Università degli studi di Napoli
FEDERICO II

Facoltà di Scienze Matematiche Fisiche e Naturali

Dottorato in
Fisica fondamentale ed applicata
XX ciclo

Nonlinear Optical Techniques applied to Perovskite Oxides.

Candidato
Andrea Rubano

Coordinatore
Prof. Gennaro Miele

Anno accademico 2006 – 2007

To my mom

Contents

Acknowledgements.

First of all, I want to thank professor Lorenzo Marrucci, whose teachings were precious and constant during all my work. I hope I will never forget them. Another very warm thanks to Dr. Domenico Paparo, which have been my "elder brother" for some years. Most of what I learned is due to him. Thanks to prof. Fabio Miletto Granozio, hoping that I will never forget his second name again, to prof. Umberto Scotti di Uccio and to Dr. Giovanni Cantele for the interesting discussions about my work. I would thank all people who lived in my lab for years or for just few weeks: Dr. Carlo Manzo, dott. Nunzia Savoia, Marco Siani and Francesca Ciccullo. Besides these persons, I would like to thank also Antigone, Alessia, Annalisa, Giulia and all the OSA Chapter of Naples, because we did some very beautiful things together.

Many things happened during the three years of my doctorate, some of them were beautiful, some were not. But what never stopped was the help of all people who supported me in the worst moments. My debt with them will never be repaid. All I can do is to deserve their love.

Introduction.

Transition-metal oxides with a perovskite-like structure form a very wide class of materials, whose physical features can be very variable. High-Tc superconductivity, colossal magnetoresistence, ferroelectricity, high dielectric constant, Mott insulator phase, antiferromagnetism are some of the many remarkable properties these fascinating materials could present. Two among them have been chosen as main targets of the present work: the yttrium-barium cuprate $YBa_2Cu_3O_{6+x}$ (YBCO) and the strontium titanate $SrTiO_3$ (STO).

YBCO is an high Tc superconductor (HTCS) and probably the most widely studied one. STO is well-known perovskite oxide, whose electronic properties can appear deceptively simple, but they are not, as we will show in this work. In order to investigate the fundamental physics of these materials, two different optical techniques have been used: the Coherent Raman Spectroscopy (CRS), on YBCO, and Photoluminescence (PL), on STO. The latter is a rather common technique on solid state: we used its time-resolved version in order to investigate the kinetics and the lifetime of a very interesting room temperature blue band, which has been recently discovered in n-doped STO by Kan and coworkers [82]. The interest in this discovery is mainly due to the possible use in electro-optical applications, since only few blue emitting sources are nowadays available and the possibility to convert the light-induced emission into an electric-induced emission will open the route to many novel devices, entirely based on perovskites. We were motivated by two main purposes: to set the intrinsic bandwidth of a future possible device and to help the understanding of the recombination mechanisms, which are responsible for this luminescence, since the discussion on this subject is still open.

The Coherent Raman Spectroscopy has been used mostly in liquids, gases and flames. Only very few works have been carried out on solid state until now. In particular, there is a lack in literature about applying this technique to high Tc superconductors. The CRS was proposed by B. Fainberg in 1991 ([85],[89]) with the name of "biharmonic pumping technique", and the first experiment has been performed one year after by V.N. Bagratashvili and coworkers [1]. To our knowledge, no other works followed. More recently, a similar nonlinear technique (not frequency-resolved) was applied to HTCS by N. Gedik and coworkers in order to directly measure the recombination and diffusion lifetimes of quasiparticles [27]. The key point of our experimental approach is the choice of a "reflection" geometry, as will be explained in the first part of this work. This non-trivial experimental geometry overcomes many problems which make this technique quite hard to be applied on this class of materials. Here we would like to stress that the present work, although giving

some interesting physical informations on the elementary excitations of YBCO, is mainly devoted to proving the feasibility of this technique on this class of materials and the many advantages it brings: a better signal-to-noise ratio, the possibility to select a specific excitation and, especially, the possibility to make Pump&Probe time-resolved measurements.

In this work, we have demonstrated that CRS spectra can measure the phase of different terms of the third order susceptibility of YBCO. This information is not present in the linear Raman spectra, which have been used from the beginning on HTCS. Phase-information has been obtained only at room temperature, but the main goal will be the study of the phase changes above and below the critical temperature. Besides this result, the CRS technique is suitable for measuring directly the lifetime of a selected low-energy excitation. This might help shedding light on the 20-years-old high temperature superconductivity puzzle.

Let us now briefly illustrate the contents of the present work.

This dissertation is divided in two Parts, which reflect the two distinct subjects of our investigation, and in this Introduction a brief overview is given for both.

The first Part is composed of five Chapters. Each Chapter focuses on a different aspect of the matter of discussion. In the first two Chapters a general overview is given on the basic CRS theory, which is useful in order to understand what the CRS technique measures, and on the main physical features of HTCS, and in particular YBCO, which is the target of this study. We will start from the basic concepts of the linear Raman scattering and, from there, we will get into the Nonlinear Optics formalism, which is the natural framework of the CRS theory in the Four Wave Mixing (FWM) formulation. In the first Chapter, we will also set out the semiclassical model used for the subsequent best-fit of our first measurements. At the end of this Chapter a brief description of an alternative formulation, the so-called Dynamic Gratings theory, is given too. In the second Chapter, we tried to give to the reader a brief and simplified review of the huge literature about HTCS. The lattice, as well as the electronic, structures are described in some detail. The transport properties and some of the possible non-BCS models, which have been proposed by several authors, are roughly explained, without the claim of completeness. In the third Chapter, we will focus our attention on the YBCO phonons and their symmetries, which are the subjects of the main results obtained from our first room temperature measurements. The fourth Chapter is dedicated to a detailed analysis of the CRS experimental setup and its principal features. Here we would like to stress that this is a quite complex apparatus, and we will give some information about its critical points and also about the several procedures which are requested in order to obtain a reliable measurement. Finally, the fifth Chapter contains our theoretical and experimental results: the complete theory of the radiated FWM field, as it is revealed in the "reflection" geometry, and some test measurements on different reference materials. In the final section, the CRS spectrum of YBCO is discussed in detail. It will be shown how the CRS technique can be used to measure the phase-shift between resonant and non-resonant terms of the third order nonlinear dielectric susceptibility.

The second Part is dedicated to the time-resolved PL analysis of pure and doped

STO. Within this Part, the sixth Chapter is focused on the principal features of the Photoluminescence emission in solid state. The main purpose of this Chapter is to introduce the reader to this subject. The seventh Chapter contains an overview about the principal features of STO, with a particular regard to its photoluminescent properties. Many experimental results are available in this field, and the knowledge of the principal ones can be very useful in order to compare them with the measurements and the models which are reported in the following Chapter. Besides a detailed explanation of the experimental setup and the step-by-step description of the best-fit procedure used to interpret our data, the last Chapter contains our main experimental results and an accurate description of the theoretical models we used to interpret them. We have investigated the time as well as the frequency domain, and we have found a non-trivial kinetics in the electron-hole recombination and a quite interesting behaviour of the PL spectrum with temperature.

Finally, in the Appendix it is possible to find some background information about some specific topics. In App. A there are some recalls on the Group Theory, which can be useful in reading the third Chapter. In App. B a short account on the relaxation times theory is given. In App. C the main concepts of BCS theory are summarized. In the last Appendix (App. D), it is reported the full Matlab program we used to make the numerical analysis of the PL data.

Finally, our main results and perspectives are summarized in the last concluding section.

Part I

Coherent Raman Spectroscopy of YBCO.

Chapter 1

The Four Waves Mixing Theory: an introduction.

In this Chapter, we will give the bases of the Nonlinear Optics concepts which are used in the first part of this work. The Chapter will be thus focused on the Raman-light generation. For a detailed treatment of this and other features of Nonlinear Optics, see in particular refs [3] and [4].

1.1 Linear and nonlinear phenomena.

Everyone of us has to deal, everyday, with several optical phenomena: mirrors, glasses, rainbows are some examples. All these phenomena are described with great accuracy in the framework of the Linear Optics Theory. This theory arises naturally (within certain hypotheses) from the Maxwell laws, which rule every electromagnetic phenomenon. Actually, the hypotheses on the base of Linear Optics are valid only in "usual" situations, where the intensity of the electromagnetic waves which interact with matter is "small". The sense of the word "small", in this framework, will be defined in the following. If this circumstance does not take place, it is necessary to get into a new formalism: the Nonlinear Optics Theory.

A nonlinear wave coupling, in the acoustic field, is known since 1714, when the Italian violinist Giuseppe Tartini discovered the phenomenon of the "third sound" [2]. He noted that, when two vibrations (as musical notes) are combined in a sound-box (as an empty room or the human ear), a third vibration comes out, even if it was not generated by the source. This "third sound" has a frequency given by the difference between the two initial frequencies. In the optical field, this phenomenon corresponds to the so-called Difference Frequency Generation (DFG). The third sound is the strongest, but not the only sound which can be generated by the nonlinear coupling of two notes: the generation of the cubic difference sound, having a frequency equal to $2f_1 - f_2$, is the exact acoustic correspondent of the optical effect known as "Raman effect", described in the present Chapter.

Before the discovery of lasers (Maimen, 1960), it was not possible to reach light intensities so strong to invalidate the hypothesis on which the Linear Optics is based.

The observation of the first nonlinear optical effect was made by Franken in 1961. He used a ruby laser of frequency 694.2 nm in order to produce an ultraviolet beam of frequency 347.1 nm. This is now known as Second Harmonic Generation (SHG). Actually, the optical pumping on the base of the laser inversion of population is a nonlinear phenomenon too, but the Franken experiment was the first in which a coherent input produces a coherent output.

Soon, the Nonlinear Optics was found to be a very powerful tool for spectroscopic investigations, beside being a fascinating stand-alone research field.

In this Chapter some theoretical guidelines will be briefly provided, in order to better clarify the framework in which the experimental results of the present dissertation will be presented.

1.2 A short account on Nonlinear Optics.

The polarization and magnetization vectors ($\vec{P}$ and $\vec{M}$ respectively) completely describe the electromagnetic response of every material, while Maxwell equations rule the propagation of the electromagnetic wave through the material medium itself. Let us write down these laws, for simplicity, without charges and currents:

$$\begin{aligned}
&\vec{\nabla} \wedge \vec{E} = -\frac{\partial \vec{B}}{\partial t} \\
&\vec{\nabla} \wedge \vec{H} = \frac{\partial \vec{D}}{\partial t} \\
&\nabla \cdot \vec{B} = 0 \\
&\nabla \cdot \vec{D} = 0
\end{aligned}$$

In order to close this system, it is necessary to define the constitutive relationships of the material, i.e. to specify the dependence of the two inductions $\vec{D}$ and $\vec{B}$ from the electric and magnetic fields $\vec{E}$ and $\vec{H}$. In the case of optical electromagnetic waves, i.e. with a frequency in the range $(3.84 \div 7.69) \times 10^{14}$ Hz, it is almost always possible to neglect the magnetic response of the material, as it depends on the Lorentz force acting on the electron, in its motion around the nucleus. Since the Lorentz force is proportional to the vector $(\vec{v}_e/c) \wedge \vec{B}$, being the ratio between the electron speed ad the light velocity $\vec{v}_e/c$ of the order of 10^{-5}, the approximation $\vec{B} = \mu_0 \vec{H}$ almost always holds true. The constitutive relationship between the electrical induction $\vec{D}$ and the electric field $\vec{E}$ is, in turn, $\vec{D} = \varepsilon_0 \vec{E} + \vec{P}(\vec{E})$. The vector $\vec{P}(\vec{E})$ in its general form is a functional of the electric field, and it has to vanish in the absence of the inducing field, since there is not any material with a spontaneous optical polarization. If the field intensity is "small", with respect to the atomic coulomb potential, it is almost always possible to write the polarization as a linear functional of the applied electric field. In this case the most general form is an integral operator, and its kernel depends both on the relative positions and times:

$$\vec{P}(\vec{r}, t) = \int \chi\left(\vec{r} - \vec{r}', t - t'\right) \; \vec{E}\left(\vec{r}', t'\right) \; d\vec{r}' dt'.$$

If this kernel is proportional to a time delta function, the material will present an instantaneous response, and the dielectric constant ε will be, thus, independent of the excitation frequency ω. If the kernel is proportional to a space delta function,

the material will have a local response, i.e. the polarization in a given space point will depend only on the local field, as it happens at optical frequencies in almost all materials.

If the tensor has degenerate eigenvalues, the material will be uniaxial or birefringent in the case of second order degeneration, and isotropic in the case of third order degeneration.

This is the framework of Linear Optics.

Nevertheless, when the light intensity is sufficiently high, the linear approximation for $\vec{P}(\vec{E})$ is no longer valid. More orders are needed in the power expansion:

$$\vec{P}(\vec{E}) = \varepsilon_0(\chi^{(1)} \cdot \vec{E} + \chi^{(2)}{:}\vec{E}\vec{E} + \chi^{(3)}{:}\vec{E}\vec{E}\vec{E}) + o[|E|^4] \Rightarrow \tag{1.1}$$

$$\Rightarrow P_i = \varepsilon_0(\chi^{(1)}_{ij}E_j + \chi^{(2)}_{ijk}E_jE_k + \chi^{(3)}_{ijkl}E_jE_kE_l) + o[|E|^4] \tag{1.2}$$

$$\vec{P}(\vec{E}) = \vec{P}^L(\vec{E}) + \vec{P}^{NL}(\vec{E}), \tag{1.3}$$

where $\vec{P}^L(\vec{E})$ is the usual linear polarization while the vector $\vec{P}^{NL}(\vec{E})$ contains, for brevity, the second and the third order polarizations. The main reason why it is convenient to expand until the third order, instead of the second, is that the second order term vanishes if the material has a center of inversion[1].

Assuming Eq. 1.1, the Maxwell Equations become a coupled nonlinear system of differential equations, which does not admit a general exact solution.

However, with the help of an appropriate hypothesis, it is possible to find an analytical solution in many cases of great interest.

Nevertheless, such a great mathematical effort is not necessary to understand intuitively what the insertion of a nonlinear polarization into Maxwell equations means, from a physical point of view. Actually, the wave-equation has the time second derivative of $\vec{P}(\vec{E})$ as a source term. It is possible to obtain the usual vacuum wave equation using the position $\varepsilon_r = (1 + \chi^{(1)})$, following the same route of the linear theory. If the polarization is given by Eq. 1.1, one obtains

$$\nabla^2\vec{E} - \frac{1}{c^2}\frac{\partial^2}{\partial t^2}\varepsilon_r\vec{E} = \mu_0\frac{\partial^2}{\partial t^2}\vec{P}^{NL}. \tag{1.4}$$

Let us now consider a simple monochromatic electric field, and the nonlinear polarization it induces:

$$E \propto \cos(\omega t) \Rightarrow P^{NL} \propto \cos^2(\omega t) = \frac{1}{2}(1 + \cos(2\omega t)).$$

One can see that the presence of a quadratic behaviour in the field produces a source term in the wave-equation which oscillates at the double frequency. This example allows to show very directly one of the most relevant aspects of the nonlinear phenomena: the possibility to generate output frequencies which are different from the input ones.

[1] the proof is:
$\vec{r} \to -\vec{r} \Rightarrow \vec{E} \to -\vec{E}; \vec{P} \to -\vec{P}$
$-P_i = -\varepsilon_0\chi^{(2)}_{ijk}(-E_j)(-E_k) = P_i = \varepsilon_0\chi^{(2)}_{ijk}E_jE_k \Rightarrow$
$\Rightarrow \chi^{(2)}_{ijk} = -\chi^{(2)}_{ijk} \Rightarrow \chi^{(2)}_{ijk} = 0$

In the general case of a third order process, we have to deal with four different frequencies. Thus, the general theory is known as Four Wave Mixing (FWM).

The nonlinear susceptibility $\chi^{(3)}_{ijkl}$ is, in general, a 4-rank tensor having 81 complex elements, which are, in turn, the sum of 48 terms [3]. The number of non-vanishing terms in this tensor is greatly reduced by the symmetries and the resonances of the material, but a symmetry which makes the whole tensor vanishes, does not exist.

Let us write Eq. 1.1 in a component notation:

$$P_i(\vec{k},\omega)=\sum_{n,m,p}\chi^{(3)}_{ijhk}(-\vec{k},\vec{k}_n,\vec{k}_m,\vec{k}_p;-\omega,\omega_n,\omega_m,\omega_p)\cdot \\ \cdot E_j(\vec{k}_n,\omega_n)E_h(\vec{k}_m,\omega_m)E_k(\vec{k}_p,\omega_p),$$

where the sum is made on the indices n,m,p which satisfy the relationships $\omega_n + \omega_m + \omega_p = \omega$ and $\vec{k}_n + \vec{k}_m + \vec{k}_p = \vec{k}$. This means that the third order susceptibility actually does not depend on $\vec{k}$ and ω, but the dependence was introduced only for notational symmetry reasons: in this way, we have one variable pair corresponding to each index, including both input and output fields.

In general, the following index permutation symmetry of the $\chi^{(3)}$ tensor always holds true:

$$\chi^{(3)}_{ijhk}(-\vec{k},\vec{k}_n,\vec{k}_m,\vec{k}_p;-\omega,\omega_n,\omega_m,\omega_p) = \\ = \chi^{(3)}_{ihjk}(-\vec{k},\vec{k}_m,\vec{k}_n,\vec{k}_p;-\omega,\omega_m,\omega_n,\omega_p) = \\ = \chi^{(3)}_{ijkh}(-\vec{k},\vec{k}_n,\vec{k}_p,\vec{k}_m;-\omega,\omega_n,\omega_p,\omega_m).$$

Moreover, since the electric field and the optical polarization have to be real vectors, the condition

$$\chi^{(3)}_{ijhk}(-\vec{k},\vec{k}_n,\vec{k}_m,\vec{k}_p;-\omega,\omega_n,\omega_m,\omega_p)= \\ = \chi^{(3)*}_{ijhk}(\vec{k},-\vec{k}_n,-\vec{k}_m,-\vec{k}_p;\omega,-\omega_n,-\omega_m,-\omega_p).$$

holds true.

Some other very useful symmetry properties can be achieved within some additional hypotheses. For non-disspative loss-less materials is possible to prove that

$$\chi^{(3)}_{ijhk}(-\vec{k},\vec{k}_n,\vec{k}_m,\vec{k}_p;-\omega,\omega_n,\omega_m,\omega_p) = \\ = \chi^{(3)}_{jihk}(\vec{k}_n,-\vec{k},\vec{k}_m,\vec{k}_p;\omega_n,-\omega,\omega_m,\omega_p)$$

Finally, in most cases it is possible to assume a point-by-point local relationship, in order to neglect any spatial dispersion, i.e. the dependence on the wave-vector $\vec{k}_i$. The optical polarization is, thus, a function of the position $\vec{r}$ inside the material:

$$P_i(\vec{r},\omega)=\sum_{n,m,p}\chi^{(3)}_{ijhk}(-\omega,\omega_n,\omega_m,\omega_p)\cdot \\ \cdot E_j(\vec{r}_n,\omega_n)E_h(\vec{r}_m,\omega_m)E_k(\vec{r}_p,\omega_p) \tag{1.5}$$

In literature, the complete calculation of all the $\chi^{(3)}_{ijkl}$ elements is present, but here we will calculate only those terms which are involved in the case of our interest, i.e. the Stokes and anti-Stokes Raman light generation.

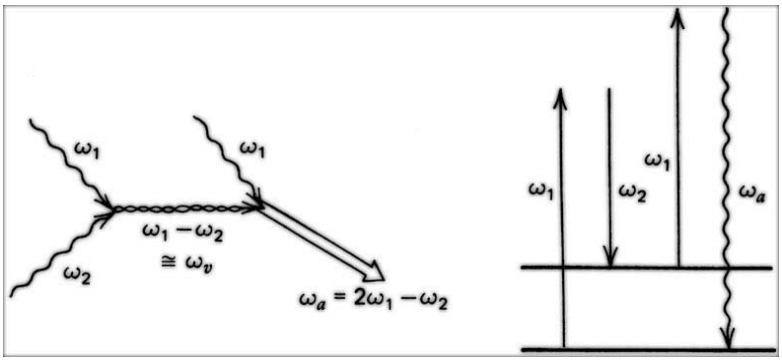

Figure 1.1: Quantum diagrams of the anti-Stokes scattering [4].

1.3 Raman Spectroscopy.

The Raman effect can be regarded as an interaction between the material and the beating of two photons, and not between the material and the single photon, as normally happens in absorption and emission phenomena.

In Fig 1.1 a quantum picture and the level diagram is showed. Let us imagine to deal with a simple system, for instance a molecule, with a vibrational level of frequency $\hbar\omega_v$. When a very intense and monochromatic beam of frequency ω_1 interacts with the molecule, a spectral analysis of the emitted light shows the presence of distinct and equally spaced series of lines, on the right side as well as on the left side of the "pump" frequency ω_1. These series are called Stokes lines (below ω_1) and anti-Stokes lines (above ω_1).

This effect is known as Spontaneous Raman Scattering (SRS). It is an isotropic effect, since the scattered light is diffused in all directions. Its complete description requires the use of a quantum theory of the electromagnetic field.

This obstacle can be easily overcome using the concept of "vacuum photon", i.e. assuming that the quantum fluctuations of the electromagnetic field produce the presence of one photon for each mode. This vacuum photon can act as a seed for the scattering process, and it allows a classical treatment of this effect, as shown in the following.

The stimulated Raman effect is, on the contrary, strongly anisotropic: the scattered light has a well-defined direction, according to the so-called "phase-matching" relationship, as shown in the following. Two pump beams of frequencies ω_1 and ω_2 are sent on the molecule and a third beam of frequency $2\omega_1 - \omega_2$ is collected at the output. The intensity of the output beam as a function of the frequency ω_2 will give the stimulated Raman spectrum, where the Stokes lines will be observed for $\omega_2 > \omega_1$ and the anti-Stokes lines for $\omega_2 < \omega_1$. This spectrum has different features compared with the spontaneous one, as will be shown in the following.

In the Stokes case, the molecule absorbs a photon of frequency ω_1 reaching a virtual high-energy level, and gives out back a photon of frequency ω_2, which is in fact the first line of the Stokes series. It reaches the final excited vibrational level

with energy $\hbar\omega_v$. In the anti-Stokes case, the excited molecule absorbs the pump photon and reaches the ground level by the emission of a photon with frequency ω_a, i.e. the first anti-Stokes line.

The algebraic relationship between these frequencies is

$$\omega_2 + \omega_v = \omega_1 \qquad \omega_a - \omega_v = \omega_1 \qquad \omega_a = 2\omega_1 - \omega_2 \tag{1.6}$$

The other lines of the two series are due to a subsequent scattering with a Stokes photon acting as a pump photon for a new process, giving, in this way, a photon of frequency $\omega_{2s} = \omega_2 - \omega_v = \omega_1 - 2\omega_v$, i.e. the second Stokes line. Each line will be weaker than the previous one. Both series come from a single resonance of the molecule. It is, thus, easy to imagine that the Raman spectrum of a real complex system will be an extremely complicated object, and its analysis can be an hard task.

The study of the Raman spectrum gives, thus, many information on the vibrational or rotational levels in the case of gases and liquids, or on the elementary excitations in the case of our interest: the solid state. In this case, it is further to note that only $\vec{k} \sim 0$ (where $\vec{k}$ is the lattice wave-vector) excitations can be induced by the anelastic scattering with photons, since the photon carries an almost zero kinetic momentum, compared with a phonon one. Thus, only the $\vec{k} \sim 0$ point (called $\Gamma-$point) of the Brillouin zone can be investigated by means of this technique.

The usual Raman-based spectroscopic techniques use its spontaneous version, and the spectroscopic analysis is made with very high sensitivity spectrometers. In a stimulated Raman experiment, the resonances are investigated by means of a tunable laser source and a high-sensitivity detector, as a photomultiplier. In this case, the signal beam is strongly anisotropic, and this makes easier the separation between the signal and the scattered background.

We should note that, in the spontaneous effect, the Stokes lines often show a very much higher intensity than the anti-Stokes ones. This happens since the anti-Stokes process needs to start from an excited level, which is less populated than the ground level. In the stimulated effect, on the contrary, the excited population is induced by the beating of the two pump beams, and so the two series have a comparable intensity. This nonlinear optical technique is known as Coherent Raman Spectroscopy (CRS). Usually, one distinguishes the Stokes and the anti-Stokes cases, leading to the so-called Coherent Stokes Raman Spectroscopy (CSRS) and Coherent anti-Stokes Raman Spectroscopy (CARS).

1.4 The semiclassical model.

The probability per unit time (P_s) of a photon to be emitted into a Stokes mode[2] is a function of the pump intensity. In the case of a stimulated emission, it will be a function of the Stokes beam intensity too, so that the hypothesis on the base of this semi-classical theory of Raman scattering is very similar to the one usually assumed in the case of the stimulated emission of a photon by an atom, which is

$$P_S = Dm_L\,(m_S + 1) \tag{1.7}$$

[2] For clarity, let us now limit the discussion to the Stokes case.

where m_L is the mean value of the pump mode photon number, m_S is the Stokes mode one, D is a constant which depends on the material, and the unity hides behind itself the quantum vacuum fluctuations, as mentioned before.

This hypothesis can be strictly proved in a complete quantum formalism, where the electromagnetic field is a quantum vector too.

By its definition, the emission probability per unit time is

$$P_S = \frac{dm_S}{dt} = \frac{c}{n}\frac{dm_S}{dz}$$

where $\hat{z}$ is the propagation direction of the Stokes light[3]. Thus, we have

$$\frac{dm_S}{dz} = \frac{n}{c} D m_L \left(m_S + 1\right). \tag{1.8}$$

Eq. 1.8 admits a general solution, but it is more instructive to solve it in two opposite limits. This approach have the merit to stand out the main features which distinguish the spontaneous from the stimulated Raman process.

$$\begin{aligned} m_S \ll 1 \qquad & \frac{dm_S}{dz} = \frac{n}{c} D m_L \\ m_S \gg 1 \qquad & \frac{dm_S}{dz} = \frac{n}{c} D m_L m_S. \end{aligned}$$

Assuming that the pump intensity is not greatly affected by the process, i.e. the fraction of the pump photons converted into Stokes photons is small, we have the following two solutions:

$$\begin{aligned} m_S \ll 1 \qquad & m_S\left(z\right) = \frac{n}{c} D m_L \, z \\ m_S \gg 1 \qquad & m_S\left(z\right) = m_S\left(0\right) \, \exp\left(Gz\right) \end{aligned}$$

where $G = \left(n/c\right) D m_L$ is the Raman gain factor and $m_S\left(0\right)$ is the input number of Stokes photons. The distinction between the spontaneous and the stimulated process is now clear: the presence or not of a Stokes photons number sufficiently higher than the vacuum fluctuations, deeply changes the nature of the differential equations which rule the process. This leads to have two very different solutions: in the first case, the number of emitted photons scales linearly with the length z, which is the path of the light along the medium[4], while, in the second, it scales exponentially, with a gain factor which varies, in turn, linearly with the pump intensity.

In Eq. 1.7, we introduced the constant D in order to account for the features of the material. This features are present in the Maxwell equations inside the electrical susceptibility, being it linear or not. For this reason, a simple classical model is proposed, here, in order to get a quantitative estimate of the nonlinear susceptibility which takes part into the Raman scattering.

[3] note that it is not needed that the pump-light has the same direction.

[4] this case is also known as Linear Raman Scattering.

Let us consider, for clarity, a molecular material, and let us call q a vibrational coordinate which characterizes an internal degree of freedom. The dipole moment induced by an electric field will be $\vec{p} = \alpha\vec{E}$, where α is the optical polarizability.

The total polarization can, thus, be written as

$$\vec{P}(\vec{E}) = N\alpha\vec{E}, \tag{1.9}$$

where N is the number of molecules per unit volume of the medium. The postulate of the model is that the polarizability α depends linearly from the vibrational coordinate q:

$$\alpha(t) = \alpha_0 + \left.\frac{\partial\alpha}{\partial q}\right|_{q=0} q(t),$$

where α_0 is the polarizability at the equilibrium point $q = 0$, while the behaviour of q itself is given by

$$\frac{d^2}{dt^2}q(t) + 2\gamma\frac{d}{dt}q(t) + \omega_v^2 q(t) = F(t)/m, \tag{1.10}$$

which is a simple forced oscillator equation of the motion: γ is a dumping factor, ω_v is the proper frequency of the oscillator, m is the reduced nuclear mass, and the forcing term $F(t)$ is given by the presence of the electric field.

In order to achieve an explicit relationship between the forcing term and the applied field, let us consider the interaction energy between the single dipole moment and the electric field, which is

$$W = -\frac{1}{2}\langle\vec{p}(z,t)\cdot\vec{E}(z,t)\rangle = -\frac{1}{2}\alpha\langle\vec{E}^2\rangle,$$

where the average is done over a time scale larger than the optical period, but shorter than the vibration period of the molecule.

The Coulomb force applied on the vibrational degree of freedom, thus, is

$$F(z,t) = -\frac{dW}{dq} = \frac{1}{2}\left.\frac{\partial\alpha}{\partial q}\right|_0 \langle\vec{E}^2\rangle.$$

Assuming the following form for the total electric field $\vec{E}(z,t)$

$$\vec{E}(z,t) = A_1\exp(ik_1 z - i\omega_1 t) + A_S\exp(ik_S z - i\omega_S t) + c.c.$$

where ω_1 is the pump frequency, ω_S the Stokes frequency, $k_{1,S}$ and $A_{1,S}$ are the wave-vectors and amplitudes, respectively, one obtains

$$F(z,t) = \frac{1}{2}\left.\frac{\partial\alpha}{\partial q}\right|_0 [A_1 A_S^*\exp(ikz - i\omega t) + c.c.] + \text{cost.}$$

where $k = k_1 - k_S$ and $\omega = \omega_1 - \omega_S$.

Here, it can be better understood what was mentioned before: the Raman effect emerges from the coupling between an internal degree of freedom of the material and the beating of two photons, which appears, just here, as the forcing term in

the harmonic oscillator equation of the motion. Now, Eq. 1.10 can be solved by searching a solution of the form:

$$q(t) = \tilde{q}(\omega) \exp(ikz - i\omega t) + c.c. \tag{1.11}$$

From Eq. 1.10 and Eq. 1.11, we have

$$\tilde{q}(\omega) = \frac{1}{2m} \left.\frac{\partial \alpha}{\partial q}\right|_0 \frac{A_1 A_S^*}{\omega_v^2 - \omega^2 - 2i\omega\gamma}.$$

From Eq. 1.9, this solution leads immediately to an explicit expression for the total polarization, which is

$$\vec{P}(z,t) = N\left(\alpha_0 + \left.\frac{\partial \alpha}{\partial q}\right|_0 q(z,t)\right)\vec{E}(z,t).$$

The term α_0 is the usual linear polarization form, in which the polarizability is a constant, while the remaining part gives the nonlinear polarization

$$\vec{P}^{NL}(z,t) = N \left.\frac{\partial \alpha}{\partial q}\right|_0 \left[\tilde{q}(\omega) e^{(ikz - i\omega t)} + c.c.\right] \cdot \left[A_1 e^{(ik_1 z - i\omega_1 t)} + A_S e^{(ik_S z - i\omega_S t)} + c.c.\right].$$

This is, thus, the sum of several terms which oscillate at different frequencies, and every term will appear into the wave-equation as a source term (Eq. 1.4). We have to separate this terms, and calculate the contribution of each term to the total solution.

Since $\omega = \omega_1 - \omega_S$, the Stokes term is

$$\vec{P}^{NL}(z,t) = \vec{P}(\omega_S) \exp(i\omega_S t) + c.c.$$

with

$$\vec{P}(\omega_S) = \frac{N|A_1|^2 A_S}{2m} \left(\frac{\partial \alpha}{\partial q}\right)^2 \frac{1}{\omega_v^2 - (\omega_1 - \omega_S)^2 - 2i(\omega_1 - \omega_S)\gamma} \exp(ik_S z)\ . \tag{1.12}$$

Now, writing the ω_S component from Eq. 1.1 in the frequency domain[5] we have

$$\vec{P}(\omega_S) = 6\chi_R(\omega_S)|A_1|^2 A_S \exp(ik_S z). \tag{1.13}$$

Finally, by comparison of Eq. 1.12 and Eq. 1.13, we have

$$\chi_R(\omega_S) = \chi_R'(\omega_S) + i\chi_R''(\omega_S) = \frac{N}{12m}\left(\frac{\partial \alpha}{\partial q}\right)^2 \frac{1}{\omega_v^2 - (\omega_1 - \omega_S)^2 - 2i(\omega_1 - \omega_S)\gamma}. \tag{1.14}$$

The behaviour of the real and imaginary parts of $\chi_R(\omega_S)$ has, thus, a typical resonance structure, as shown in Fig 1.2.

Once an explicit form for the susceptibility is obtained, is possible to solve the wave-equation (Eq. 1.4), which can be written as

[5] the factor 6 accounts for the symmetry $\chi_{ijkl} = \chi_{ijlk} = \chi_{ikjl} = \chi_{iklj} = \chi_{ilkj} = \chi_{iljk}$, (the simultaneous permutation of the frequencies is omitted).

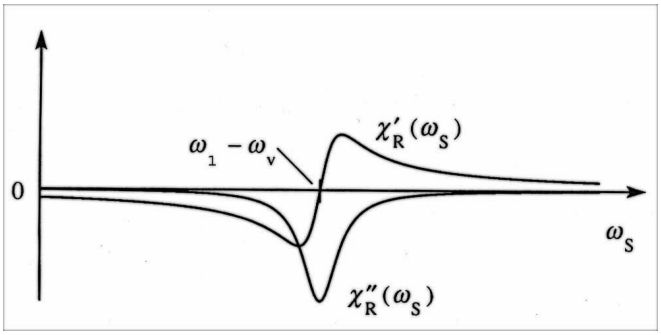

Figure 1.2: Real and immaginary part of the Raman susceptibility [4].

$$\frac{d}{dz}A_S = GA_S \Rightarrow A_S = A_S(0)\exp(Gz), \tag{1.15}$$

with

$$G \propto i\omega_S \chi_R(\omega_S)|A_L|^2.$$

Here, the second derivative of the amplitude A_S is neglected, since it is assumed a very slow energy transfer with respect to the field oscillations.

In correspondence of the resonance $\omega_S = \omega_1 - \omega_v$, $\chi_R(\omega_S)$ assumes a pure imaginary negative value, and so G is a positive real number. Eq. 1.15 describes, thus, an amplification of the Stokes light during its path along the medium; this gain is independent from the direction of propagation[6] $\vec{k}_S$.

Let us now analyze the nonlinear polarization term which oscillates at the anti-Stokes frequency. Since any hypothesis on the sign of $\omega_1 - \omega_S$ was done until now, Eq. 1.14 is immediately applicable to the anti-Stokes case, with the substitution

$$\omega_1 - \omega_S = -(\omega_1 - \omega_a),$$

so that

$$\chi_R(\omega_a) = \chi_R^*(\omega_S).$$

Near the resonance $\omega_a = \omega_1 + \omega_v$, $\chi_R(\omega_a)$ is a positive imaginary number (Fig 1.3), and so the gain-factor G is a negative real number. This means that the anti-Stokes light will be depleted instead of being amplified. Actually, this holds true in linear Raman scattering experiments, in which the anti-Stokes light is very hard to be revealed, but, nevertheless, experimental evidence clearly show that in the stimulated process, both channels have a comparable intensity. This discrepancy will be solved in the Nonlinear Optics formalism, as shown in the next section. The anti-Stokes light is produced as a pure three waves beating between two pump photons and one Stokes photon, as shown in the quantum diagrams of Fig 1.1.

[6] This means that the Stokes process is automatically "phase-matched". The concept of phase-matching will be shown in the next paragraph.

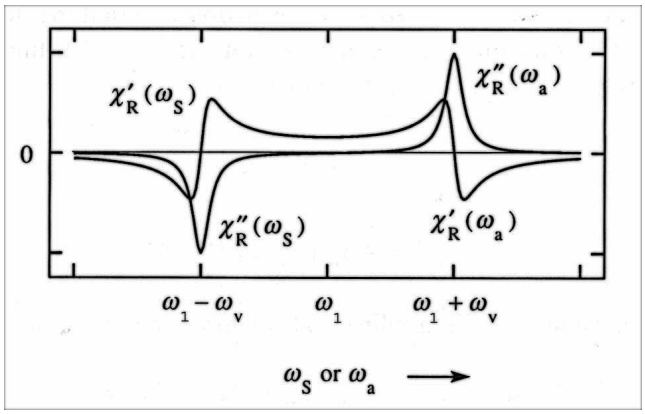

Figure 1.3: Stokes and Anti-Stokes resonances of the Raman susceptibility [4].

Eq. 1.14 has a direct dependence on the vibrational frequency ω_v, but the dumping factor γ shifts the observed resonance frequency ω_0 to the value $\omega_0^2 = \omega_v^2 - \gamma^2$, as easily proved by solving the dumped harmonic oscillator equation. Writing Eq. 1.14 in terms of ω_0 and the so-called "Raman shift" $\Delta\omega = \omega_1 - \omega_{S,a}$ one obtains a very short and useful form of the Raman susceptibility:

$$\chi_R(\Delta\omega) \propto \frac{1}{\Delta\omega + \omega_0 + i\gamma} - \frac{1}{\Delta\omega - \omega_0 + i\gamma}. \tag{1.16}$$

In this relationship, the Stokes and the anti-Stokes resonances are explicated in each term, in which the sign of ω_0 is inverted. Eq. 1.16 will be the relationship we will use to interpret the CRS spectra in Ch. 5.

1.5 The FWM in the Nonlinear Optics formalism.

The stimulated Raman effect is a third order nonlinear process, in which three photons interact inside the material to generate a fourth, and so it has to be framed in the general formalism of the third order Nonlinear Optics [4]. This theory describes the coupling between three travelling waves and so it takes the name of Four Wave Mixing (FWM). The Raman effect is a particular case of FWM, in which two of the three input waves are coincident. Nevertheless, in this section the general formalism of the non-degenerate FWM will be shown, since the experiment presented in Part I is degenerate in frequency but not in the wave-vectors.

As mentioned before, the third order nonlinear term, in the expression of the polarization as a function of the applied field, generates the coupling between the four waves, each having a proper direction of propagation, polarization and frequency. Let us now analyze in detail how this interaction takes place, and what features it has.

Let us write the wave-equation with a nonlinear third order source term

$$-\nabla \times \nabla \times \vec{E} - \frac{n^2}{c^2}\frac{\partial^2}{\partial t^2}\vec{E} = \mu_0 \frac{\partial^2}{\partial t^2}\vec{P}^{NL},$$

with

$$\vec{P}^{NL}(\vec{E}) = \varepsilon_0 \chi^{(3)} : \vec{E}\vec{E}\vec{E} \Rightarrow P_i^{NL} = \varepsilon_0 \chi^{(3)}_{ijkl} E_j E_k E_l, \tag{1.17}$$

where the indexes $i, j, k, l = x, y, z$ indicate the total electric field components. Let us assume the following form for the field $\vec{E}$, which is present in Eq. 1.4:

$$\vec{E}(\vec{r}, t) = \vec{E}_1 + \vec{E}_2 + \vec{E}_3 + \vec{E}_4, \tag{1.18}$$

where

$$\begin{cases} \vec{E}_1 = \frac{1}{2}\hat{e}_1 \cdot [\mathcal{E}_1 \exp[i(\vec{k}_1 \cdot \vec{r} - \omega_1 t)] + c.c]. \\ \vec{E}_2 = \frac{1}{2}\hat{e}_2 \cdot [\mathcal{E}_2 \exp[i(\vec{k}_2 \cdot \vec{r} - \omega_2 t)] + c.c.] \\ \vec{E}_3 = \frac{1}{2}\hat{e}_3 \cdot [\mathcal{E}_3 \exp[i(\vec{k}_3 \cdot \vec{r} - \omega_3 t)] + c.c.] \\ \vec{E}_4 = \frac{1}{2}\hat{e}_4 \cdot [\mathcal{E}_4 \exp[i(\vec{k}_4 \cdot \vec{r} - \omega_4 t)] + c.c.] \end{cases} . \tag{1.19}$$

From Eq. 1.19 and Eq. 1.17, we have

$$P_i^{NL}(\omega_4, \vec{r}) = \frac{1}{2}\varepsilon_0 \chi^{(3)}_{ijkl}\ \hat{e}_1^j \hat{e}_2^k \hat{e}_3^l\ \mathcal{E}_1 \mathcal{E}_2^* \mathcal{E}_3\ \exp\left[i\left(\vec{k}_4 \cdot \vec{r} - \omega_4 t\right) + c.c\right]. \tag{1.20}$$

with

$$\omega_4 = \omega_1 - \omega_2 + \omega_3. \tag{1.21}$$

Here the unit-vectors $\hat{e}_i$ represent the polarizations, $\mathcal{E}_i$ the complex amplitudes, $\vec{k}_i, \omega_i$ the wave-vectors and the frequencies of each applied field[7].

Eq. 1.20 is the term which forces the anti-Stokes oscillations, while the other terms in Eq. 1.17 will give a different mixing of the three frequencies ω_i. By the insertion of Eq. 1.19, Eq. 1.18 and Eq. 1.20 in Eq. 1.4 one obtains a nonlinear coupled system of differential equations.

The condition of Eq. 1.21 is nothing but the total photon energy conservation law, during the interaction. Note that Eq. 1.6 and Eq. 1.21 coincide, if a partial degeneration of frequencies is present, i.e. $\omega_1 = \omega_3$:

$$\omega_4 \equiv \omega_a = \omega_1 - \omega_2 + \omega_3 = 2\omega_1 - \omega_2. \tag{1.22}$$

A first simplification of the system is possible by means of the so-called "slow varying amplitude approximation", which is a common hypothesis in Nonlinear Optics. The approximation is to neglect the second derivative of the amplitudes of the fields in Eq. 1.19, since it is assumed that the energy transfer between the involved wave is slow compared to the field oscillations. This idea is supported by experimental evidence in a very large number of cases.

[7] here, the fields are written inside the material. Reflection and refraction laws would be taken into account in a complete calculation.

1.5.1 The phase-matching relationship.

The slow-varing amplitude approximation brings down the order of the system from the second to the first, but it is not able to decoupling its equations. The system becomes decoupled within the so-called "non-depletion approximation", in which one assumes that this energy transfer is "small", beside being slow.

This means that the ratio between the total energy and the energy given by the pump beams to the FWM beam is close to zero. Within this hypothesis, the wave-equation is very easy to integrate, and it gives a FWM beam intensity $I_{4i}(L)$ which is

$$I_{4i}(L) \propto 2L^2 \left| \chi^{(3)}_{ijkl}\, \hat{e}_1^j \hat{e}_2^k \hat{e}_3^l\, \mathcal{E}_1(0)\, \mathcal{E}_2^*(0)\, \mathcal{E}_3(0) \right|^2 \left(\frac{1-\cos(\Delta k L)}{(\Delta k L)^2} \right),$$

where L is the superposition length of the four beams, and $\Delta k = \left| \vec{k}_1 - \vec{k}_2 + \vec{k}_3 - \vec{k}_4 \right|$ is the so-called "mismatch" factor.

Note that the factor $(1-\cos(\Delta kL))/(\Delta kL)^2$ makes the FWM beam intensity significantly strong only when[8]

$$\Delta k \approx 0 \Rightarrow \vec{k}_4 = \vec{k}_1 - \vec{k}_2 + \vec{k}_3 \tag{1.23}$$

This condition (Fig 1.4) is the so-called "phase-matching".

The phase-matching is a crucial point in all nonlinear phenomena of the third, as well as the second, order, simply because it is, from a physical point of view, the total kinetic momentum conservation law of the interacting photons.

Another point of view is to pay attention to the coherent nature of this energy transfer: each of the four involved waves have to keep a well defined and constant relative phase, in order to have a positive (constructive) interference. This condition is, thus, on the base of the strong anisotropy which characterizes the FWM process, which is one of the advantages of the CRS technique. Actually, in the experimental practice of a spontaneous process, the initial electric field $\vec{E}_4$ is given by the quantum vacuum oscillations, so that only those photons which have a wave-vector $\vec{k}_4$ which satisfy the relationship $\Delta k = \vec{k}_1 - \vec{k}_2 + \vec{k}_3 - \vec{k}_4 \approx 0$, will be amplified, and they will generate a small cone of light around the $\vec{k}_4$ direction. In the stimulated scattering experiment, we have to achieve the minimization of the phase-mismatch, in order to have a stronger signal and to avoid it can oscillate.

1.5.2 The Raman tensor.

In case of a perfect phase-matching, the FWM signal as a function of frequency and polarizations is a direct measurement of the square modulus of the third order susceptibility tensor: each particular combination of input and output polarizations will measure a particular component of that tensor. It is, thus, interesting to compare the Raman tensor, which is defined in the case of linear Raman scattering, with the third order susceptibility, which gives the efficiency of the FWM process.

[8] Actually, we could also choose $L \approx 0$, but, in this case, the intensity would be very much reduced by the factor L^2.

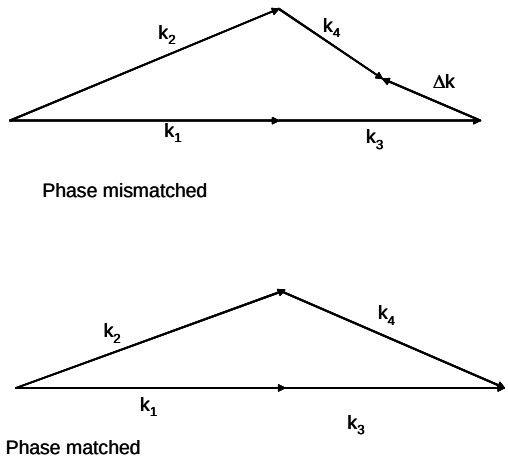

Figure 1.4: Vectorial form of the phase-matching factor.

In Ch. 1.4 the behaviour of the Raman susceptibility with respect to the Raman shift $\Delta\omega$ was obtained. The same semiclassical model can be used again, taking into account each combination of polarizations of the incident and emitted waves, as in the case of linear Raman scattering. The Raman scattering efficiency is found to be proportional to the square modulus of the so-called "Raman tensor", defined as

$$\tilde{R} = \hat{e}_S^* \cdot \frac{\partial \tilde{\chi}}{\partial q} \cdot \hat{e}_L,$$

where $\hat{e}_S$ and $\hat{e}_L$ indicate the Stokes and the pump-light polarizations unit-vectors, respectively, while $\tilde{\chi}$ is the linear dielectric susceptibility tensor. Writing Eq. 1.17 in the case of a partial degeneration of frequencies, as given by Eq. 1.22, one obtains

$$P_i(\omega_4) = 3\varepsilon_0 \chi^{(3)}_{ijkl}(\omega_4 = \omega_1 + \omega_1 - \omega_2) E_j(\omega_1) E_k(\omega_1) E_l^*(\omega_2), \tag{1.24}$$

where the index NL is omitted for clarity and 3 is a numerical factor which collects three identical terms.

Now, following the above discussed semiclassical model, we assume that the linear susceptibility tensor is not constant in time, but modulated because of the variation of the oscillator degree of freedom $q(t)$. From this assumption, the following form of the induced polarization can be found:

$$P_i(\omega_4) = \frac{\varepsilon_0^2}{2m\omega_0} \left(\frac{\partial \chi_{ij}}{\partial q} \frac{\partial \chi'_{kl}}{\partial q} \right) F(\Delta\omega, \omega_0) E_{1j} E_{1k} E_{2l}^*, \tag{1.25}$$

where $F(\Delta\omega, \omega_0)$ is the resonance factor as defined by Eq. 1.16, the apex on χ denotes the real part and the numerical index in the electric field expressions is a short form to indicate the frequency of each field oscillation ω_1, ω_2. By comparison between Eq. 1.24 and Eq. 1.25 and taking into account the symmetry between j and k indices, one obtains

$$\chi^{(3)}_{ijkl}(\omega_4 = \omega_1 + \omega_1 - \omega_2) = \frac{\varepsilon_0}{6m\omega_0} \frac{1}{2} \left(\frac{\partial \chi_{ij}}{\partial q} \frac{\partial \chi'_{kl}}{\partial q} + \frac{\partial \chi_{ik}}{\partial q} \frac{\partial \chi'_{jl}}{\partial q} \right) F(\Delta\omega, \omega_0).$$

Here we used an explicit symmetrized form. Finally, the effective susceptibility, for a given input-output combination of polarizations, is

$$\chi_{eff} = \frac{\varepsilon_0}{6m\omega_0}\left(\frac{\partial\chi_{ij}}{\partial q}\frac{\partial\chi'_{kl}}{\partial q}\hat{e}^*_{4i}\hat{e}_{1j}\hat{e}_{1k}\hat{e}^*_{2l}\right)F(\Delta\omega,\omega_0),$$

where the symmetrized form is no longer necessary, since it is assumed the sum over mute indices. The polarization unit vector $\hat{e}_1$ is referred to the ω_1 frequency, and, thus, it plays the role of the pump-light polarization $\hat{e}_L$ of the linear case. The unit vectors $\hat{e}_4$ and $\hat{e}_2$ play instead the role of the Stokes polarization $\hat{e}_S$.

Finally let us note that the Raman tensor depends on the first derivative of the linear susceptibility, while, in the nonlinear case, the effective susceptibility depends on the square of that derivative. This means that χ_{eff} could be written as the product between two different Raman tensors, one referred to $\hat{e}_S \equiv \hat{e}_4$ and one to $\hat{e}_S \equiv \hat{e}_2$. In order to compare linear and nonlinear spectra, it would be useful to keep these two vectors parallel between them. In this case, the effective susceptibility χ_{eff} will be proportional to R^2.

1.6 The optically induced Dynamic Gratings.

The Four Wave Mixing phenomena could be understood within another formalism too, completely equivalent to the Nonlinear Optics, which has, perhaps, the merit to be more intuitive and physically concrete: the optically induced Dynamic Gratings [5].

In this framework, two waves interact inside the material and change its index of refraction. This change is periodic and it follows the behaviour of the interference pattern generated by the waves. This pattern could be permanent, as in the case of a photo-sensitive material, or dynamic, i.e. it vanishes in some time, once the incident waves are vanished.

A periodic change of the index of refraction is nothing but a diffraction grating, whose presence can be, thus, verified by sending on the material a third beam which will be diffracted by the grating into another direction.

The two beams which produce the pattern (Pump beams) and the beam which has to probe the grating amplitude (Probe beam) play the same role as the fields $\vec{E}_{1,2}$ and $\vec{E}_3$ respectively in the Nonlinear Optics formalism, while the diffracted beam will be the fourth field, i.e. the FWM signal.

A change in the optical properties of a material is caused, in general, if an element of the system goes out from the thermal equilibrium, and this element can couple with the index of refraction or with the absorption coefficient.

For instance, the light absorption can populate many electronic excited states, and these populations will follow, in turn, the periodic interference pattern. This case is called population density grating. During the decay of these electronic excited states, many other lower energy states can be populated, leading to a secondary grating, and, at higher times, the system can locally thermalize, and a thermal grating can be achieved too. In this case, the change of the index of refraction is induced by its dependence on temperature.

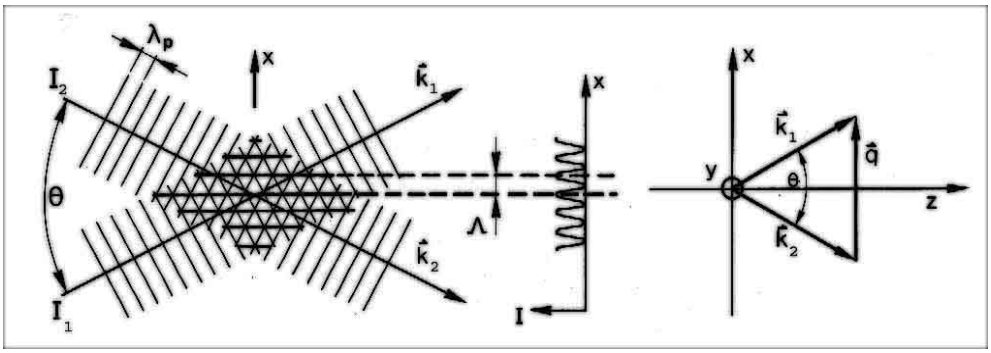

Figure 1.5: Scheme of a dynamic grating [5].

If this changes in the optical properties are not permanent, the system will come back to the initial state, after the disappearance of the applied fields, with a certain characteristic time (see App. B). It can be, for instance, related to the excited level lifetime, or to some other, more complex, mechanisms.

This characteristic time can be easily measured by delaying the third beam (Probe) with respect to the first two (Pumps). A progressive decreasing of the diffracted beam intensity will be observed as the delay increases, and this is a direct measurement of the decreasing rate of the optically induced dynamic grating.

This is a kind of Pump&Probe technique, which, in general, consists of causing an excitation with a very strong laser beam (Pump) and to subsequently probe its temporal decay by a second, weaker and delayed, beam (Probe).

Let us, now, give a brief overview on the formalism of the Dynamic Gratings.

In Fig 1.5, an interference grating picture is shown. It is formed by two beams whose intensities are I_1 and I_2. Let us suppose, for the moment, that these beams have parallel polarizations and the same wavelength λ_p. Their wave-vectors are $\vec{k}_1$ and $\vec{k}_2$, and they form an angle θ. The grating vector is thus

$$\vec{q} = \vec{k}_1 - \vec{k}_2,$$

and so the grating-step is

$$\Lambda = \frac{2\pi}{|\vec{q}|} = \frac{\lambda_p}{2\sin\frac{\theta}{2}} \overset{\theta\to 0}{\approx} \frac{\lambda_p}{\theta}.$$

Assuming that the electric field, in the superposition volume, is a plane-wave, we have

$$\vec{E}(\vec{r},t) = \frac{1}{2}\vec{A}\ \exp[i\,(k_z z - \omega_p t)] + c.c.$$

with

$$\vec{A} = \vec{A}_1 \exp[ik_x x] + \vec{A}_2 \exp[-ik_x x],$$

where k_x and k_z are the absolute values of the components of the wave-vectors $\vec{k}_1$ and $\vec{k}_2$, according to the Cartesian reference shown in the figure.

The intensity of the total field will be

$$I = \frac{n}{2}\varepsilon_0 c\left(\vec{A}\cdot\vec{A}^*\right) = I_1 + I_2 + 2\Delta I\cos(2k_x x),$$

where

$$\Delta I = \frac{n}{2}\varepsilon_0 c\left(\vec{A}_1\cdot\vec{A}_2^*\right).$$

The ΔI parameter represents the amplitude of the interference oscillations, and it is directly proportional to the photo-induced grating amplitude, in the case of isotropic media. Note that ΔI vanishes when $\vec{A}_1 \perp \vec{A}_2^*$, and so the grating cannot be formed if the two beams have orthogonal polarizations. This is strictly true for an isotropic medium, but in an anisotropic one, the coupling between orthogonal polarizations is possible, because of the tensor nature of the dielectric constant.

Thus, it is more correct and complete to define an interference tensor as follows:

$$\Delta M_{ij} = \frac{1}{2}\varepsilon_0 c\left(\vec{A}_1\right)_i\left(\vec{A}_2^*\right)_j$$
$$\Delta I = \left|\mathrm{Tr}\left\{\Delta M\right\}\right|.$$

Moreover, it is possible to generalize the interference tensor in the case of pulsed beams, with a standard Gaussian time-shape:

$$I_{1,2}(t) = \hat{I}_{1,2}\exp[-\left(t \pm \tau/2\right)^2/t_p^2],$$

where τ is the relative delay between the two pulses, t_p is its time-constant, equal for both, and $\hat{I}_{1,2} = \frac{1}{2}\varepsilon_0 c\hat{A}_{1,2}^2$ are the peak intensities. The interference tensor, in this case, will be

$$\Delta M_{ij}(t) = \frac{1}{2}\varepsilon_0 c\hat{A}_{1,i}\hat{A}_{2,j}^*\exp\left[-\frac{\tau^2}{4t_p^2}\right]\exp\left[-\frac{t^2}{t_p^2}\right].$$

Note that the tensor has the same Gaussian time-shape of the pulses which induced it, but its amplitude depends on the factor $-\tau^2/4t_p^2$, i.e. on the time superposition of the two pulses.

Let us call X any quantity (as temperature, population density, a spatial distribution of excited molecules and so on), which is coupled with the applied field and with the index of refraction. We can imagine, as a first approximation, a linear relationship[9] between a variation of X and the variation of the grating amplitude:

$$\Delta X_{ij} = g_{ijkl}\Delta M_{kl},$$

where g_{ijkl} is an appropriate coupling tensor. It is possible, finally, to write the index variation[10] which corresponds to the variation of X:

$$\Delta\tilde{n} = \frac{\partial\tilde{n}}{\partial X}\Delta X,$$

[9] the relationship can be scalar or tensorial depending on the nature of X.
[10] the variation of $\tilde{n}$ is more complicate if X is a tensor.

where $\tilde{n}$ is a complex index of refraction. The imaginary part of $\tilde{n}$ represents the absorption coefficient, which takes part, in turn, to the formation of the grating.

Keeping in mind the well-known relationships

$$\tilde{n}^2 = \varepsilon = 1 + \chi$$
$$\Delta\tilde{n} = \frac{\Delta\varepsilon}{2\sqrt{\varepsilon}} = \frac{\Delta\chi}{2\sqrt{1+\chi}}$$

it is clear that the grating can be regarded as a variation of $\tilde{n}$ as well as ε or χ.

At this point, we can find the link with the Nonlinear Optics formalism. The variation of the polarization, which is induced by the grating, can be written as

$$P_i = \varepsilon_0 \chi_{ij} E_j \Rightarrow \Delta P_i = \varepsilon_0 \Delta\chi_{ij} E_j.$$

It becomes the third order correction of the polarization (Eq. 1.1), by assuming the following relationship

$$\Delta\chi_{ij} = \chi^{(3)}_{ijkl} E_k E_l.$$

Let us now consider a third beam, having a wave-vector $\vec{k}_3$ which will be diffracted by the grating. From the Bragg law, we have

$$\vec{k}_m - \vec{k}_3 = m\vec{q}; \quad m = 0, 1, 2, 3... \tag{1.26}$$

Eq. 1.26, limited to the first diffraction order ($m = 1$), is nothing but the phase-matching relationship between the four involved waves (Eq. 1.23).

If the two pump beams have different frequencies, the only change which must be made is that the amplitude of the grating will vary with time, and this will result into a moving grating:

$$\vec{E}_{1,2}(\vec{r}, t) = \frac{1}{2}\vec{A}_{1,2} \exp\left[i\left(\vec{k}_{1,2}\cdot\vec{r} - \omega_{1,2}t\right)\right] + c.c.$$
$$I \propto \left|\vec{E}_1 + \vec{E}_2\right|^2 \propto I_1 + I_2 + \left(\vec{A}_1 \cdot \vec{A}_2\right) \exp i\left[\vec{q}\cdot\vec{r} - \Omega t\right] + c.c.$$

where $\vec{q} = \vec{k}_1 - \vec{k}_2$ and $\Omega = \omega_1 - \omega_2$. Note that the probe beam, which is diffracted by the grating, will be frequency shifted by the quantity Ω, according to Eq. 1.21. This shift is interpretable, within the Dynamic Gratings formalism, as a Doppler shift. It is due to the motion of the grating itself, which acts as a moving light source.

In this case too, the intensity modulations bring to a dielectric constant variation:

$$\Delta\varepsilon = \chi^{(3)} \left(A_1 A_2^*\right) \exp i\left[\vec{q}\cdot\vec{r} - \Omega t\right] + c.c. \tag{1.27}$$

Inserting Eq. 1.27 into the linear wave-equation, we have

$$\left(\nabla^2 - \frac{\varepsilon + \Delta\varepsilon}{c^2}\frac{\partial^2}{\partial t^2}\right)\vec{E} = 0$$

This wave-equation leads to the same nonlinear coupled system just discussed in the previous sections.

Chapter 2

Superconducting Cuprates: an overview.

Since their discovery, many theories have been proposed in order to explain the remarkable features of cuprates superconductors. Notwithstanding these efforts, and the huge number of experimental data which have been collected in these years, many questions are still open. For these reasons, this Chapter cannot be a clear report on a closed subject. It has to be taken, instead, as a brief overview on this fascinating matter, in order to understand what we know and what we do not know about the high T_c superconductivity. Most of the notions presented here can be found in refs [7] and [8].

2.1 The discovery of high-Tc superconductors.

In 1986, Bednorz and Muller [43] discovered that a perovskite-like compound, based on the copper and lanthanum oxides and rightly doped with calcium atoms, shows a superconductive behaviour with a very high critical temperature (T_c): about 30K.

Such a temperature was already sufficiently high to be hard to explain it in the framework of the BCS theory (see App. C), but very soon, on the wave of this discovery, many other similar compounds were found, whose critical temperatures were even higher. The following year, a compound, based on yttrium and barium, was found [6], whose critical temperature was higher than the liquid nitrogen temperature: this had a huge impact on the scientific community, since this compound opened the route to every future concrete applications of the superconductive technologies. Before this discovery, the cooling equipment were too much expensive to allow a large scale use of the superconductive technology.

These new materials took the name of High-Tc Superconductors (HTCS) or Cuprates Superconductors, since the copper-oxide is present in all of them.

Beside the anomalous value of T_c, the cuprates present a very wide range of common features which make them very different from the normal BCS superconductors: first of all, they have a layer structure, i.e. they contain lattice planes with the chemical formula CuO_2, orthogonal to the $c-$axis. In these planes there is the most part of the conductive charge carriers. The strong localization of the

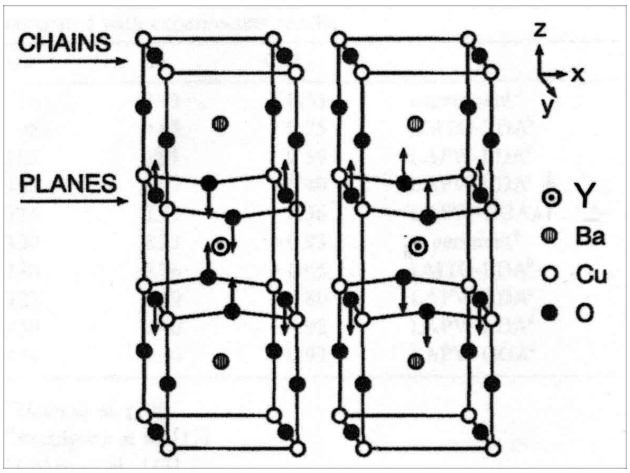

Figure 2.1: The unit cell of YBCO and its normal modes [25].

mobile carriers in these planes makes the contact between a plane and the other very weak, and this is the reason of the strong anisotropy of many properties of cuprates. Up till now, it is believed that these planes are the "natural" place of the high temperature superconductivity.

Secondly, the charge density in cuprates is very much smaller than in normal metals, so that the carriers are less screened and more sensitive to the Coulomb interaction between them.

Moreover, they have a coherence length very much shorter than normal superconductors (about 2 nm in the planes and 0.3 nm along the $c-$axis). This makes the thermal fluctuations and the scattering from impurities, or imperfections, more important.

Finally, all cuprates are very sensitive to the doping, which allows them to go through several phases and to change dramatically their conductive behaviour, even above T_c, as will be shown in the following.

2.2 The structure of cuprates.

In Fig 2.1 and 2.2 a schematic picture of the unit-cell of $YBa_2Cu_3O_{7-\delta}$ (YBCO), one of the most studied superconductive cuprates, is shown as a typical example of a cuprate-like structure.

Generally speaking, all cuprates have a tetragonal perovskite-like structure[1]. The main feature of the unit-cell is, as previously mentioned, the CuO_2 superconductive planes in the lattice plane $a-b$, which are bidimensional square lattices with a side-length of approximately 0.38 nm. This value, slightly lower than expected for ionic bonds, suggests that the nature of these planes would be, at least partially, covalent.

[1] $a = b \neq c$; $\alpha = \beta = \gamma = \pi/2$.

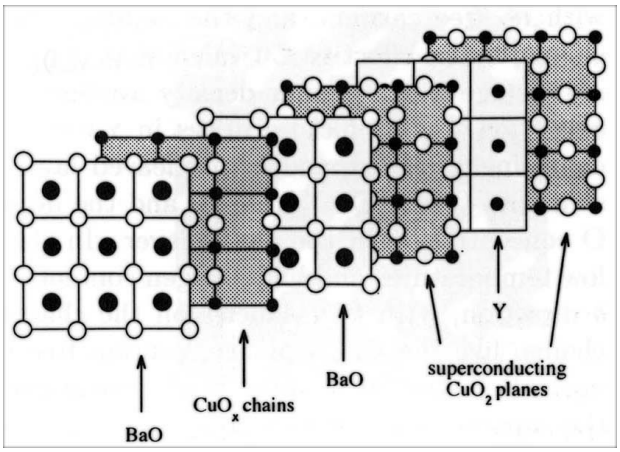

Figure 2.2: Planar development of the YBCO unit cell [25].

The CuO_2 planes are separated by some AX planes (where X is usually an oxygen atom) so that the oxygen coordinates the copper atoms of the CuO_2 planes as happens into a typical perovskite unit-cell.

The electronic state of the CuO_2 planes depends on doping. Let us consider first the so-called "parent-compound", i.e. the undoped compound. Its copper atoms of the CuO_2 planes have a $+2$ valence, while oxygens have -2, so that each plane has a net -2 charge for each unit-cell. Usually, the AX planes have a positive charge which compensates the negative charge of the copper-planes.

There are two possible kind of doping: if an excess of negative charges (electrons) is provided to the system, the material will be n-doped ($Nd_{2-x}Ce_xCuO_{4-\delta}$ or NCCO is a prototype material of this class), while p-doped materials are doped with an excess of holes.

In this work, we will point our attention exclusively on the last case, since the increase of a negative charge concentration makes the material more similar to a normal metal, and thus less interesting from the superconductive point of view. For instance, n-doped materials have critical temperatures very much lower than the p-doped ones.

The doping is usually made by the substitution of cations in the AX planes with others having different valence (for instance putting Sr^{2+} in the place of La^{3+}) or by changing the oxygen concentration, as in the case of YBCO.

Since the AX planes have a ionic nature, the doping modifies the valence of the copper atoms in the CuO_2 planes so that the charge carriers density, in that planes, is modified.

The case of YBCO and related compounds is slightly different, since their structure can be sketched as $(BaO)(CuO_x)(BaO)$ and the doping is done by changing the x value. The stable configuration of the CuO_x planes have some $Cu-O$ chains along the crystal axis b, with some oxygen vacancies along them. Thus, the chain carriers are free, and they give a contribution to the conduction.

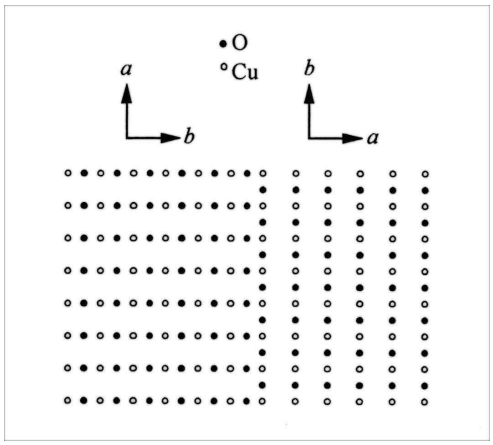

Figure 2.3: The twinned structure of $a - b$ planes.

The copper-oxygen chains make the lattice orthorhombic (with $b > a$), but, at high temperatures and low oxygen concentrations, the oxygen position in the planes and chains becomes disordered, and the lattice becomes tetragonal (with $a = b$).

Since the growth of these materials is done at very high temperatures, the crossing from the tetragonal to the orthorhombic structure generates a strong internal stress. This results in an orthorhombic domains crystallization: each domain have a and b axis exchanged, compared to adjacent domains. This phenomenon, whose schematic picture is shown in Fig 2.3, takes the name of "twinning".

Using some rather complex techniques, it is even possible to obtain an "untwinned" sample, i.e. with a unique (a, b) orientation along the whole crystal.

In the last years, the knowledge about the growth of these materials, bulk monocrystals or thin films, made a very fast progress, and high quality single crystals (with some millimeters side) or very thick films (about 1 μm) are now available.

2.3 Electronic states and phase diagrams.

The largest difficulties in the understanding of the mechanism leading to the high-Tc superconductivity in cuprates derive from the poor knowledge we have about their "normal state". For them, the expression "Non-Fermi Liquid", whose sense will be clarified in the following, was coined. In particular, one has to understand that the very strong correlations between the quasi-particles (electron and holes) play a crucial role in the physics of such complex systems ([7],[8]).

Outside the CuO_2 planes, experimental evidence suggests the presence of strong ionic bonds. Electron are, thus, strongly localized near their atoms, into orbitals whose energies is lower than the Fermi level. Their role into the conductive dynamics seems to be completely negligible.

In the planes, as well as in the CuO chains, it is reasonable to start from the standard electronic configuration of the copper and oxygen atoms as it is in the parent compound. The copper is in the Cu^{2+} state, while the oxygen is in the O^{2-}

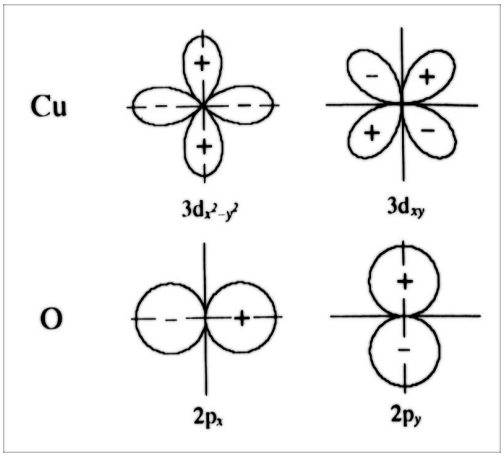

Figure 2.4: Copper and oxygen orbitals involved in the electronic state of cuprates [7].

state. The external electronic configuration is, thus, $3d^9$ (with one hole) and $2p^6$ (full shell) respectively. In total, we have 11 orbitals (5 d-orbitals from the oxygen atoms and 3 p-orbitals from the copper) for each unit-cell and they have to be used as the fundamental bricks in order to build the electronic state of the system.

Beside removing the degeneration, the surrounding lattice creates many bands (even superimposed), but, since there is only one hole per unit-cell, only one of these bands can be partially filled. It is, thus, reasonable to expect that the Fermi energy intersects only the highest energy band. Since the charge carriers are localized almost solely in the (a, b) plane, it is logic to consider those orbitals, whose lobes lie in that plane, as participants in the building of a concrete depiction of the normal state electronic structure (as shown in Fig 2.4). In this framework, the doping has mainly the effect of removing one electron (or hole, in the case of n-doping) from the CuO_2 planes. For instance, in the $La_{2-x}Sr_xCuO_4$ compound the substitution of a La^{3+} ion with a Sr^{2+} one creates $n_d = 1 - x$ holes, placed in each CuO_2 plane. The same can be done by filling the oxygen vacancies with O^{2-} ions. In the case of YBCO, the situation is slightly complicated by the presence of the $Cu - O$ chains. Assuming an equal distribution of the holes between planes and chains, we have $n_d = 4/3 - 2\delta/3$ holes per unit-cell.

We have already said that the electronic properties of cuprates are extremely sensitive to the doping. In Fig 2.5 the phase diagram of YBCO is shown as a function of the oxygen concentration. This diagram is qualitatively very similar in all cuprates. For low oxygen concentrations, the material has a tetragonal structure and it is an antiferromagnetic insulator. As the oxygen concentration increases, the Neel temperature (i.e. the antiferromagnetic transition temperature) decreases until a critical doping value is reached. Above this value, the material becomes mainly orthorhombic, and its conductive behaviour is closer to a normal metal than an insulator. In this phase, the material become a low temperature superconductor.

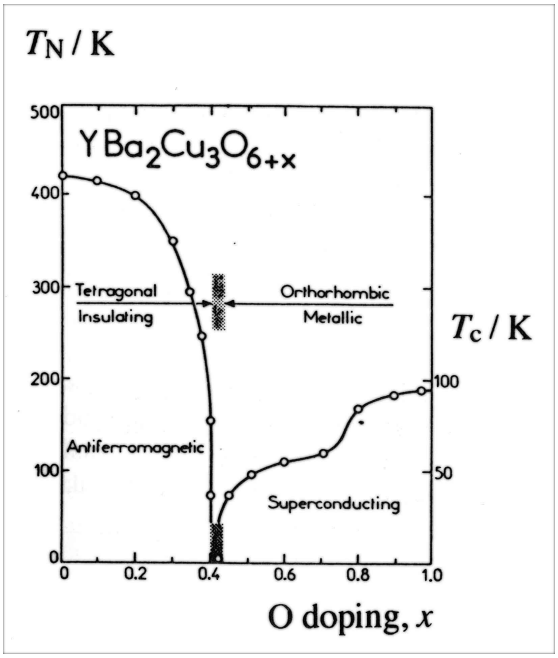

Figure 2.5: Phase-diagram of YBCO [7].

Continuing to increase the doping, the metallic features become more marked and the critical temperature rises more and more until it reaches its peak at about 93K for $x \simeq 1$. In this case the material is called "optimal doped". After the peak, the critical temperature decreases until it vanishes.

A quite accurate description of this behaviour is given by the empirical formula in Eq. 2.1

$$\frac{T_c}{T_c^*} = 1 - \left(\frac{n_d - 1.15}{0.10}\right)^2. \tag{2.1}$$

Nevertheless, the tetragonal-orthorombic transition has not clear connection with the insulator-metal transition, and it appears in different positions, depending on the sample.

Such a strong dependence of the inmost nature of the material on its chemical composition makes, thus, evident that the first experimental difficulty in studying the cuprates, is just to have a good sample-to-sample reproducibility, i.e. to obtain a controlled procedure which allows a good reproducibility between different samples.

All these considerations prevent from a passive application of the free-electrons model, as it is applied in normal metals. The presence of the insulator-antiferromagnet transition makes very clear that the interaction between electrons is nothing but negligible.

Suffice it to say that the parent compound, having an empty half upper band, would be a metal, in the free-electron gas theory. Actually, the parent compound is not strictly an insulator. This kind of insulators are known as "Mott insulators".

In a Mott insulator, the not negligible Coulomb interaction opens a gap inside the conduction band, so that it is divided into two parts, one full and one empty. This confers the insulating nature to the material. The intuition can help to have a naïve image of what happens into a Mott insulator: each electronic site contains only one electron, so that another one, with opposite spin, could be added to the system without breaking the Pauli principle. This does not happen, because of the excessive energetic cost caused by the strong Coulomb repulsion. Moreover, this means that the electron has the possibility to freely change its spin, leading to some very particular magnetic features of cuprates.

Nevertheless, it is true that, for some doping levels, the cuprates show several quite marked metallic features (for instance, the specific heat follows the typical free electron gas behaviour). Thus, it can be useful to have an idea of what the free electron theory predicts in these materials.

The electronic wave-function is made mainly by the copper orbitals $3d_{x^2-y^2}$, strongly hybrided with the oxygen orbitals $2p_x$ and $2p_y$: looking at Fig 2.4, it is possible to see that these orbitals present quite superimposed lobes. This leads to a quite large bandwidth (about 2 eV) and an effective mass quite similar to the free electron mass m_e.

The upper zone of the band is close to the reciprocal lattice limits $ak_x = bk_y = \pi$, where the superposition of the orbitals forms an anti-binding combination; this produces, in the Fermi surface, an approximately cylindrical hole. These holes are centered in the Brillouin zone (BZ) angles, and their area is about the half of the BZ area (as shown in Fig 2.6).

By means of the Hartree-Fock method, it is possible to consider the averaged effect of the electron-electron interaction and also the spin correlation effects, but not the correlations effects due to the effective instantaneous positions. The highest energy band is very similar in all cuprates: the superposition between a CuO_2 plane and the other is very small, and the charge carrier density is concentrated mainly into those planes; the energy band and the electron scattering cross-section are almost independent of the z component k_z of the crystal momentum $\vec{k}$, and this can explain the experimental evidence of a strong anisotropy in all the transport properties.

In YBCO, and related compounds, we have a similar situation for the CuO_2 planes, but there are also the electronic states of the $Cu-O$ chains. In this chains, the energy is almost independent both of k_x and k_y. The electrons are, thus, strongly localized into an almost monodimensional system.

In Fig 2.6, it is seen that the band (i) is nothing but an monodimensional version of the previously mentioned CuO_2 planes band, while the band (ii), which has a smaller orbital superposition, has a lower energy and bandwidth. In this case too, anti-bonding combinations of adjacent orbitals are found near the maxima of the band. Finally, the Fermi energy can intersect the band (ii) only when the hole density value crosses the optimal doping value. This induces to think that this band plays a minor role in the superconductive dynamics.

These are only qualitative features, which should be roughly valid also taking into account the electronic correlations. This correlations will play, instead, a crucial role into the real dynamics inside planes and chains.

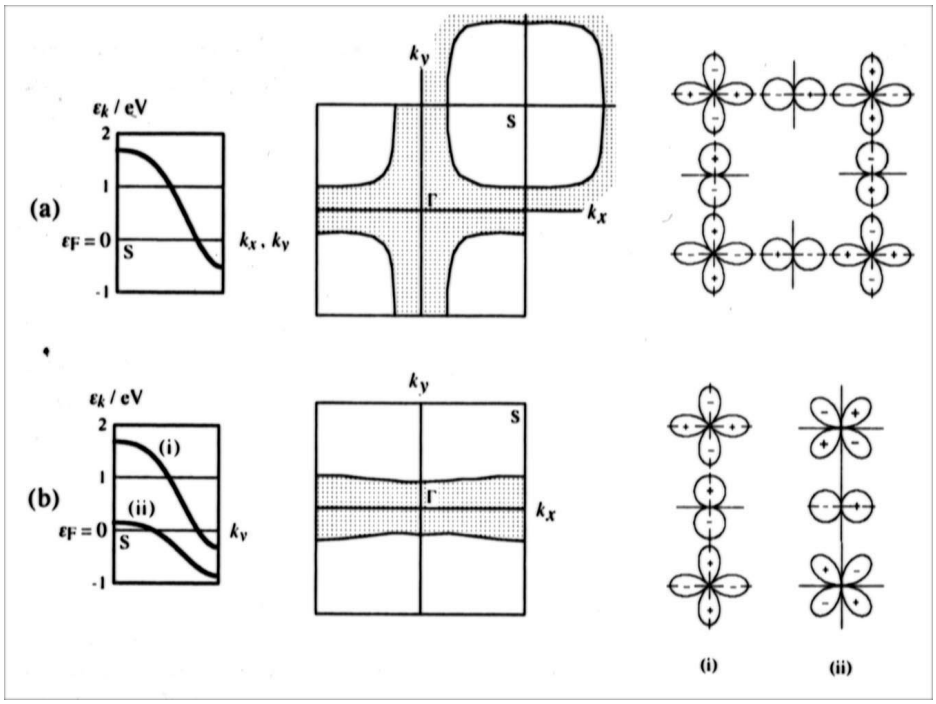

Figure 2.6: Band structures, Brillouin zones and orbitals of planes (a) and chains (b) [7].

In an ideal free-electron gas, it is important to distinguish between two different regimes: high and low electronic densities. Being r the mean electronic distance, the Coulomb interaction energy is $e^2/4\pi\varepsilon_0 r$, while the zero-point kinetic energy is $\hbar^2 k^2/2m_e \approx \hbar^2/2m_e r^2$. This means that the kinetic energy prevails for small values of r. In other words, at high densities, the electron has a well-defined momentum and it has a large wave-function. It extends over the whole available volume, since it has enough energy to overcome, by means of a tunnel effect, the potential barrier formed by its neighbours. At low density, the electron is confined into the potential hole created by the interaction with its neighbours and it has a very much localized state: this localization generates a Mott insulator. The cross point between these two regimes is for $r \sim a_0$, i.e. when the mean distance between two electrons is of the order of magnitude of the Bohr radius. This is exactly the case of the hole gas of cuprates.

Into a crystal, we should take into account the presence of the lattice too, i.e. the atomic potential, generated by the lattice ions. This can be obtained with the Hubbard model, which makes provision for only one atomic orbital for each lattice site. The Hubbard Hamiltonian is

$$H = -t\sum_{i,j,\sigma} c^{\dagger}_{i\sigma} c_{j\sigma} + U\sum_{i} n_{i\uparrow} n_{i\downarrow}, \tag{2.2}$$

where i is the reticular site index, j is the first neighbour index, σ is the spin index, the operator $c^{\dagger}_{i\sigma}$ inserts an electron into the atomic orbital of the i-site with spin σ.

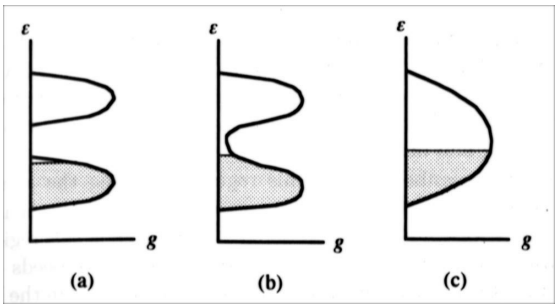

Figure 2.7: Scheme of the Hubbard-to-conduction band transition [7].

U is the Coulomb energy which must be added when two electrons are on the same site with opposite spins and $-t$ is the tight-binding theory superposition integral. Often, this model is substituted by the so-called "$t-J$" model, where $J = 2t^2/U$ is the magnetic interaction strength.

Note that, for $U = 0$, one obtains the usual tight-binding band with a bandwidth equal to $2Nt$ where N is the number of first neighbours in the lattice, while for $U \gg t$ one obtains an antiferromagnetic ground-state. This is in quite good agreement with what observed in the parent compound. Thus, the Hubbard model can include both the high and low densities regimes.

Nevertheless, it is not clear what happens at the cross point, i.e. how an apparent metallic state could emerge with a very slight addition of holes. Once more, the model can give us only a qualitative picture of what is going on. In Fig 2.7, the occupation number (g) as a function of the energy (ε) at three different doping levels (a,b,c) is shown. At low doping (a), we have the so-called Mott Hubbard bands: when an electron is added to the system, it will go into an occupied orbital (since the external orbital of copper is $3d^9$ it has only one free hole) and the energy will be positive shifted by a quantity equal to U. It is possible to prove that an opportune linear combination of these states leads to an extended band with a well-defined momentum (upper Hubbard band). A removal of an electron from its site will correspond to the creation of a hole in the lower Hubbard band.

At higher doping (b), we can expect something similar to what happens in a doped semiconductor, i.e. the appearance of bound states inside the gap. These states can form the so-called "impurity band", since the excess of doping-charges are preferentially localized near some impurities. As the doping increases (c), the intersection between these bands increases, and the bound states can lead to an "hopping conduction", i.e. the electron can jump from a state to another, being, in practice, almost a free-carrier.

Viceversa, we can start from a tight-binding theory, without interactions, and ask ourselves what happens as the electronic interaction becomes more and more important. It is not clear at what level of interaction the theory falls down: it is possible that some hole band is formed with a gradual transition from the Fermi liquid (c) to the Hubbard bands. In this case, it is necessary a theory which must describe quite in detail the mobility near the Fermi energy.

It is also possible that in this doping range, the quasi-independent particles model could be definitively useless, and that a new theory of superconductivity could emerge solely from the inter-electronic interaction, without the phonon-mediated attraction, as prescribed by the BCS theory (see App. C).

Unfortunately, up till now the experimental data are not able yet to clarify if the doped material has a Fermi surface in agreement with the one we can calculate from the free-electron gas model. ARPES (Angular Resolved Photo-Emission Spectroscopy) measurements [9] seems to be in good agreement with this hypothesis, but EELS (Electron Energy Loss Spectroscopy) data indicate, with some clarity, that the low-doping Hubbard bands are partially superimposed, but the Mott insulator behaviour does not vanish completely at higher doping level. Another apparent paradox is given by some thermodynamical measurements: in the doping range where ARPES data show the presence of a Fermi Liquid, the ratio between the electronic specific heat and the temperature is constant (equal to γ) as expected, but the ratio between the entropy and the temperature is not constant at all, since it depends again on temperature and on the doping. This could be explained only if one supposes that the fermion density of states changes abruptly in correspondence to the Fermi level.

This experimental evidence gave birth to the concept of "pseudogap". On this subject, see §2.7. Also the neutron scattering measurements gave unexpected results. For instance, there is a characteristic peak of a spin-excitation in the antiferromagnet-phase which remains visible, although very weak, also at those doping values where the antiferromagnetic behaviour is completely vanished, as shown in Fig 2.8 (a).

Also the neutron absorption spectrum has a particular feature: it seems that, below T_c, neutrons can generate magnetic fluctuations only above a certain energy threshold. This threshold took the name of "spin gap" and its value is very close to the one predicted for the usual BCS gap ($3.52kT_c$).

2.4 Transport properties.

The transport properties of superconductive cuprates have many remarkable features.

First of all, the spatial charge distribution is strongly anisotropic. In order to simplify the problem, let us start from the assumption that the conduction is ruled by one kind of charge carrier, and that it is almost isotropic in the (a, b) plane. In this plane, the conductivity is usually given by

$$\sigma = ne^2\tau/m^*,$$

where n is the carrier density, m^* is the effective mass and τ is relaxation time of the current density, due to lattice scattering.

The electric resistivity $\rho(T)$ as a function of temperature, shown in Fig 2.9 for several doping values, scales linearly with T, when it is far from T_c, only if the doping value is near the optimal doping. For lower values, $\rho(T)$ assumes a positive curvature until, in the antiferromagnetic zone, it increases abruptly, as the

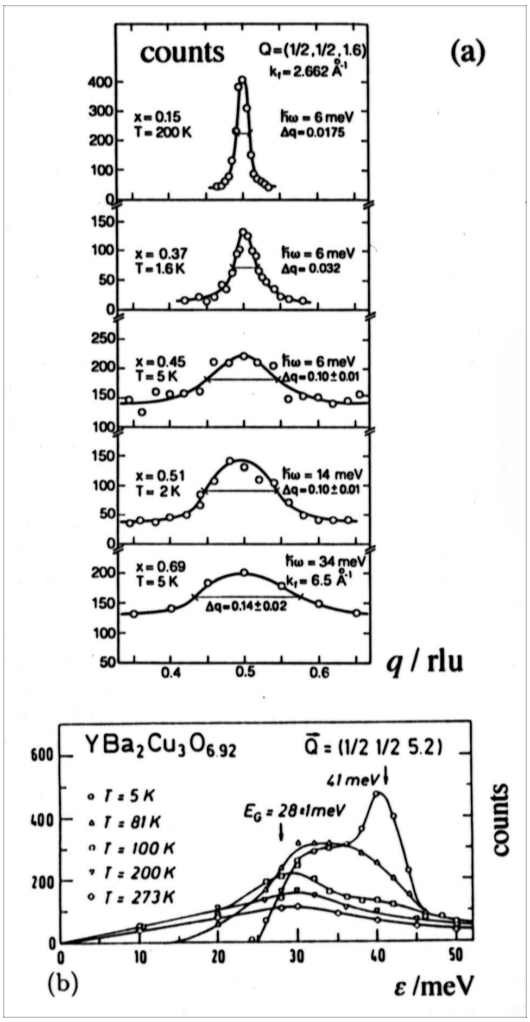

Figure 2.8: Neutronic scattering measurements on YBCO [7].

temperature decreases. This is not surprising if the material is enough doped to be an antiferromagnetic insulator (when the low-temperature hopping-conduction is "freezed"), but a positive curvature remains visible even for doping regions where we are used to think at the material as a metal. Even if the optimal doping is exceeded, $\rho(T)$ has a positive curvature. It obeys to a perfectly quadratic behaviour only when the superconductivity has now vanished.

In the YBCO-like compounds there is also a small anisotropy in the (a, b) plane due to the $Cu - O$ chains. Very fine measurements, on untwinned crystals, showed that the $b-$axis conductivity is about double compared to the $a-$axis one in a optimal doped sample, but its variation with temperature is the same in both directions.

The resistivity along the $c-$axis is, as expected, higher than the one in the plane. Moreover, it is very sensitive to the doping variation and to the inter-planes distance: different compounds having different inter-planes distances may have five orders of

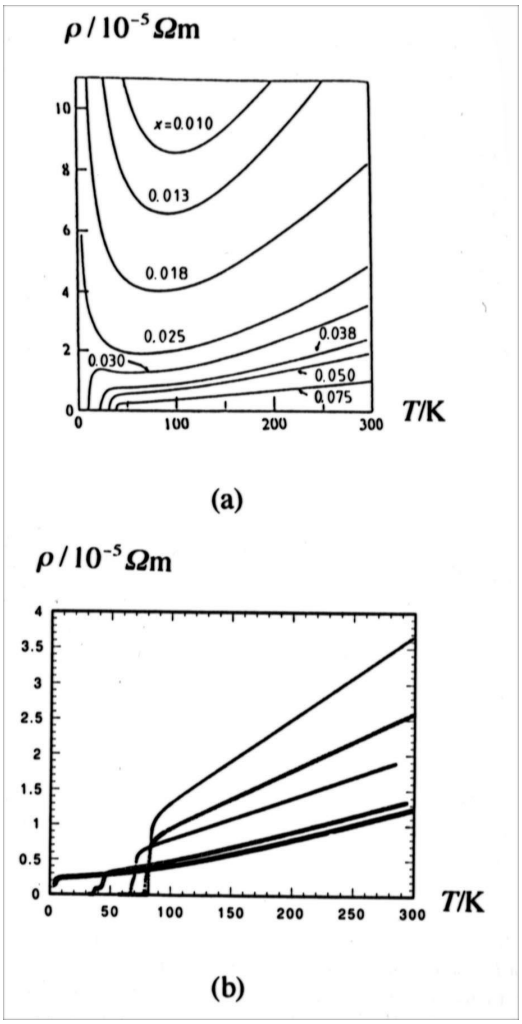

Figure 2.9: Electric resistivity as a function of temperature [7].

magnitude different $c-$conductivity.

Along this direction, it is likely to suppose a tunnel effect conductivity between two planes. The major difficulty in direct measurements of this kind, is that the $c-$conductivity is strongly sensitive also to small inter-planes defects.

In order to understand the transport properties of cuprates, the crucial problem lies, once more, on the charge carrier density. In particular it is necessary to understand if this density varies strongly with doping or not. On the one hand, Hall effect measurements and infrared conducibility data show that the charge carrier density varies strongly both with doping and temperature. This suggests a transition between the Hubbard and the conduction band. On the other hand, ARPES measurements on the Fermi surface, supported by thermal capacity and magnetic susceptibility data, seem to show that the charge carrier density is almost constant in a wide range of doping.

This remarkable discrepancy can be partially overcome by keeping in mind that the weak-bound states contributes to the ARPES reconstruction of the Fermi surface but not to the pure electronic properties, as the Hall effect does. Nevertheless, these considerations are not sufficient to quantitatively match this two aspects. A possible suggestion was made by Cooper [10], in order to have an almost constant Fermi surface, without requiring the localized states: its assumption is that the electrons can have different kind of scattering in different zones of the Fermi surface. In particular, the so-called "nested Fermi surface" would be made by several faces, more or less flat and parallel, with strong variations of the curvature in some points ("angles"). The model's hypothesis is that, in the flat zones, the electron scattering is mainly ruled by the spin-fluctuations (being proportional to T), while in the angles it is a normal electron-electron scattering (being proportional to T^2). This model seems to work quite well, but it depends on a "special combination" of several different effects. Moreover, it does not match completely with some EELS measurements and it leaves open the question about the Hubbard–to-conduction band transition. Nowadays, this question is still open.

2.5 BCS theory and cuprates.

When the BCS theory (App. C) is applied to cuprates superconductors, one has to note first that it cannot be applied in its usual form, even in the roughest approximation. The reason is that the usual BCS theory is an $s-$wave theory (fully isotropic) and, thus, it cannot account for the strong anisotropy of these systems. Moreover, in the YBCO-like compounds we should understand if the chain-electrons (which are, as seen before, almost decoupled from the plane ones) participates in the condensation and, if yes, in which way.

Since the coherence length along the $c-$axis is very small (of the same order of magnitude of a unit-cell), one can regard this system as an almost pure bidimensional, one with a weak plane-to-plane interaction described mainly as a superconductor-superconductor Josephson junction. Nevertheless, since the tunnelling based experiments give informations which are averaged on several coherence lengths, it is a quite hard task to compare the theory with this kind of data.

Note that a real bidimensional superconductivity theory is excluded *a priori* from the general Mermi-Wagner theorem, which asserts that the generic bidimensional system cannot present a symmetry-breaking at a finite temperature. It is possible to prove that the phase-fluctuations of the order parameter below T_c go as $1/k^2$: the sum of these fluctuations on a set of bidimensional modes diverges, while this does not happen in three dimensions. In other words, the phase of the order parameter is intrinsically incoherent in two dimension, and the system loses its superconductive properties.

The weak coupling between the planes has to be considered far from being a small perturbation. It plays, instead, a crucial role in the condensation; it allows the locking of the order parameter phases between different planes, and it preserves the coherence of the whole system.

Also the $a-b$ plane coherence length ξ_{ab} is very much lower (~ 2.5 nm), compared to the normal superconductors one. This makes very much important the thermal fluctuations effects as well as the local defects of the compound. The superconductive properties must have, thus, many local variations, while the normal superconductors are almost insensitive to the defects or impurities, in the superconductive phase.

The usual BCS theory requires a well-defined energy-gap (where the density of states has a well-delineated peak), while experimental evidence in cuprates shows the presence of bound states near the Fermi energy. Moreover, a possible $d-$ or $p-$wave BCS theory would lead to a strong variability of the gap-value, which should vanish in the nodal points, and this is not supported by any experimental evidence. The magnetic order have to play an important role too, since the antiferromagnetism (due to a long range magnetic order) disappears as the doping increases, but a certain short range magnetic order seems to persist. Finally, also if it should be possible to write a BCS like wave-function, we have to keep in mind that the attractive mechanism will be very much different from the weak electron-phonon-electron interaction which is usually accepted as the base of the Cooper's pairs creation.

The thermal capacity, measured as a function of temperature in YBCO for different oxygen concentrations, clearly shows that the electronic entropy is abruptly reduced below T_c. This could mean that all electrons, including the chain-electrons, participate to the condensation. But the same measurements show that the entropy is not so reduced as the $s-$wave BCS theory predicts, and this could be a first support to a $d-$wave theory. The same measurements on zinc-doped YBCO show that a certain fraction of electrons are in the normal state also for $T = 0$, and thus they are not involved in the condensation. This leads to think that the zinc atoms create electronic states, localized near the zinc sites, whose energy is lower than the energy-gap value. The low carrier density of cuprates produces a large magnetic field penetration length λ (for instance, in optimal doped YBCO at $T = 0$, $\lambda_{ab} \sim 1.3 \times 10^{-7}$ m and even larger λ_c). This means that cuprates are always in the London limit $\xi \ll \lambda$ and, thus, $\lambda \approx \lambda_L = \sqrt{mc^2/4\pi n_s e^2}$, where λ_L is the London length and n_s is the carrier density. This allows to link the measurements of the penetration length as a function of temperature with the ratio $n_s(T)/n_s(0) = (\lambda_s(0)/\lambda_s(T))^2$. These measurements are in qualitative agreement with the weak-bond BCS theory, but the low-temperature data show a strong bound behaviour, where the $\Delta/k_B T$ ratio is 2.2 instead of the usual value 1.76.

Moreover, in the BCS theory the available number of excitation levels at low temperatures is proportional to $e^{-\Delta/k_B T}$, while in zinc-doped samples the behaviour is quadratic.

The behaviour of λ_a and λ_b is in perfect agreement with the fact that the number of charge carriers along b is double compared with a, since the chain-electrons contribute only along the $b-$direction, and both λ_a and λ_b scales linearly with T (as predicted by a $d-$wave theory). This seem to confirm that the chain-electrons participate to the condensation with an energy-gap not so far from the one of the planes.

The $c-$axis penetration length λ_c is very much larger than λ_a and λ_b. This is not surprising, since the band structure is almost independent from k_z. Moreover, if the sample is doped with cobaltous, whose effect is to ruin the chain structure,

the values of λ_c increases, suggesting that the chains have a crucial role into the plane-to-plane coupling.

The large coherence length in normal superconductors is due to the large wave-function of the pair, and not to the interaction distance between the pairs, which is smaller. The value of this parameter in cuprates resembles the one of superfluid helium $He4$, in which the condensation happens between small bosons.

Actually, cuprates are into a particular condition in which the wave-function width and the interaction distance are quite similar. Their coherence length is not completely out of the BCS theory predictions, since the well-known relationship $\xi = \hbar v_F / \pi \Delta_0$ can give the correct value, if the strong bound $\Delta / k_B T$ ratio is used instead of the weak bound one[2]. The value of ξ_{ab} is, however, still larger than the interaction distance of several boson excitations proposed as possible mediators of the electron coupling.

In normal superconductors, the wavelength which corresponds to the energy-gap is in the range of the millimeters. For cuprates, it falls into the far infrared. This is the reason why it is very convenient to study the infrared response of these materials, being them bulk crystals, thin films of powders. Introducing a complex index of refraction $n = n' + in''$ (i.e. a dielectric constant $\varepsilon = \varepsilon' + i\varepsilon''$), whose imaginary part accounts for the absorption and the real part for the refraction, the reflection coefficient is given by

$$R = \frac{(n'-1)^2 + n''^2}{(n'+1)^2 + n''^2}. \tag{2.3}$$

Measuring this quantity in several cuprates, one finds three different ranges of frequencies: below 10^2 cm^{-1} the reflectivity is very large, as expected for a metal. Over this value, R decreases, since the dielectric constant is no longer ruled by the free-carriers terms: in this zone the opening of the gap is expected. Near 10^3 cm^{-1} there are the optical phonon sharp peaks and, finally, above 10^4 cm^{-1} the plasma frequency is overcome, and the material is transparent.

Using the Kramers-Krönig relationships in order to extract n' and n'' from R, one observes a strong slope, below T_c, near 750 cm^{-1}. It is natural to interpret this spectral feature as the opening of the superconductive gap, but such interpretation gives rise to several difficulties: firstly, its value is larger than those obtained from other independent methods, secondly, this slope persists, although weaker, above T_c too. A much more accurate fit of these data can be achieved by means of the sum of three effects: a Drude-like contribution from the free-carriers, a small range of optical phonon resonances, and a large absorption peak in the middle infrared.

The last contribution is not, up till now, fully clarified. It seems to have a Lorentzian behaviour, peaked at about 1800 cm^{-1}, and it is independent of temperature. These feature can represent some kind of excitation, not directly linked to the free-carriers, but the fact that its width scales with temperature as T_c does, seems to suggest that such excitation plays a role in the superconductivity. The

[2] the Fermi velocity v_F can be calculated from the band structure to be about 1.7×10^5 m/s.

"presumed gap" could, thus, be an artifact, due to the simultaneous presence of these three factors.

Actually, the superconductivity is revealed by the infrared absorption spectra, keeping in mind that their integral is a measure of the total number of electrons which respond to the applied field, and it is thus a constant. This integral is really a constant above T_c, but its value decreases dramatically below this threshold, suggesting that the most part of electrons has gone in the condensate. This approach is not, however, a suitable tool in order to measure the numeric value of the superconductive gap, since the value of n is quite small, and it is hard to extract it from IR data using the Kramers-Krönig relationships.

Since the energy-gap along the $c-$axis is much larger, it should be possible to extract it from this kind of measurements, but any structure is seen, below T_c, in the IR-spectrum. These seems to confirm what previously mentioned: the carrier density in the superconductive state of cuprates does not thicken near the Fermi energy, but presents some kind of underlying localized states.

Another proof is that the so-called "coherence peak" is absent in the high-frequency conductivity measurements. In normal superconductors, this very broad peak is due to the presence of a narrow peak of the BCS density of states, just below the Fermi energy, which produces an enhancement of the scattering rate.

Nevertheless, this result does not have to be read as a trivial failure of the BCS theory, since a $d-$wave theory or a strong electron coupling or spatial unhomogenities can lead to the disappearance of this peak.

On the other hand, as seen before, it is likely that the wave-function has a non-trivial symmetry, since the phonon mediation can carry upon the gap Δ_k the lattice symmetry, giving to it a weak anisotropy. Nowadays, is is accepted that the gap has a $d_{x^2-y^2}$ symmetry, having the nodes at 45° with respect to the a and b axes (in the case of a tetragonal lattice).

2.6 Phonons and other attraction mechanisms.

The phonon spectra of several cuprates have been measured with great accuracy from neutronic scattering measurements for several $\vec{q}$ vectors and with infrared and Raman spectroscopy for $\vec{q} = 0$. The results are well-approximated by the lattice dynamics calculations. Since in the unit-cell there are a lot of atoms, it is easy to expect that the phonon spectrum will be quite complicate.

In the optimally doped YBCO, for instance, we have 36 different vibrational modes for every $\vec{q}$ vector. For $\vec{q} = 0$, we have 15 Raman-active modes and 21 infrared-active modes. The high-frequency modes involve the lightest atom of the unit-cell, the oxygen. For a detailed treatment of the calculation of the YBCO vibrational modes, see Ch. 3.

In normal superconductors, the strongest evidence of the phonon nature of the electron-electron coupling are the tunnelling measurements and the isotopic substitutions.

The tunneling measurements in cuprate are, unfortunately, very hard to be performed and the isotopic substitution gave unusual results, hard to be understood.

There is not any direct evidence of the involvement of phonons in the pairs creation.

The more interesting modes for this analysis are the so-called "soft modes", i.e. those modes which are not stable when the temperature or the doping level are varied. These modes do exist, actually, at the tetragonal-orthorombic transition doping level, but in that zone of the phase diagram the superconductivity is almost absent, so that the soft modes seems to be not involved in the condensation. There are, moreover, some anomalous features of the phonon spectrum which suggest some kind of more complex attractive mechanism: in the BCS theory the frequency of the under-gap phonons is red-shifted by the condensation and the over-gap modes are blue-shifted by some percentage point. In cuprates, all infrared phonons are red-shifted, being them above or below any known gap value.

On the other hand, before the HTCS discovery, the highest predicted critical temperature was about 30K. A strong electron-phonon interaction should produce a strong instability of the lattice itself, and this happens for very much lower values of the exchange forces compared to those required to have a phonon-coupled electron pair in cuprates [14]. Moreover, it is not possible, despite all efforts, to explain the peak of T_c in the phase diagram as a function of doping in terms of a phonon interaction, and that peak is doubtless the main feature of these compounds.

Within the hypothesis that the anelastic scattering of electrons is not ruled by phonons, it can be ruled by some other kind of excitation, and it is likely that such excitation has an electronic nature.

Actually, the matrix element $V(k_1, k_2, q)$, which gives the electron scattering probability from a k_1 momentum to $k_1 + q$ and, simultaneously, from k_2 to $k_2 + q$ is given by

$$V(q, \omega) = \frac{e^2}{4q^2 \varepsilon_0 \varepsilon_r(q, \omega)},$$

where $\omega = (\varepsilon(K_1 + q) - \varepsilon(k_1))/\hbar$. The relative dielectric constant $\varepsilon_r(q, \omega)$ $\varepsilon_r(q, \omega)$ includes all the vibrational modes of the electric polarization, not only the phonon ones. Interband transitions or electron-hole transitions could be, for instance, good candidates.

Since the energy-gap in cuprates is about 250 cm^{-1}, one has, first of all, to investigate the range where $\varepsilon_r(q, \omega)$ is dominated by the low-frequency modes. But for $q = 0$ phonons are the only modes, together with the plasma resonance. This resonance gives a positive sign, and thus a repulsive mechanism, to ε_r, in the frequency range below the plasma frequency (i.e. below 8000 cm^{-1} for (a, b) plane carriers). We have to keep in mind, however, that each low-frequency mode will contribute to the final form of ε_r and so the phonons will add their contribute too, since their energy is comparable with $k_B T_c$. It is possible that all contributes are equally important, and that a single dominant factor could not be found.

Finally, the antiferromagnet nature of cuprates for certain doping values, and the magnetic fluctuations which vanish only for doping values well above the optimal doping, place the magnetic excitations (as, for instance, the spin interactions) among the most relevant candidates.

2.7 Recent developments.

One of the most complete and recent work in the wide literature on HTCS was written by Orenstein and Millis in 2000 [16]. The authors underline that the Anderson hypothesis seems to be right. Shortly afterwards the discovery of Bednorz and Muller, Anderson predicted that the nearness of a Mott insulator phase with the bidimensional features of cuprates would bring to a real new behaviour, which cannot be understood in the old framework of the physics of metals.

From the beginning, it was recognized that the spin plays a non-trivial role in the problem: in a Mott insulator, the highest energy band has one electron for each unit-cell, and the quantum spin-number is, thus, indeterminate. This is not affected by doping, since it creates extra-sites, allowing the charge motion without the need to pay a large energetic cost, due to the Coulomb interactions. In a fermion bidimensional system, the spins of neighbour sites are in a anti-parallel alignment, in order to minimize the energy of the system [17]. They are "coupled" into a sort of singlet state, two by two, forming a so-called "spin liquid". The motion of singlets is similar to the motion of the electrons of a resonant bound of the $\pi-$benzene ring. For this reason, they are called RVB (Resonating Valence Bond). This theory was soon refuted by some experimental evidence which clearly showed that the spin liquid does not exist. Nevertheless, this simple idea takes the essence of some kind of features which will be exposed in the following, and, up till now, the doping range which goes from the disappearance of the antiferromagnet-phase to the superconductive one is considered as the most interesting. Neutronic scattering experiments on high quality single crystal samples, showed a very unhomogeneous distribution of charge and spin.

In these experiments, the Bragg peaks are in correspondence of the lattice vectors $Q = \left(\pm\frac{\pi}{a}, \pm\frac{\pi}{a}\right)$. Note that these vectors, the so-called "nesting vectors", are the normals to the flat and parallel regions of the nested Fermi surface.

As the doping increases, every Bragg peak is divided into four peaks, each with a distance from Q equal to the doping value x (in units $2\pi/a$). This effect can be explained with a stationary or slow varying spin-density wave (SDW), whose phase is $\pi-$shifted in correspondence of a periodic sequence of linear domains. Further measurements on Nb-doped LASCO samples showed [18] that the spin has this behaviour, while the vacant sites, induced by the doping, are placed just on the phase-change lines, forming a sort of "charged stripes". These stripes are separated by a distance equal to $a/2x$ while the SDW wavelength is a/x. Also these stripes give a contribution to the neutron scattering which was experimentally proved [19]. It is not clear at all what kind of implications such an unusual charge distribution can have in the superconductivity.

The $d-$wave-like nature of the order parameter is, nowadays, no more a matter of discussion: the gap has a $d_{x^2-y^2}$ symmetry, with its maxima along the bond directions and its minima (nodes) at 45° with respect to them. This means that, in the linear combination of the order parameter ψ on the base vectors, the elements with a nodal wave-vector have to vanish. As a proof of this, it was noted that the nodal particles dominate the thermal behaviour of cuprates. The biggest effort is

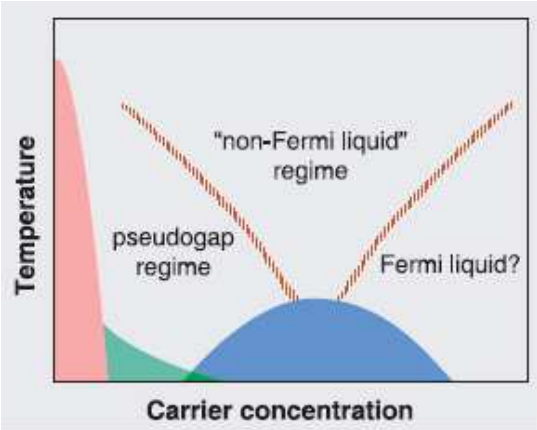

Figure 2.10: YBCO phase-diagram [16].

now dedicated to the estimate of the lifetimes of the quasi-particles, which can give valid informations on the BCS or not-BCS nature of the order parameter.

Since a $d-$wave symmetry requires only four nodal point on the Fermi surface, the volume of the phase-space available for the scattering is quite small. A BCS-like theory predicts that the lifetime of the nodal quasi-particles at low temperature diverges as $1/T^3$ [20].

Absorption measurements in the microwaves range confirm this behaviour, while ARPES data show a $1/T$ behaviour below T_c. If this result will be confirmed by independent measurements, it could be explained by means of the strong quantum fluctuations created by a quantum critical point in the cuprates phase diagram.

However, in this work we will not face the wide field of the "Quantum Criticality" applied to HTCS (see ref [21]).

Recent ARPES measurements [22] showed, with even more clarity, another important feature of the phase diagram, shown in Fig 2.10: the pseudo-gap regime. In Fig 2.11 the ARPES spectrum in the low-doping zone above and below T_c is shown. It is easy to see that the quasi-particle peak, which is clearly seen for $T < T_c$, disappears, while the gap behaviour (i.e. the removal of the carrier density from the region near E_F) remains well above T_c, and reaches, in some case, very high temperatures too (300K).

This behaviour allows to hope that, in the future, critical temperatures higher than the present will be achieved.

A possible explanation of this phenomenon can be found in the peculiar spin structure present in the doping regions near the antiferromagnet-phase, where the material has, a little longer, the "memory" of the previous Mott insulator phase. The antiferromagnetic arrangement can take place because of the presence of one electron for each unit-cell: when each electron see an opposite spin in every neighbour site, it can move into another site for an infinitesimal time, increasing its dislocation and decreasing its potential energy. When an hole is inserted into an antiferromagnetically oriented spin-lattice, it is clear that it cannot move itself with-

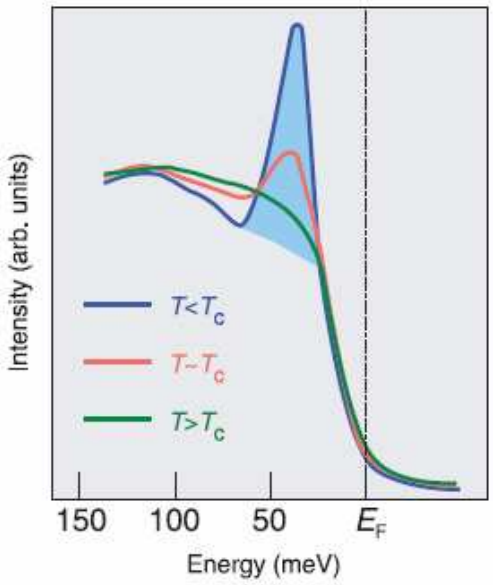

Figure 2.11: ARPES spectra of YBCO above and below Tc [16].

out greatly increasing the Coulomb interaction with its neighbours. This opens two possibilities: two holes move together so that they compensate each other (this hypothesis is quite similar to the Anderson's RVB singlets) or the holes are placed into equally spaced linear domains, or "charge stripes".

Thus, it seems that the cessation of the superconductivity has not to be related to the pairs breaking, as happens in BCS superconductors, rather than the loss of long-range phase correlations. In other words, in the BCS theory the main energy scale is given by the gap Δ, while in cuprates what is more important is the "phase stiffness" ρ_s, i.e. the zero-temperature superfluid density. In this scenario, when the temperature rises above the critical value, the Cooper's pairs do exist, but they cannot superconduct since they lost their coherence. For this reason, the superconductive gap in cuprates is now called, by many researchers, "coherence gap".

Nevertheless, the transport properties in the CuO_2 planes do not show any sign of the presence of a gap. This experimental evidence lead many researchers to invoke a separation between charge and spin. The latter would be coupled into electrically neutral singlets, so that the plane transport properties should not be affected by them. On the contrary, the $c-$axis conduction shows the presence of a gap as it requires an hopping of an electron from a plane to another, and, thus, it requires a spin pair breaking. Nevertheless, the question "if and when" charge and spin could be separated into a bidimensional system is far from being solved, also if it is well-known in the case of monodimensional systems [23].

Besides the large theoretical efforts [24], the pseudo-gap phenomenon and the quasi-particles lifetimes were studied in great detail from an experimental point of

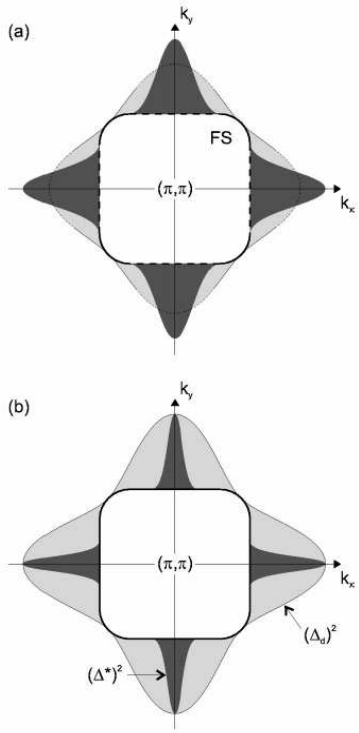

Figure 2.12: Pseudogap (dark gray) and coherence-gap (pale gray) behaviour in underdoped (a) and optimally doped (b) samples [26].

view too.

Apart from the photoemission techniques described before, there is, of course, the Raman Spectroscopy [25], [26]. With the help of this technique, it was, in particular, possible to follow the pseudo-gap behaviour with respect to the coherence gap, varying several parameters, and it was found that these are two uncoupled quantities: the pseudo-gap is likely to be a "spectral deficit" between 0 and 800 cm^{-1}, which corresponds to an energy E^*. This energy does not depend on doping or temperature (until the "critical temperature" T^*), while it is confirmed that the coherence gap has a $d_{x^2-y^2}$ symmetry and it scales with T_c. In Fig 2.12, the pseudo-gap (dark gray) and the coherence gap (pale gray) behaviour in the phase-space is shown for underdoped samples (a) and optimal doped samples (b).

In the last case, the pseudo-gap is confined around the principal axes, while the coherence gap is well defined over the whole Fermi surface. In the first case, the pseudo-gap covers a wide area of the phase-space. The Fermi surface is present only in the nodal directions, and, in these directions, the superconductive gap scales as T_c.

More refined optical techniques were made (see refs [27], [28], [29]) in order to investigate the anti-nodal particles lifetime. These lifetimes are harder to be investigated since they require an extremely k-sensitive experiment, in order to distinguish

them from the nodal ones. These experiments, however, are still controversial.

At the moment, it seems clear that the quasi-particles lifetime problem (joined with the understanding of the "normal" state, which, up till now, escapes from a clear description) is crucial in order to understand these exotic and elusive materials. More measurements in this direction can tell us if we can maintain a quasi-particle picture (even if modified) or if it is necessary to completely change our mind, as proposed by some more "brave" theories.

Chapter 3

Spatial Groups and YBCO vibrational modes.

In this Chapter, we will give the brief description of the Spatial Groups Theory, which is the basic tool in the study of the crystal symmetries, and we will calculate the number of YBCO vibrational modes in the framework of this theory. In refs [30] and [36] is possible to find an accurate treatment of the subjects discussed here. To have a brief overview of the main concepts used in this Chapter, see App. A.

3.1 Spatial Groups.

A point-group structure completely defines the symmetry of the equilibrium configuration of any molecule. In order to study the symmetry of crystals, we should introduce some new operations, which will define the so-called "Spatial Group".

3.1.1 Crystal classes.

Identity E, rotations C_n, reflection σ, inversion i and improper rotation S_n operations are still valid symmetries in a crystal, below the condition that C_n and S_n can have only certain values of their parameter, i.e. rotations are allowed only for certain angles $\phi = 2\pi/n$. It is possible to prove that the only admitted angles are given by

$$n = 1, 2, 3, 4, 6. \tag{3.1}$$

This lead to the fact that we have only 32 point groups which can give the symmetry of a crystal. These 32 groups are called "Crystal Classes". All possible point groups, relative to different kind of crystals, are listed into every text-book.

As in the case of molecules, the generic symmetry operation on the vector $\vec{x}$ is

$$\vec{x}' = \mathbf{R}\,\vec{x},$$

where

$$\mathbf{R} = \begin{pmatrix} \cos\phi & -\sin\phi & \\ \sin\phi & \cos\phi & \\ & & \pm 1 \end{pmatrix}$$

is the proper (+1) or improper (−1) rotation matrix, and the angle $\phi = 2\pi/n$ has to satisfy Eq. 3.1.

This matrix leaves the rotation-point unmoved. Thus, the translation symmetry of infinite crystals has to be obtained by a generalization of the rotation matrix:

$$\vec{x}' = \mathbf{R}\,\vec{x} + \tau,$$

i.e.

$$\vec{x}' = \{\mathbf{R}|\tau\}\ \vec{x}\,.$$

which is the so-called Seitz notation.

The properties of $\{\mathbf{R}|\tau\}$ are:

1. the product $\{\mathbf{R}'|\tau'\}\{\mathbf{R}|\tau\} = \{\mathbf{R}'\mathbf{R}|\mathbf{R}'\tau + \tau'\}$ is associative.
2. The inverse element is given by $\{\mathbf{R}|\tau\}^{-1} = \left\{\mathbf{R}^{-1}|-\mathbf{R}^{-1}\tau\right\}$.
3. The identity is $\{\mathbf{E}|0\}$.
4. The operator $\{\mathbf{R}'\mathbf{R}|\mathbf{R}'\tau + \tau'\}$ is still a $\{\mathbf{R}|\tau\}$-like operator.

The $\{\mathbf{R}|\tau\}$-operations are, thus, a group. Moreover, the pure translations $\{\mathbf{E}|\tau\}$ are a subgroup.

Limiting to the primitive (or elementary) pure translations given by

$$\tau_n = n_1\mathbf{t}_1 + n_2\mathbf{t}_2 + n_3\mathbf{t}_3,$$

where $n_{1,2,3} \in \mathcal{Z}$ and $\tau_{1,2,3}$ are three independent lattice vectors, the group $\mathcal{G} \equiv \{\mathbf{R}|\tau\}$ is called the Space Group of the crystal, while the abelian subgroup $\mathcal{I} \equiv \{\mathbf{E}|\tau_n\}$ is called Translation Group.

Groups $\mathcal{G}$ and $\mathcal{I}$ are, of course, infinite groups. Nevertheless, keeping in mind the crystal periodicity conditions

$$(n_i + N_i)\,\mathbf{t}_i = n_i\mathbf{t}_i$$

where N_i is an arbitrary number of primitive cells in the $\mathbf{t}_i$-th direction, the group $\mathcal{I}$ has dimension $N_1N_2N_3$, which is the total number of primitive cells in the cycle-unit made by $N_1 \times N_2 \times N_3$ primitive units. The crystal can be regarded as the infinite reproduction of this cycle-unit cell.

Finally, we can define the Factor Group $\mathcal{U}$, i.e. the group of the unit-cell, as

$$\mathcal{U}: \quad \mathcal{G} = \mathcal{U} \otimes \mathcal{I}\,.$$

The irreducible representations of $\mathcal{U}$ include all irreducible representations of $\mathcal{G}$ which are invariant under a primitive translation. Since the primitive translation lattice of the space group is invariant under the operation of its factor group, the number of operations of the translation group will be limited too. These 14 different kinds of lattices are called "Bravais lattices". A number of space groups can be associated with each Bravais lattice, so that the total number of the possible space groups is 230 [30].

Let us now make a simple but important consideration: writing the generic translation τ as the sum of a primitive (τ_n) and a not-primitive translation ($v(\mathbf{R})$), we have

$$\{\mathbf{R}|\tau\} = \{\mathbf{R}|v(\mathbf{R}) + \tau_n\} = \{\mathbf{E}|\tau_n\}\{\mathbf{R}|v(\mathbf{R})\}\,.$$

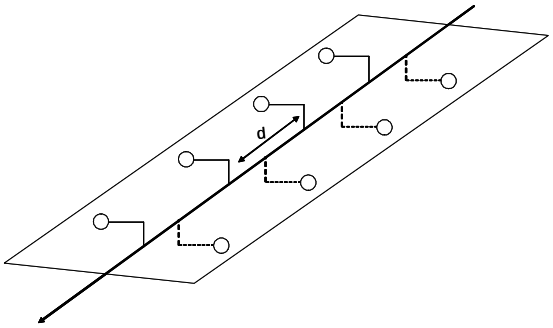

Figure 3.1: Screw-axes 2_1.

In 73 of the 230 space groups it happens that $v(\mathbf{R}) = 0$ and, thus, an unique association between each operation $\mathbf{R}$ of the point group and the operation $\{\mathbf{R}|0\}$ of the space group exists, so that the point group is a subgroup of $\mathcal{G}$. These are the so-called "symmorphic" groups. The non-symmorphic groups usually contains the symmetry elements called "screw-axes" and "glide-planes".

3.1.2 Screw-axes and glide-planes.

Because of the translation symmetry, there are two more symmetry operations, whose corresponding symmetry elements are called screw-axes (roto-translations) and glide-planes (reflection-translations).

The screw-axis is a clockwise rotation by an angle of $\phi = 2\pi/n$ with $n = 1, 2, 3, 4, 6$, followed by a non-primitive translation into the same direction of the rotation-axis. The international symbol is n_p where $p = 1, 2, 3, ...(n-1)$ and p/n is the fraction of the primitive translation made during the symmetry operation.

A glide-plane is a reflection on a plane, followed by a non-primitive translation along a in-plane-lying direction. It is represented by the symbols a, b, c (axial planes $\vec{a}, \vec{b}, \vec{c}$), n (diagonal planes $\left(\vec{a} + \vec{b}\right)/2$ and $\left(\vec{a} + \vec{b} + \vec{c}\right)/2$) and d ("diamond planes" $\left(\vec{a} + \vec{b}\right)/4$ and $\left(\vec{a} + \vec{b} + \vec{c}\right)/4$), depending on the crystal symmetry. In Fig 3.1 and 3.2 a schematic picture of these two operations is shown.

3.1.3 The symmetry of the lattice sites.

Let us consider a generic point of the lattice. A group operation can move that point or not. The point which can be generated from a given one are called "symmetrically equivalent" and their number is the "multiplicity" of the starting point. A site of the crystal can be, thus, characterized by the point group which leaves it unmoved, which is, in turn, a subgroup of the factor group. The site group is, thus, the group which characterizes the symmetries of the electromagnetic crystal field which surrounds that site. This can be very useful, for instance, in the case of a molecule which occupies a certain reticular site: even if the free molecule has its own point group, its symmetry will be lowered by the crystal in order to let it assumes the

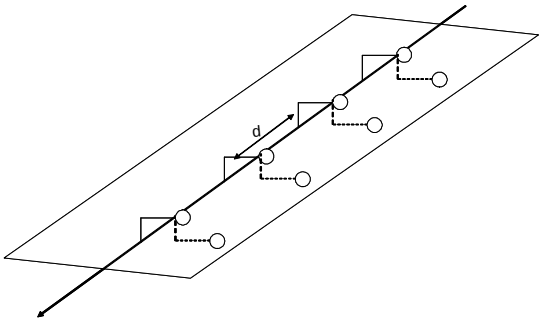

Figure 3.2: Glide-plane b.

symmetry of the site where it is. In this case the site group must be a subgroup of the free molecule point group.

3.1.4 The Translation group.

Let us consider, for simplicity, a symmorphic group, with a translation group $\{\mathbf{E}|t_n\} \equiv \mathcal{I}$. The cycle-bound conditions are

$$\{\mathbf{E}|t_1\}^{N_1} = \{\mathbf{E}|t_2\}^{N_2} = \{\mathbf{E}|t_3\}^{N_3} = \{\mathbf{E}|0\}\,.$$

Since the vector sum is commutative, the translation group will be commutative, and, thus, abelian. In such a group, each element is a class by itself, the number of irreducible representations (each of one dimension) is equal to the order of the group and, for each representation, it is possible to prove that:

$$\chi^{(k)}_{\tau_n} = \exp[2\pi i \vec{k} \cdot \vec{\tau}_n],$$

where

$$\vec{k} = \frac{s_1}{N_1}\vec{b}_1 + \frac{s_2}{N_2}\vec{b}_2 + \frac{s_3}{N_3}\vec{b}_3.$$

Here $\vec{b}$ is a reciprocal lattice vector and $s_i = 1, ..., (N_i - 1)$.

Let us consider a finite crystal, made by $N_1 \times N_2 \times N_3$ unit-cells, having m atoms for each cell. It is clear that the total number of vibrational modes will be $3mN_1N_2N_3$. It is also clear that the unique translation which leaves a given point unmoved is the identity element. This implies that the characters of the reducible representation of the site translations will vanish for each not-identical operation, while the character of the identity E is

$$\sum_{i=1}^{3mN_1N_2N_3} 1 = 3mN_1N_2N_3,$$

which is the order of E. It is possible to expand these characters on the irreducible representations of the group, and find that every representation contains $3m$ vibrational modes. The acoustic modes, in particular, are pure translation modes, and they all belong to the total-symmetric representation.

It can be also shown that the dipole moment as well as the polarizability (i.e. the infrared and Raman activities, respectively) belong to the total-symmetric representation of the translation group too. This means that they are all[1] $\vec{k} = 0$ transitions, i.e. in the Γ-point of the Brillouin zone (BZ).

3.1.5 The Factor group.

The factor group has, in general, the crystal base informations besides the kind of its lattice. The symmetries of the lattice (without base) and of the crystal (lattice and base) coincide, of course, only for monoatomic compounds.

The vibrational modes are calculated by means of the Winston and Halford method, which is very similar to the molecule method. It is possible to prove that the "magic formula" (see App. A) for the space group irreducible representation expansion is equivalent to the one of the only factor group (i.e. it is possible to draw out the contribution of the translation group), and, thus, the crystal vibrations will be classified according to the factor group irreducible representations. It is as if the unit-cell could be considered as a stand-alone molecule.

In order to find the characters of the reducible representation which have to be expanded, one has to count how many atoms go in themselves for each operation. Then, one has to sum the number of atoms which go into the same position, but into another unit-cell.

In this way, the translation symmetry is automatically satisfied, and the molecule method works "as if" the translation symmetry does not exist. Moreover, one has to weigh the contribution of each atom with the inverse of the number of unit-cells which contain the atom, as usually done in the physics of crystals. Finally, the last important difference between the molecule and the crystal method is to not subtract the translation and rotational characters from the displacement reducible representation characters.

In facts, the translational characters give the three acoustic phonon branch (i.e. the vibrations which move the crystal center of mass), and the rotational characters do not exist, since crystal atoms are fixed in the space, and they have not any rotational degree of freedom.

3.1.6 The parity of states: gerade and ungerade.

It is possible to prove, as mentioned before, that, into a given symmetry group, if ϕ_a, ϕ_b are the base-functions for the irreproducible representations Γ_a, Γ_b of the group, the integral

$$\int_S \phi_a \cdot \phi_b d\tau,$$

defined over the whole space S, vanish if the decomposition of the direct product $\Gamma_a \otimes \Gamma_b$ does not contain the total-symmetric representation. The reason is that the integral of the odd part of the integrating function vanishes for symmetry when integrated on the whole space, while the even part vanishes if the direct product

[1] The $\vec{k} \neq 0$ vibrational modes treatment is more complicate and it will not be faced here.

$\Gamma_a \otimes \Gamma_b$ does not contain the total-symmetric representation. For instance, in the perturbative calculation of the matrix element $(\phi_i, \mathcal{H}'\psi_k)$, the transition will be permitted (i.e. the matrix element is not vanishing) if this element acts as a scalar number (i.e. in according to the total-symmetric representation) under the operation of the symmetry group. This is equivalent to say that, being Γ_j the symmetry of the interaction Hamiltonian $\mathcal{H}'$, the total-symmetric representation is present in the direct product $\Gamma_i \otimes \Gamma_j \otimes \Gamma_k$, i.e. the base-function ϕ_i is not orthogonal to all the base-functions which are present in the function $\mathcal{H}'\psi_k$. Thus, in order to calculate the selection rules of a given problem, all things we need are the irreducible representations of the initial and final state as well as the interaction Hamiltonian one. With this tools, one can calculate the triple direct product $\Gamma_i \otimes \Gamma_j \otimes \Gamma_k$, expand it on the irreducible representations of the group and look if the total-symmetric representation is present or not.

Since the infrared (IR) interaction Hamiltonian has the usual dipole moment form, it must have the same parity of $\vec{r}$, i.e. it is odd. On the contrary, the Raman interaction Hamiltonian must have the parity of $\vec{r} \cdot \vec{r}$, since it is composed by an absorption to a virtual level and a simultaneous emission to a real level (see Ch. 1.3 and App. A), and so, it will be even. The IR and Raman transitions couple two states with different (IR) or equal (Raman) parity, and the base functions will be x, y, z for IR-transitions and x^2, y^2, z^2, xy, xz, yz for Raman-transitions (see App. A).

Moreover, it can be proved that the ground-state always changes in according to the total-symmetric representation. These considerations leads to the result that the even levels will be IR-active, and the odd levels will be Raman-active, if the discussion is limited to the ground-to-excited levels transitions.

For those molecules, or crystals, which have an inversion center, each irreducible representation can be only even (symbol g, from German "gerade") or odd (u, "ungerade") under the inversion operation.

As a consequence, an explicit calculation of the selection rules is no longer required, when the vibrational modes are singled out: the transitions between the ground-state and an excited vibrational level will be IR-active if this level has the u symmetry or Raman-active if this level has the g symmetry. Thus, IR- and Raman-spectra are complementary: the same vibration cannot be present in both. On the contrary, if there is not any inversion center, the generic vibration can be both IR- and Raman-active, and the selection rules have to be calculated separately for each level. In any case, IR and Raman spectra are not equivalent, and a complete study of the vibrational modes of a system requires to have both of them.

What said until now is strictly true for perfectly depolarized light. In other words, the parity conservation allows to calculate all the possible IR- and Raman-transitions. If the light has a well-defined polarization, not all modes will be excited. In order to understand what vibrations will be excited, one has to give a look at the tables of characters, and find the irreducible representation which is in correspondence with that oscillation direction.

A generic polarization direction, different from any principal axes, will be expressed as a linear combination of them. When the symmetry of the incident light is found, one can proceed to the calculation of the selection rules, as previously

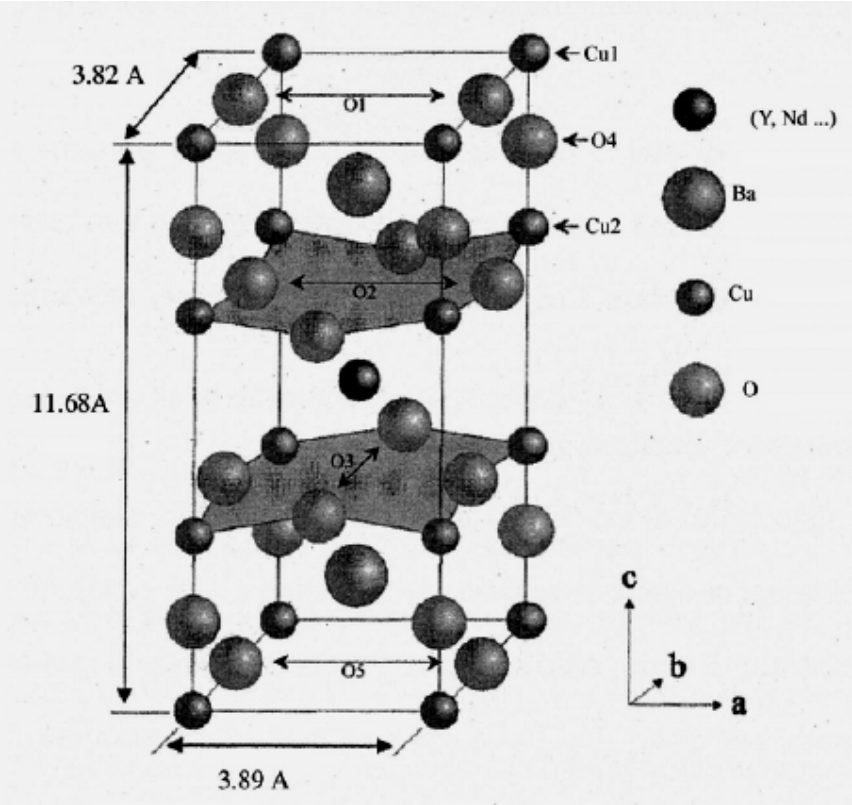

Figure 3.3: The YBCO unit cell.

exposed.

3.2 YBCO vibrational modes.

Let us here briefly recall what showed in §2.2 about the YBCO structure. YBCO, whose unit-cell is showed in Fig 3.3, has a perovskite-like structure, with a principal axis c, passing through the yttrium-atom and the two barium-atoms. This is the main symmetry element of the cell, as shown in the following.

There are to $Cu - O_2$ planes, orthogonal to the $c-$axis. They pass between the yttrium and the two barium-atoms (the Cu-atoms of these planes have, for convention, the label 2, the O-atoms have label 2 along x and 3 along y). There is a linear $Cu - O$ chain (label 1), lying in the y direction. Finally, there are some "bridge" oxygens (label 4) between planes and chains. The chains are fully complete only in the optimal doped orthorhombic $YBa_2Cu_3O_7$ while they are absent in the tetragonal parent compound $YBa_2Cu_3O_6$. In this work, we will be focused on the optimal doped material. For an orthorhombic lattice ($a \neq b \neq c,\ \alpha = \beta = \gamma = \pi/2$) the possible symmetry groups are only three: D_2, D_{2h}, C_{2v} [30]. Carefully looking at the unit-cell in Fig 3.3, it is possible to immediately observe a $\pi-$rotational symmetry around the $\vec{z}$ axis, $C_2(z)$: under this transformation, the $Cu1$-atoms go

into the $Cu1$-site opposite to them (i.e. their displacement is the vectorial sum $\vec{a}+\vec{b}$), the $O1$-atoms go into the opposite site, and the $Cu2$-, $O2$-, $O3$- and $O4$-atoms do the same; the yttrium and the two barium-atoms lie on the rotation axis, and thus they are unmoved. In the same way, it is possible to find two other rotational axes (x and y), both passing on the yttrium, but both having lower symmetries ($C_2(y), C_2(x)$): these two rotations leave only Y unmoved and exchange the Ba positions (note that the positions of the two barium atoms is not linked by any integer multiple of a lattice vector). The CuO_2 planes are exchanged too. Also them are not linked by a lattice vector, while chains-atoms are linked by $\vec{c}$. The same holds true for the inversion operator i (whose center of inversion in on the yttrium site), and for the reflection $\sigma(xy)$. Finally, there are two more reflections by the two vertical planes where $\vec{z}$ lies, which are $\sigma(xz)$ and $\sigma(yz)$. They link the atoms of the same plane or chain. Also in this case, as well as for the $C_2(z)$ rotation, all atoms go into equivalent sites. The symmetry group we have to consider will be, thus, D_{2h}, which has order 8. Its characters table is:

D_{2h}	E	$C_2(z)$	$C_2(y)$	$C_2(x)$	i	$\sigma(xy)$	$\sigma(xz)$	$\sigma(yz)$	
A_g	1	1	1	1	1	1	1	1	x^2, y^2, z^2
B_{1g}	1	1	−1	−1	1	1	−1	−1	R_z, xy
B_{2g}	1	−1	1	−1	1	−1	1	−1	R_y, xz
B_{3g}	1	−1	−1	1	1	−1	−1	1	R_x, yz
A_u	1	1	1	1	−1	−1	−1	−1	
B_{1u}	1	1	−1	−1	−1	−1	1	1	z
B_{2u}	1	−1	1	−1	−1	1	−1	1	y
B_{3u}	1	−1	−1	1	−1	1	1	−1	x
Γ_{xyz}	3	−1	−1	−1	−3	1	1	1	

In order to calculate the vibrational modes, we have to write, first of all, the characters of the reducible representation Γ_{tot}, which contains all possible displacements of each atom in every equivalent lattice site. From the previous considerations, it is clear that the number of the unchanged sites is 13 (i.e. all the atoms of the unit-cell) for $C_2(z)$, $\sigma(xz)$, $\sigma(yz)$ and, of course, the identity E. For the other symmetries, we have to be careful and count each atom as a part of more than one unit-cell: for instance $Cu1$ weighs 1/8, $O2$ weighs 1/2 and so on. The number of unchanged site is, thus, 3 for all remaining symmetries. Therefore, the characters χ are:

$$\chi = 13\ 13\ 3\ 3\ 3\ 3\ 13\ 13.$$

Since the character of the direct product of two representations is the algebraic product of their characters, the Γ_{tot} characters will be given by the product between χ and the $\Gamma_{x,y,z}$ characters:

$$\Gamma_{tot} = 39\ -13\ -3\ -3\ -9\ 3\ 13\ 13.$$

Now, we have to decompose Γ_{tot} on the irreducible representations of D_{2h}:

$$\Gamma_{tot} = 5A_g + 5B_{2g} + 5B_{3g} + 8B_{1u} + 8B_{2u} + 8B_{3u}.$$

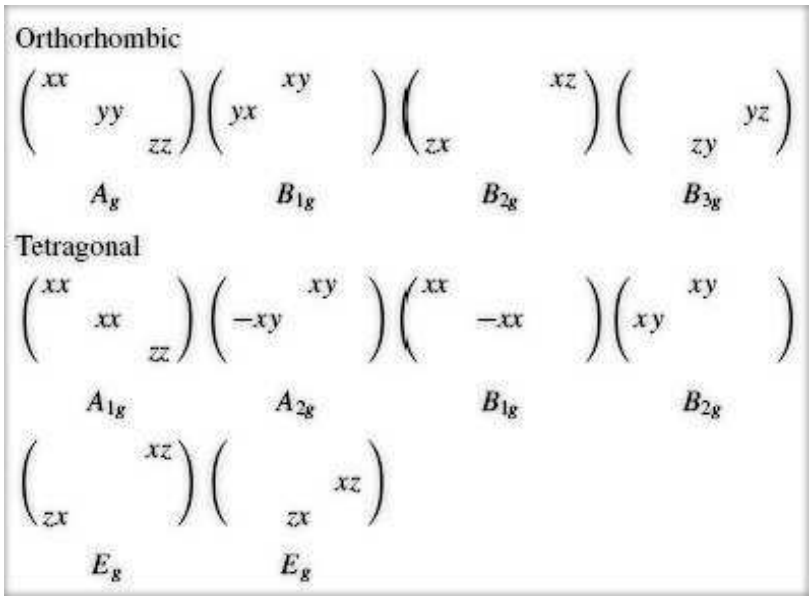

Figure 3.4: Irriducible representations of the Raman tensor [94].

Looking at the characters table, we can assign the three acoustic modes to the three B_u modes, since they correspond to the base functions x,y,z. It remains 7×3 "ungerade" optical modes (IR-active) and 5×3 "gerade" optical modes (Raman-active). Thus, we have 36 optical modes, as mentioned in §2.6.

The same calculation, in the case of the parent compound $YBa_2Cu_3O_6$ (D_{4h} group, tetragonal lattice $a = b \neq c,\ \alpha = \beta = \gamma = \pi/2$), leads to:

$$\tilde{\Gamma}_{tot} = 4A_{1g} + B_{1g} + 5E_g + 6A_{2u} + 8B_{1u} + B_{2u} + 7E_u.$$

Here we have two E_u (x, y) acoustic phonons and one A_{2u} (z) acoustic phonon, 11 IR-active and 10 Raman-active phonons.

From these simple calculations, is possible to see how the appearance of the copper-oxygen chains, changes significantly the lattice structure of the material (by changing the values of a and b axes) and, thus, its vibrational modes.

In Fig 3.4, it is possible to directly have the polarizations of each Raman-active symmetry in both cases: for instance, in the D_{2h} group, the A_g modes will be excited only if the incident light and the scattered light have parallel polarizations, while B_g and E_g modes are excited into a cross-polarizations geometry. For a detailed treatment of the polarized Raman scattering, see ref [36]. From an experimental point of view, these selection rules are of use to give to each phonon line its own symmetry. This information, joined with the isotopic substitution data, is a focal point in order to understand what atoms are involved in a given vibration.

For instance, in the optimal doped YBCO, only 5 Raman phonons are actually seen in normal Raman experiment instead of 15, and they are all $c-$polarized modes. Their frequencies are: 115, 150, 330, 430, 500 cm^{-1}. The (a, b) planar modes are

too weak to be easily seen. This five modes were assigned as follows [31]: the lower frequency one is mainly due to the barium vibrations, since it is the largest atom of the cell; the second to the plane-copper vibrations; the third and the fourth to the plane-oxygens and the last to the chain-oxygens, which are the most mobile atoms of the cell. All belong to the total-symmetric representation A_g, but the 330 cm^{-1} mode have a peculiarity: it belongs to A_g in the orthorhombic phase, but in the tetragonal phase it belongs to B_{1g}. Since the orthorhombic distortion of the crystal axes is very small, this vibration follows approximately the B_{1g} selection rules and can be, thus, located unambiguously from the cross-polarization spectra.

In Fig 3.5, all IR- and Raman-optical modes are shown. Each mode have three frequencies values: the theoretical value (calculated using the method described in ref [31]), one measured by IR- and Raman-spectra, and one by neutron scattering experiments.

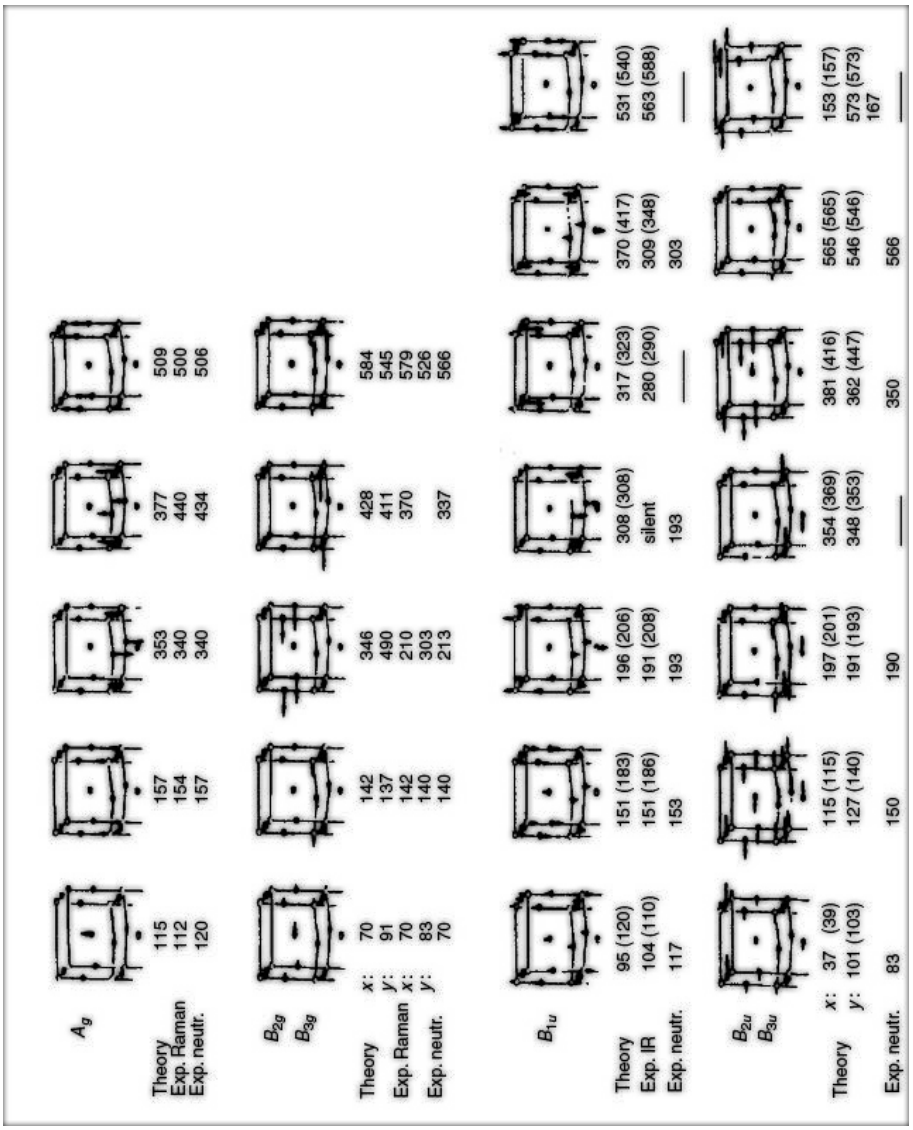

Figure 3.5: Summary scheme of the YBCO normal modes [94].

Chapter 4

The CRS experimental setup and its optimization.

As previously said, the Four Wave Mixing is given by three interacting waves into a nonlinear medium, in order to give a fourth wave. This phenomenon was treated in Ch. 1.5, assuming a plane-wave expression for all fields involved in the process. The plane-waves are abstract quantities, which are present in every point of the space at each time. The real experimental light is, on the contrary, composed of Gaussian pulses, with a certain direction and a finite duration, which is, in our case, about 20 ps.

Nevertheless, this does not change the theoretical approach given before, since the TEM_{00} Gaussian beams have a flat wave-front in their focus, and they are, thus, well-approximated by a plane-wave. Moreover, the interaction area on the sample is very much larger than the unit-cell dimension and the pulse duration is very much longer than the electromagnetic oscillation period.

We should note that our reflection geometry allows to study thin films samples, without the need to take into account the substrate contribution to the FWM signal, since the penetration length at these frequencies is usually lower than the film thickness.

There are two main experimental issues to be faced when pulsed beams are used: the spatial superposition of the beams, and their temporal synchronization. In the following, a detailed description of the experimental setup will be given and the optimizing procedures will be shown.

4.1 Setup description.

The experimental setup in Fig 4.1 is made by three light-lines, called Pump, Probe and Tune, and a revelation-line.

The Pump and the Tune are synchronized during all kind of measurements. The dynamic grating described in Ch. 1.6 is created by these two beams, while the Probe (which has always the same frequency of the Pump) has to be diffracted by it, in order to investigate its amplitude as a function of the Tune frequency (to measure the CRS spectrum) or the Probe delay (to measure the quasi-particles lifetime).

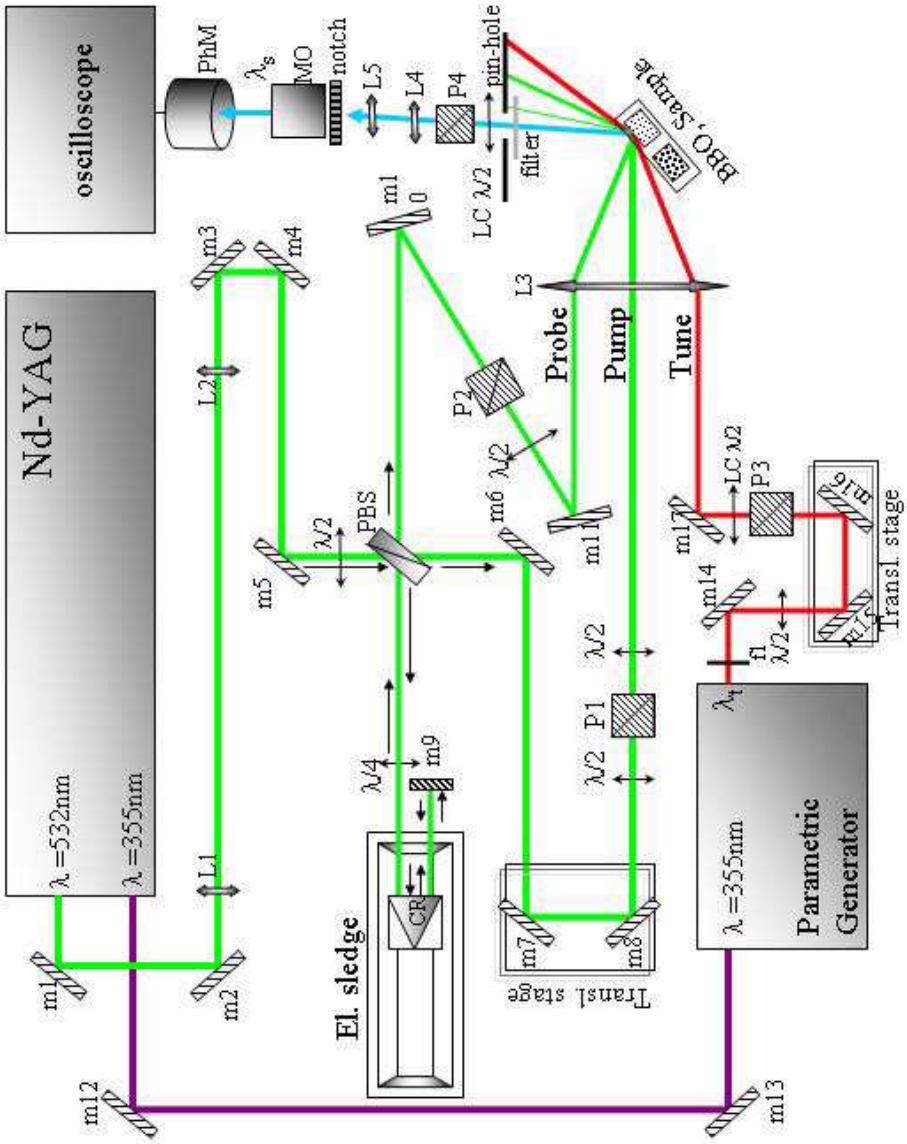

Figure 4.1: Experimental setup for the Coherent Raman Spectroscopy in a "reflection" geometry.

The light-source we used is a $Nd^{3+} - YAG$ mode-locked laser (mod. PL214, Ekspla Ltd) and its second and third harmonics. Its repetition rate is 10 Hz, it has three light-outputs, whose highest pulse energy is 80 mJ ($\pm 2.5\%$) at 1064 nm (fundamental, IR), 20 mJ ($\pm 5\%$) at 532 nm (II harm., Vis), 10 mJ ($\pm 7.5\%$) at 355 nm (III harm., UV). The 532 nm-output goes into a long-focal telescope (lenses $L1$ and $L2$, with 1 m and 0.5 m focal length, respectively), in order to keep the beam waist constant during all its path. The beam is then divided in two by a beam splitter polarizer (PBS): these two beams are the Pump (the stronger) and the Probe (the weaker). An half wavelength wave-plate is before the PBS, in order to control the percentage of light intensity to be sent in the Pump or in the Probe beams. The UV-output goes through mirrors $m12$ and $m13$ into an optical parametric generator (OPG). The OPG generates tunable light pulses, whose frequency is in the range $410 \div 680$ nm, in our case. Its spectral width is about 6 cm^{-1}.

In Fig 4.1, some other components, as control photodiodes and pin-holes, are not shown for clarity. Let us now discuss the four lines one by one.

Pump-line:

The Pump beam (green thick line in figure) goes through the mirror $m6$ into a delay line made by mirrors $m7$ and $m8$, mounted on a translation stage, whose extension is about 3 mm. This line is used in the synchronization procedure only. The beam goes, then, through a line made by a $\lambda/2$ wave-plate and the polarizer $P1$. This line can control the Pump intensity. The last wave-plate is used to change the Pump polarization.

Probe-line:

The Probe beam (green thin line in figure) goes into the corner reflector (CR), placed on a electric sledge, whose length is about 30 cm. The sledge is moved by a personal computer, with an position error of about 0.5 μs, which corresponds to about 1.7 fs delay[1]. The corner reflector is an useful tool to be mounted on mobile supports, since it gives back the light into the same direction from which it comes, in order to preserve the alignment of the beam and, thus, the superposition on the sample surface. The mirror $m9$ sends back again the beam into the CR so that the $\lambda/4$ wave-plate acts twice, and allows the beam to pass through the PBS. Finally, some other optics are used, as in the case of the Pump, in order to adjust the Probe direction, intensity and polarization.

Tune-line:

The OPG-output (red line in figure), having a variable wavelength λ_t, is filtered by filter $f1$, in order to remove the UV residual, and goes through the mirror $m14$ into a delay line similar to the Pump one, and made by mirrors $m15$ and $m16$. Also this line has some intensity and polarization control optics.

Revelation-line:

The FWM signal (blue line in figure), comes out from the sample with a different wave-vector and different frequency, with respect to the reflected beams. The revelation line can, thus, separate with great efficiency the signal from the background noise, since it can work both in the space-domain (blocking the other beams with a pin-hole) as well as in the frequency-domain (by filtering the light before the

[1] it is, thus, negligible, with respect to the pulse duration.

detector's head).

The three beams go through the achromatic lens $L3$ to the sample. Actually, it is possible to not use this lens in order to maximize the interaction area. The sample is into a thermal controlled stage, and its temperature can, thus, be varied in the range $-190 \div 600$ °C with 0.1 °C accuracy. In the thermal stage chamber the pressure can be fixed at about 10^{-3} torr. The revelation line has, as usual, a wave-plate polarizer series in order to investigate the polarization of the signal. The signal is, finally, filtered by means of a double-gratings monochromator (MCR, Jobin-Yvon mod. Gemini-180) and sent to a side-on photomultiplier (PMT, Hamamatsu mod. R928, $185 \div 900$ nm). The electric signal is time-integrated by a gated integrator (Stanford, mod. SR250) and the digital output reaches, finally, the personal computer.

4.2 Alignment procedures and optimization techniques.

The main problem to be faced with a setup of this kind, is, of course, the time and spatial superposition of the beams. The procedure we used is based on a nonlinear crystal for the second harmonic generation (SHG): the beta-barium borate, or BBO. Its great nonlinear efficiency, allows to direct measure the SHG-signal as a function of the alignment or of the Probe delay, even starting from an unfavourable position. Moreover, the time-resolved SHG measurement gives another fundamental quantity, which is the time-resolution of the setup, as shown in the following. Finally, the BBO crystal shows a great third order response too: one of its phonon resonance, near 600 cm^{-1}, is so strong to be visible with the naked eye, and, thus, it is an invaluable tool, in order to align the revelation-line.

The fundamental requirement that this system has to satisfy, in order to have reliable measurements, are two: one in the time-domain and one in the frequency-domain.

In the time-domain, the FWM intensity is measured as a function of the CR position on the sledge. It is, thus, needed to verify that the CR movements do not change the beam superposition. This was made by means of the manual point-to-point maximization of the signal along a delay range of 40 ps, and no difference from the automatically moved CR data was found.

In the frequency-domain, the FWM intensity is measured as a function of the Tune frequency. Since the FWM wave-vector depends on the Tune frequency, is not possible to keep it fixed during the measure. The only thing which can be done, is to minimize the revelation-line path. Then, an estimate of the angular dispersion of the FWM signal have to be compared with the angular acceptance of the monochromator. It is further to note that the phase-matching relationship of Eq. 1.23 is valid only inside the material, while, in order to calculate the exact beam direction in the "reflection" geometry, the material surface discontinuity has to be taken into account. Eq. 1.23 is, thus, valid only for the surface-plane-lying components of the involved wave-vectors. The normal component can be after obtained from the energy (i.e. frequency) conservation law. The $y-$axis is the normal to the sample surface, θ is the angle between y and the Pump wave-vector $\vec{k}_1$ (positive in an anti-clockwise direction), α is the angle between the Pump and Probe ($\vec{k}_2$) or

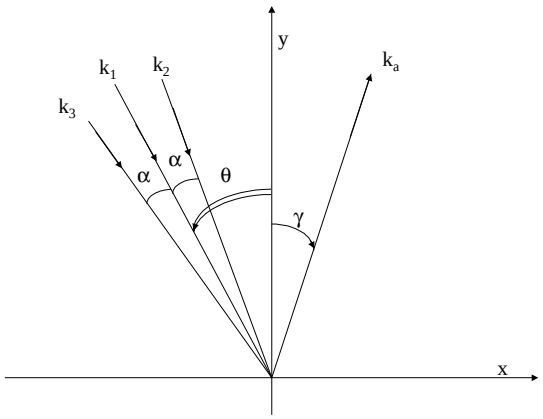

Figure 4.2: FWM angles.

Pump and Tune ($\vec{k_3}$) beams, and γ is the exit angle of the FWM signal (positive in a clockwise direction). The phase-matching and energy conservation laws are, thus:

$$(\overrightarrow{k_a})_x = (\overrightarrow{k_1})_x + (\overrightarrow{k_2})_x - (\overrightarrow{k_3})_x,$$
$$\omega_a = 2\omega - \omega_t,$$

where ω is the Pump-Probe frequency and ω_t the Tune one. If the air refraction index is equal to the unity, the system gives the solution:

$$\gamma = \arcsin\left(\frac{\sin\theta + \sin(\theta-\alpha) - (\lambda/\lambda_t)\sin(\theta+\alpha)}{2-(\lambda/\lambda_t)}\right).$$

For $\alpha \sim 0.05$ rad, $\lambda = 532.1$ nm and $\lambda_t = 410 \div 680$ nm, we have that the exit angle does not depend strongly on the incident angle θ for $\theta \lesssim 1$ rad. Choosing an almost normal geometry ($\theta \sim 0$, $\alpha \sim 0$) we have $\gamma \sim \theta$, and thus independent on λ_t. Moreover, one can remove the lens $L3$ in order to enhance the interaction area on the sample, and, thus, one obtains, as a secondary result, that the incident angles are even smaller, and the exit angle is than almost constant. In the frequency-domain measurements, we preferred also to use the Probe-line as both Pump and Probe beams, in order to maximize their time and space superpositions. In this case, the Pump is self-diffracted by the dynamic grating formed by itself and the Tune. The exit angle calculation in this modified geometry is given in the next Chapter. Actually, all frequency-domain measurements in the present work are taken within this simplified geometry.

4.2.1 Time resolution and spectral corrections.

In the time-domain measurements, the most important factor to be know is, of course, the time-resolution of the setup.

The direct measurement of the pulse durations of the Pump-Probe beams as well as the Tune beam was performed by means of the SHG of the BBO crystal. The estimated Gaussian time-constant from the auto-correlation curve of the two

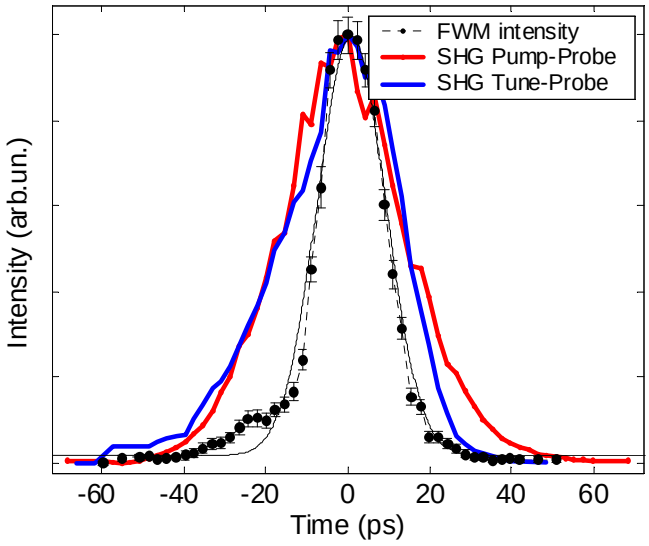

Figure 4.3: Autocorrelation curve of the Pump-Probe beams and correlation curve between Probe and Tune beams compared to the FWM signal intensity of the 640 cm^{-1} line of the BBO crystal.

green beams is $\tau_p = (11 \pm 0.1)$ ps and, thus, their Full Width at Half Maximum ($FWHM_p$) is (26.1 ± 0.2) ps. The estimate of the Tune pulse duration, from the correlation between the Probe and the Tune, using the previously measured value, gives $\tau_t = (9.1 \pm 0.2)$ ps, and, thus, $FWHM_t = (21.4 \pm 0.4)$ ps.

Actually, this is an over-estimate of the setup time-resolution: the FWM process, indeed, shortens the pulse. In Fig 4.3 the FWM signal as a function of the Probe delay is shown, in the case of the 640 cm^{-1} line of the BBO crystal. The FWM signal (black points) is fully under the correlation curves, since the FWM intensity goes as the cube of the field, while the SHG one goes as the square.

The Gaussian fit of this curve, leads to a full width at half maximum that is $FWHM_{fwm} = (19.1 \pm 0.2)$ ps, and, thus, this is the value of our estimated time-resolution.

In the frequency-domain measurements, the frequency step we chose is 1 nm, which is actually larger than the intrinsic laser bandwidth as well as the OPG minimum step (0.1 nm). This choice was done in order to have a reasonable time of measurement (few hours). In order to correct the measurements, the spectral efficiencies of all revelation optics, as well as the monochromator and photomultiplier efficiencies, were taken into account. The main efficiency to be considered, is the OPG generation one: the direct measurement of it by means of a control-photodiode was made. Nevertheless, the shot-by-shot OPG efficiency correction to the spectra was found to greatly enhance the spectral noise, and thus an interpolating curve was used to correct only the slow variation of the Tune energy.

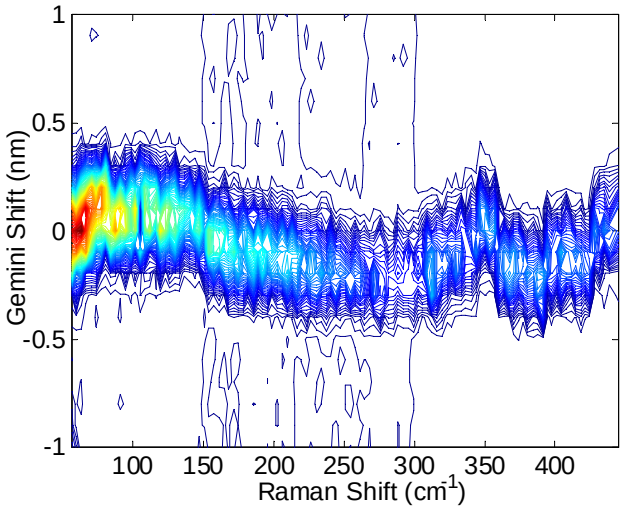

Figure 4.4: Contour plot of a Germanium spectrum. The color scale ranges from white (zero) to blue (low) up to yellow and red (high values). On the y-axis, the MCR (Gemini) displacement, referred to the theoretical expected wavelength.

4.2.2 Spectral synchronization.

Another important factor to be considered in order to maximize the detected FWM signal, is the spectral synchronization between the OPG and the monochromator frequency. The Tune frequency is strictly related to the FWM one, as shown in the first Chapter. If the nominal frequency emitted by the OPG does not correspond to the real one, the signal could be artificially depleted, since the monochromator would be set to the wrong wavelength. In order to study the spectral displacement of the parametric generator, we register several spectra from different samples, scanning with the monochromator each single line of the spectrum. We obtained always the same displacement. In Fig 4.4 the spectrum of germanium is shown, as an example: the FWM intensity is given in a color scale (red→high values, blue-white→low-zero values), as a function of the Raman shift on the $x-$axis, while on the $y-$axis there is the MCR (Gemini) displacement, referred to the theoretical expected frequency. It was found that the OPG spectral displacement is never more than ± 0.5 nm from the expected one.

Even if in principle we can use these measurements to automatically correct the MCR wavelength, the simplest method we used to overcome this difficulty, is to open the monochromator slits and thus to slightly lower the MCR resolution in order to obtain the complete detection the whole signal within ± 0.5 nm.

Chapter 5

Results and discussion.

In the first Chapter we have seen in some detail how the FWM theory works into a nonlinear medium. Nevertheless, in this work, our CRS spectra are collected in a "reflection geometry", as shown in the previous Chapter. This means that the detected beam is not the one generated inside the medium: it goes into the opposite direction, even if there is not any nonlinear interaction in that space region. To our knowledge, there is a shortage of works on this subject, since in the past CRS spectroscopy was mainly employed on gasses or liquids. Moreover, in the previous treatment, we always neglected the absorption, while, in this work, we are interesting in metallic or semiconducting materials, all showing a strong absorption in the visible range. In this Chapter we will develop a simple theory to account for the presence of the "reflected" FWM wave, and we will show our first CRS spectra on solid state and in particular on YBCO.

5.1 "Reflection" FWM.

When the FWM wave is created by a nonlinear interaction inside an ideal infinite material, it exist in every point of the space. But, in a real finite sample, light has to enter from an empty region of the space inside the material, crossing its surface. The generated FWM wave will exist, thus, only in the half space beyond the surface. In the other half space, where vacuum or air is present, the surface will act as a source term into the wave-equation which rules that part of the space. In other words, the boundary conditions on the surface can be satisfied only if a FWM plane-wave is supposed to be outside of the medium, with an opposite wave-vector compared to the usual FWM wave. Let us show the mechanism which rules this effect.

5.1.1 The Fresnel tensor.

Since the input waves of the FWM interaction, inside the material, are linked to the external input waves by reflection and refraction laws, it can be useful to introduce a tensor which can relate directly the electric field components of the incident and transmitted waves. However, when the absorption, although small, is not negligible, some attention has to be paid.

Let us consider an isotropic absorbing semi-infinite medium and a plane wave of frequency ω, forming an angle β with the normal $\hat{z}$ to the sample surface defined by the xy plane. Because of the optical losses, the refracted wave-vector $\vec{k} = \vec{k'} + i\vec{k''}$ is complex, with real and imaginary parts having different directions. From the surface boundary conditions it is clear that the imaginary part, which gives the absorption, have to lie on the z axis, since the input component outside is a real wave-vector. Moreover, they fix the x and y components of k: $k'_x = (\omega/c)\sin\beta$, $k''_x = k'_y = k''_y = 0$. The real and imaginary parts of the normal component $k_z = k'_z + ik''_z$ can be obtained from the combination of the other components with the dispersion law $k^2 = \varepsilon_r\left(\omega^2/c^2\right)$ and the relation $\varepsilon_r = \varepsilon'_r + i\varepsilon''_r$:

$$k'_z = -\frac{\omega}{c}\sqrt{\frac{1}{2}\left(\varepsilon'_r - \sin^2\beta\right) + \frac{1}{2}\sqrt{\left(\varepsilon'_r - \sin^2\beta\right)^2 + \varepsilon''^2_r}}$$
$$k''_z = -\frac{\omega}{c}\sqrt{-\frac{1}{2}\left(\varepsilon'_r - \sin^2\beta\right) + \frac{1}{2}\sqrt{\left(\varepsilon'_r - \sin^2\beta\right)^2 + \varepsilon''^2_r}}$$

which, in the small absorption limit $\varepsilon''_r \ll \varepsilon'_r$, leads to

$$k'_z \simeq -\frac{\omega}{c}\sqrt{\left(\varepsilon'_r - \sin^2\beta\right)} \tag{5.1}$$
$$k''_z \simeq -\frac{\omega}{2c}\frac{\varepsilon''_r}{\sqrt{\left(\varepsilon'_r - \sin^2\beta\right)}}.$$

Because of the transverse waves condition $\vec{E}\cdot\vec{k} = 0$, the electric field inside the material will be a complex field too. In order to obtain the usual reflection and refraction laws, it is useful to introduce the s and p unit-vectors $\hat{e}_s = (0,1,0)$ and $\hat{e}_p = (-k_z/k, 0, k_x/k)$ where $k = \sqrt{\varepsilon_r}\omega/c$. Note that, since ε_r is a complex number, the orthogonality relationships $\hat{e}_s\cdot\hat{e}_p = \hat{e}_s\cdot\vec{k} = \hat{e}_p\cdot\vec{k} = 0$ are relations between complex numbers, but the scalar product definition in this case is given without the complex conjugation of one of the factors, as usually done in the complex number scalar product. The electric field can be, thus, decomposed on the $\left(\vec{e}_p, \vec{e}_s, \vec{k}\right)$ vector base. Assuming, in general, an interface between two different absorbing materials A and B, we can write the s and p transmission coefficients t_s and t_p:

$$t_s = \frac{E_s^{(B)}}{E_s^{(A)}} = \frac{2k_z^{(A)}}{k_z^{(A)} + k_z^{(B)}};\quad t_s = \frac{E_p^{(B)}}{E_p^{(A)}} = \frac{2\sqrt{\varepsilon_A\varepsilon_B}k_z^{(A)}}{\varepsilon_B k_z^{(A)} + \varepsilon_A k_z^{(B)}}$$

This two coefficients give the percentage of transmitted and reflected waves across the AB interface (going from A to B). The same can be done for the three Cartesian components of the electric field, leading to the following relationships:

$$L_{xx} = \frac{E_x^{(B)}}{E_x^{(A)}} = \frac{2\varepsilon_A k_z^{(B)}}{\varepsilon_B k_z^{(A)} + \varepsilon_A k_z^{(B)}} \tag{5.2}$$
$$L_{yy} = \frac{E_y^{(B)}}{E_y^{(A)}} = \frac{2k_z^{(A)}}{k_z^{(A)} + k_z^{(B)}}$$
$$L_{zz} = \frac{E_z^{(B)}}{E_z^{(A)}} = \frac{2\varepsilon_A k_z^{(A)}}{\varepsilon_B k_z^{(A)} + \varepsilon_A k_z^{(B)}}$$

These are the diagonal components of the so-called "Fresnel tensor" $\tilde{L}$. Into an isotropic medium, the out-diagonal terms are vanishing, as in this case. Note that $\tilde{L}$ depends on the frequency as ε does. Let us consider, from now on, the case of a vacuum-sample interface.

The Fresnel tensor can be useful also in writing the nonlinear polarization, as defined in Eq. 1.5, inside the medium. Let us consider two input waves, having frequencies $\omega_{1,2}$ and incident angles $\beta_{1,2}$, as shown in Fig 5.1. The term of Eq. 1.5 given by Eq. 1.22, which oscillates at the Stokes (anti-Stokes) frequency, is

$$P_i(\vec{r},\omega_4) = 3\chi^{(3)}_{ijhk}(-\omega_4,\omega_1,\omega_1,-\omega_2)E_j(\vec{r},\omega_1)E_h(\vec{r},\omega_1)E^*_k(\vec{r},\omega_2).$$

Inside the medium, a refracted input wave can be written as $\vec{E}(\vec{r},t) = \vec{E}_0\exp(i(\vec{k}\cdot\vec{r}-\omega t))$, where $\vec{E}_0 = \left(\tilde{L}\cdot\hat{e}\right)E$. Here $\hat{e}$ is the polarization unit-vector of the external field, E is its amplitude and $\vec{k}$ is the wave-vector inside the medium as given by Eq. 5.1. The nonlinear polarization, thus, become:

$$\vec{P}_{NL,i}(\vec{r}) = P_i(\vec{r},\omega_4) = P_{0i}\exp\left(i\vec{k}_p\cdot\vec{r}\right)$$

where

$$\vec{k}_p = 2\vec{k}_1 - \vec{k}_2 \Rightarrow \begin{cases} k_{px} = 2k_{1x} - k_{2x} = (2\omega_1\sin\beta_1 - \omega_2\sin\beta_2)/c \\ k_{pz} = (2k'_{1z} - k'_{2z}) + i\,(2k''_{1z} + k''_{2z}) \end{cases}$$

and

$$P_{0i} = 3\chi^{(3)}_{ijhk}E_{01j}E_{01h}E^*_{02k} = \chi^{(3)}_{ijhk}L_{1jj'}L_{1hh'}L^*_{2kk'}e_{1j'}e_{1h'}e^*_{2k'}E_1^2E_2^* \tag{5.3}$$

where L_{1ij} and L_{2ij} are the Fresnel tensors relative to the frequencies $\omega_{1,2}$. Note that in the imaginary parts of k_{pz} are summed instead of being subtracted.

5.1.2 The radiated FWM field.

In order to calculate the radiated external field, we have firstly to find the complete expression of the electric and magnetic internal fields and then to apply the surface boundary conditions. The Maxwell equations which rules the internal fields are

$$\nabla\times\vec{E} = -\frac{\partial\vec{B}}{\partial t} = i\omega_4\vec{B} \tag{5.4}$$
$$\nabla\times\vec{B} = \mu_0\frac{\partial\vec{P}_{NL}}{\partial t} + \mu_0\varepsilon_0\varepsilon_4\frac{\partial\vec{E}}{\partial t} = -i\frac{\omega_4}{c^2}\left(\frac{1}{\varepsilon_0}\vec{P}_{NL} + \varepsilon_4 E\right)$$

where ε_4 is the relative dielectric constant at frequency ω_4. The solution will be the sum between the solution of the associated homogeneous equation and a particular solution. The former is an usual plane-wave (or a linear combination of plane-waves) of the form

$$\vec{E}_0(\vec{r}) = \vec{A}\exp(i\vec{k}_4\cdot\vec{r}) \tag{5.5}$$
$$\vec{B}_0(\vec{r}) = \frac{\vec{k}_4\cdot\vec{A}}{\omega_4}\exp(i\vec{k}_4\cdot\vec{r})$$

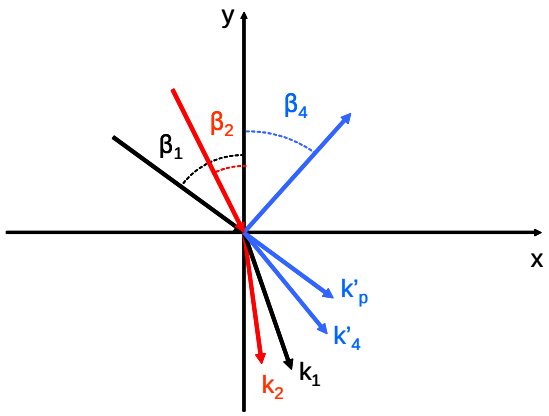

Figure 5.1: Wave-vectors directions of incident waves and radiated FWM wave.

where $\vec{k}_4$ is, for the moment, a generic wave-vector, and $\vec{A}$ is a constant vector, normal to $\vec{k}_4$, which has to be fixed by the boundary conditions. A particular solution of Eq. 5.4 can be found by assuming that all fields depend on space as the driving polarization does, i.e. as $\exp(i\vec{k}_p \cdot r)$. This approach leads to

$$\vec{E}_p(\vec{r}) = \frac{\vec{P}_0 k_4^2 - \left(\vec{k}_p \cdot \vec{P}_0\right)\vec{k}}{\varepsilon_0 \varepsilon_4 \left(k_p^2 - k_4^2\right)} \exp(i\vec{k}_p \cdot \vec{r}) \tag{5.6}$$

$$\vec{B}_p(\vec{r}) = \frac{k_4^2 \vec{k}_p \times \vec{P}_0}{\varepsilon_0 \varepsilon_4 \omega_4 \left(k_p^2 - k_4^2\right)} \exp(i\vec{k}_p \cdot \vec{r})$$

The total solution is, thus, the sum of Eq. 5.5 and 5.6. Since there is not any input wave at frequency ω_4, the boundary conditions will give $A = 0$ for each $\vec{k}_4$ which is not matched with the driving term, i.e. $\vec{k}_4$ have to satisfy the phase-matching relation (Eq. 1.23), which is, in our notation:

$$k_{4x} = k_{px} = 2k_{1x} - k_{2x} = (2\omega_1 \sin\beta_1 - \omega_2 \sin\beta_2)/c$$

and, thus, the exit angle β_4 is given by

$$\sin\beta_4 = \frac{k_4}{\omega_4/c} = \frac{2\omega_1 \sin\beta_1 - \omega_2 \sin\beta_2}{2\omega_1 - \omega_2}.$$

The z component if the FWM wave-vector is given by the phase-matching and the dispersion relationships:

$$k_{4z} = -\sqrt{\varepsilon_4 \frac{\omega_4^2}{c^2} - k_{4x}^2} = -\frac{\omega_4}{c}\sqrt{\varepsilon_4 - \sin^2\beta_4}.$$

Note, here, that the opposite solution have to be excluded since it diverges for $z \to -\infty$.

As previously mentioned, the vector constant $\vec{A}$ has to be determined from the xy surface boundary conditions. It is easy to see that such conditions cannot be

satisfied if there is not any generated field outside the medium. This external field can be informally called "reflected FWM wave" even if one has to keep in mind that it is not a reflected wave at all. Its presence is actually due to the material surface acting as a wave-source.

Let us write, now, the radiated external field as a normal plane-wave expression, which holds for $z \gg 0$:

$$\vec{E}_R(\vec{r}) = \vec{A}_R \exp(i\vec{k}_R \cdot \vec{r})$$
$$\vec{B}_R(\vec{r}) = \frac{\vec{k}_4 \cdot \vec{A}_R}{\omega_4} \exp(i\vec{k}_R \cdot \vec{r})$$

where $\vec{k}_R$ is the wave-vector in vacuum, fixed by the boundary condition $k_{Rx} = k_{4x}$, which satisfies the vacuum dispersion law $k_R = \omega_4/c$. The field amplitude $\vec{A}_R$ has to be determined by the boundary conditions, and it is always normal to $\vec{k}_R$. Since the tangential (xy) electric and magnetic fields have to be continuous across the boundary, the bulk value of the vector constant is

$$A_y = \frac{\omega_4^2 (k_{pz} - k_{Rz})}{\varepsilon_0 c^2 \left(k_p^2 - k_4^2\right)(k_{Rz} - k_{4z})} P_{0y}$$
$$A_x = -\frac{k_{4z}}{k_{4x}} = \frac{k_{4z}\left[\left(k_{4z}^2 - \varepsilon_4 k_{Rz} k_{pz}\right) P_{0x} + k_{4x}\left(\varepsilon_4 k_{Rz} - k_{pz}\right) P_{0z}\right]}{\varepsilon_4 \varepsilon_0 \left(k_p^2 - k_4^2\right)\left(\varepsilon_4 k_{Rz} - k_{4z}\right)}$$

and the radiated field amplitude is given by

$$A_{Ry} = \frac{\omega_4^2 (k_{pz} - k_{4z})}{\varepsilon_0 c^2 \left(k_p^2 - k_4^2\right)(k_{Rz} - k_{4z})} P_{0y} = \frac{\omega_4^2 P_{0y}}{\varepsilon_0 c^2 (k_{pz} + k_{4z})(k_{Rz} - k_{4z})}$$
$$A_{Rx} = -\frac{k_{Rz}}{k_{Rx}} A_{Rz} = -\frac{k_{Rz}(k_{pz} - k_{4z})(k_{4z} P_{0x} + k_{4x} P_{0z})}{\varepsilon_0 \left(k_p^2 - k_4^2\right)\left(\varepsilon_4 k_{Rz} - k_{4z}\right)} =$$
$$= -\frac{k_{Rz}(k_{4z} P_{0x} + k_{4x} P_{0z})}{\varepsilon_0 (k_{pz} + k_{4z})\left(\varepsilon_4 k_{Rz} - k_{4z}\right)}$$

Introducing an analysis polarizer, with a polarizing unit-vector $\hat{e}_4$ (even complex in the case of a circular polarization), one can find the field amplitude $E_R = \hat{e}_4^* \cdot \vec{A}_R$ from the vector amplitude $\vec{A}_R$. In particular the s and p components of the radiated field can be found from the positions $\hat{e}_4 = \hat{e}_{4s} = (0, 1, 0)$ and $\hat{e}_4 = \hat{e}_{4p} = (-k_{Rz}, 0, k_{Rz}) = (-\cos\beta_4, 0, \sin\beta_4)$.

The radiated field can be written in an useful and compact form with the help of the vacuum-to-medium Fresnel tensor $\tilde{L}_4$ at frequency ω_4 and incident angle β_4, as defined in Eq. 5.2, with A = vacuum and B = medium:

$$E_R = -\frac{\zeta}{\lambda_4 \varepsilon_0}\left(\tilde{L}_4 \cdot \hat{e}_4^*\right) \cdot \vec{P}_0 = -\frac{\zeta}{\lambda_4 \varepsilon_0} e_{4i'}^* L_{4i'i} P_{0i} \tag{5.7}$$

where $\lambda_4 = 2\pi c/\omega_4$. The "oblique coherence length" ζ is given by

$$\zeta = -\frac{\pi k_R}{k_R (k_{4z} + k_{pz})} =$$
$$= \frac{\pi}{\cos\beta_4 \left[\sqrt{\varepsilon_4 - \sin^2\beta_4} + 2\sqrt{\varepsilon_1 - \sin^2\beta_1} - \left(\sqrt{\varepsilon_2 - \sin^2\beta_2}\right)^*\right]}$$

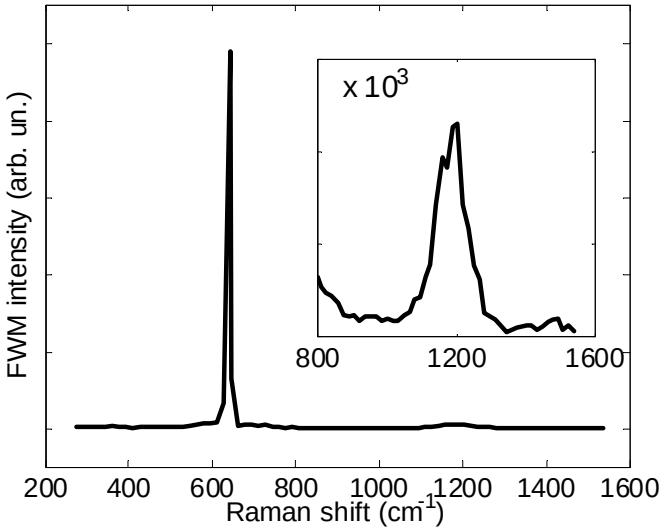

Figure 5.2: CARS spectrum of a BBO single crystal. The well-known phonon line at 640 cm^{-1} is clearly seen, without any electronic background. Inset: zoom of the same spectum, a possible second order line appears at about 1200 cm^{-1}.

It is further to note that the vector $\tilde{L}_4 \cdot \hat{e}_4^*$ is normal to the vector $\vec{k}_E = (k_{4x}, 0, -k_{4x})$. This wave-vector corresponds to that of a wave travelling from inside the medium toward positive z, which would get refracted into the radiated wave direction at the medium surface. Therefore, the scalar product $\left(\tilde{L}_4 \cdot \hat{e}_4^*\right) \cdot \vec{P}_0$ in the radiated field expression corresponds to the physical fact that only the transverse component of the polarization vector can radiate, as expected.

Inserting Eq. 5.3 into Eq. 5.7 we can get the final expression of the radiated field:

$$E_R = -\frac{3\zeta}{\lambda_4 \varepsilon_0} \chi_{eff} E_1^2 E_2^*$$

with

$$\chi_{eff} = e_{4i'}^* L_{4i'i} \chi_{ijhk}^{(3)}(-\omega_4, \omega_1, \omega_1, -\omega_2) L_{1jj'} L_{1hh'} L_{2kk'}^* e_{1j'} e_{1h'} e_{2k'}^*.$$

5.2 First CRS spectra.

The first material we used as a test for our experimental setup was again the BBO crystal. In Fig 5.2 the CARS spectrum of BBO is shown. The spectrum shows a single very strong line at about 640 cm^{-1}, which corresponds to a well-known BBO phonon-line. No background noise is present, and no non-resonant background is seen. The most interesting feature of this spectrum, is the presence of a second broader line at about 1200 cm^{-1}. We ascribe it to the second order scattering from the same resonance. This possibility was almost skipped in the theoretical treatment of the FWM, since it is usually very difficult to see it. In this case, the

very strong nonlinear behaviour of the BBO crystal, and the complete absence of the non-resonant background, makes possible to reveal it, even if it is three orders of magnitude less intense. In a second order scattering process, two phonons are created in a single scattering event. This means that the phase-matching condition holds for the vector sum of the two wave-vectors, so that the single phonon wave-vector is no longer constrained to be almost vanishing, as in the case of the first order process. This is the reason why the second order line is usually broader than the first order one, as in this case. The second order process, indeed, can investigate the whole Brillouin zone, and not only the Γ ($\vec{k} \sim 0$) point.

A second test measurement was performed on a material which is closer to the target of this work: a bulk germanium crystal, with unknown crystal axes orientation and purity degree. To our knowledge, very few works have been dedicated to the nonlinear spectroscopy on this material [84]. Germanium has only one Raman-active phonon, it is a semiconductor without any marked nonlinear property, and it is, thus, a good trial of both the experimental setup as well as the best-fit procedure. We tried different polarization combinations. Each combination of the four beams is related to a different element of the third order susceptibility $\chi^{(3)}_{ijhk}$. In the simplified geometry (i.e. when the Pump beam acts as a Probe beam too) the Pump and the Probe polarizations are, of course, the same. Moreover, we found that the FWM intensity is always vanishing if the Tune and the revelation polarizations are not parallel. This lowers the possible combinations to four: HH, VV, HV and VH, where H means horizontal and V means vertical compared to the setup plane. Since in our geometry the incident angles are very small, the approximation HH=VV and HV=VH holds true. However, we tested this approximation by comparing the "parallel" (HH, VV) spectra between them as well as the "crossed" (HV,VH) spectra, and we did not find any difference (HH≡VV, HV≡VH). In Fig 5.3 the crossed (a) and parallel (b) spectra of bulk germanium are shown. In the crossed-polarization spectra, a ~ 310 cm^{-1} phonon-line is clearly seen both in CSRS and CARS spectra. The difference in their relative height may be due to a different scattering efficiency on the two side, even if we can not exclude some minor effects caused by an imperfect spectral correction. In the parallel-polarization spectra, the same phonon resonance is seen on both sides, together with a strong non-resonant background. The phonon-line have not the same shape on the Stokes and anti-Stokes sides: this is due to the coherent interference between them and the background. This background can only be ascribed to an electronic response, and it is found to decrease approximately as the Raman shift $\Delta\omega$. The ~ 310 cm^{-1} phonon line has the T_{2g} symmetry, and, thus, its off-diagonal matrix elements in the dielectric susceptibility are not vanishing, and that line is visible in the crossed-polarization spectra. The electronic continuum, on the contrary, has a A_{1g} symmetry, its matrix is diagonal, and it is present only in the parallel-polarization spectra. This allows us to use a two-step fitting procedure: the cross-polarization spectra are used to fit very easily the resonance frequency and its spectral width. These two values are then used as fixed parameters in the parallel spectra best fit. Being $I(\Delta\omega)$ the measured FWM intensity, the CRS spectrum near a resonance ω_0 is given by Eq.

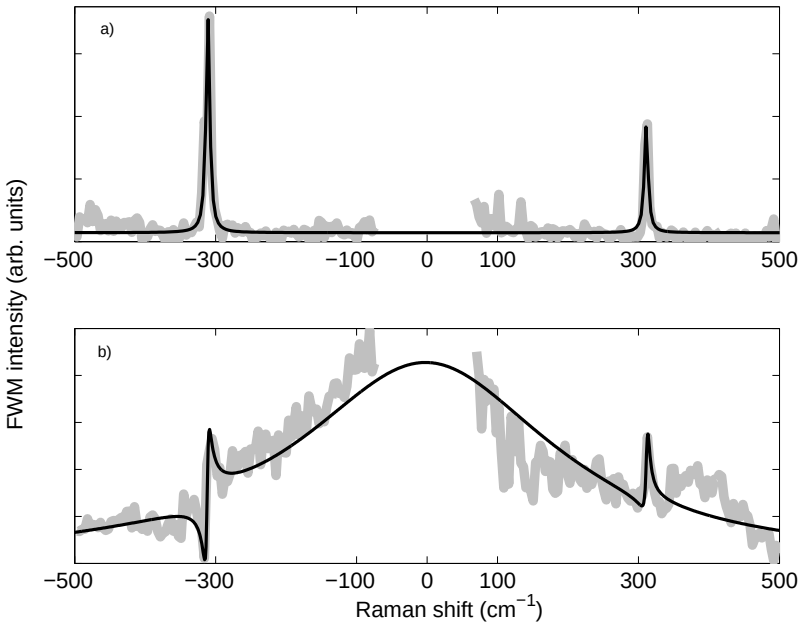

Figure 5.3: CRS spectra of bulk germanium in a crossed (a) and parallel (b) polarization geometry. Gray curves are the data, black solid line is the best-fit curve.

1.16:

$$I(\Delta\omega) \propto |\chi_R(\Delta\omega)|^2 \propto \left| \frac{1}{\Delta\omega + \omega_0 + i\gamma} - \frac{1}{\Delta\omega - \omega_0 + i\gamma} \right|^2$$

where ω_0 is the phonon frequency and γ is its spectral width. From the crossed polarization spectra (fitted together) we have $\omega_0 = 311$ cm^{-1} and $\gamma = 3.2$ cm^{-1}. Actually, one has to note that the value of γ is too close to the spectral resolution to be taken as a reliable measurement; it is rather an upper limit. In order to take into account for the electronic background, a zero-resonance, having a Lorentzian shape too, was used. The whole spectrum fitting formula is, thus:

$$I(\Delta\omega) \propto \left| \frac{A}{\Delta\omega + i\Gamma} + \left(\frac{B}{\Delta\omega + \omega_0 + i\gamma} - \frac{C}{\Delta\omega - \omega_0 + i\gamma} \right) \exp(i\varphi) \right|^2$$

where A, B, C are constants, Γ is the spectral width of the zero-resonance and φ is the relative phase between the phonon and the non-resonant background (whose phase is set to zero). This second fit gives $\Gamma = 220$ cm^{-1} and $\varphi = \pi$. Although some minor features of the background shape are not correctly reproduced, the major part of the qualitative features are taken into account by this model. We take it, therefore, as a reference model for the YBCO spectra fitting procedure.

Finally, Fig 5.4 shows the first CRS spectra of an HTCS thin film. To our knowledge only very few works have been dedicated to this subject [85], [86], [89]. The studied samples are two optimally doped twinned YBCO commercial thin films (provided by the German company "Theva"), grown on 10×10 mm^2 MgO substrate, and with the $c-$axis normal to the sample surface. Samples have a thickness

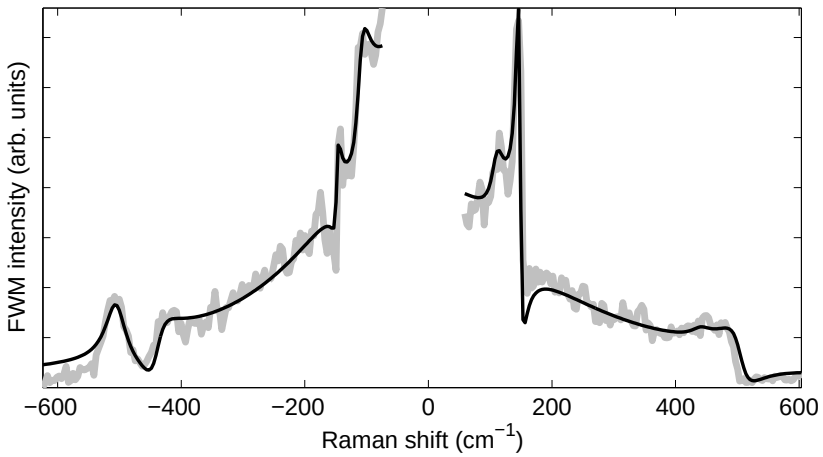

Figure 5.4: CRS spectra of an optimally doped YBCO thin film in a parallel polarization geometry. Gray curves are the data, black solid lines are the best-fit curves.

of 500 and 600 nm and a critical temperature of 84.5 and 87 K, respectively. All spectral features are found to be reproducible in each sample and very similar between different samples. No damage was seen after each measure session. Since the optical absorption length ($\sim$ 100 nm) at our wavelengths is smaller than the sample thickness, no substrate contribution to the FWM signal is expected to be seen.

Unlike germanium, the YBCO crossed polarization spectra are almost vanishing, and, thus, they are not shown here. The parallel polarization spectra show, similarly to germanium, a broad continuum on which narrow spectral features are superimposed. The spectral positions of all these features correspond to four of the five Raman-active phonons of YBCO we studied in Ch. 3. All of them have the same symmetry of the continuum, i.e. the A_{1g} symmetry. This can explain why the crossed polarization spectra are vanishing. The only missing phonon is the $\sim$ 350 cm^{-1} one. It is too much weak to be seen, with respect to the strong background, probably because its symmetry properties ($\sim B_{1g}$) are slightly different from those of the other phonons, as shown in Ch. 3. The shape of the CSRS and the CARS spectra is very different in this case, because of the different interference between each phonon and the background and also (since this time there are more than one phonon) between close phonon pairs: the $\sim$ 115 and $\sim$ 150 cm^{-1} phonons are found to be clearly present in both side, the $\sim$ 440 and $\sim$ 500 cm^{-1} phonons are much less intense. The $\sim$ 440 cm^{-1} line, in particular is almost absent (except for a very slight bump) in the CARS spectrum, but it is present as a "step" in the Stokes side. The same "step shape" is found for the $\sim$ 500 cm^{-1} line on the anti-Stokes side. The spectral shape of the underlying electronic background is different in the two sides too. As a consequence, it is not possible to fit these spectra as previously done for germanium: some changes have to be made.

In order to take into account for the different spectral shape of the zero-resonance, we used two distinct functions having two different widths in the Stokes and anti-

Stokes sides. Moreover, each phonon resonance must have its own phase in the Stokes and anti-Stokes sides ($\varphi_S \neq \varphi_a$). Stokes and anti-Stokes lines have the same width γ. Finally, in order to have a stable fit with respect to the initial parameters, the observed resonance frequencies are fixed.

Within these hypotheses, we found the following values for the involved parameters:

ω_0 (cm^{-1})	φ_S	φ_a	γ (cm^{-1})
110	$\pi/2$	π	11.9
148	$-\pi/3$	$-\pi/3$	3.9
440	$-\pi/3$	$-2\pi/3$	18.4
505	$-\pi/3$	0	20.1

The zero-resonance width was found to be $\Gamma_S = 172.5$ cm^{-1} in the Stokes side and $\Gamma_a = 231.6$ cm^{-1} in the anti-Stokes one. Some attempt to directly measure the phonon lifetimes was made, but our time resolution does not allow us to find out a reliable value, since the typical phonon lifetime is of the order of few picoseconds.

In ref [89], the zero-resonance is possibly ascribed to the electron-phonon thermalization process, but the linewidth is not consistent with our results.

The Raman electronic continuum was found to have some "anomalous" features ([87], [88]) in linear Raman spectra too. In principle, the addition of a complex constant in the fitting formula could take into account for the zero-resonance asymmetry, since the interference between this constant and the background can distort its shape, but this approach is unable to give a good fit. More and deeper investigations have to be done in order to better clarify the microscopic nature of this electronic background. In particular, it is necessary to study different samples having different $c-$axis orientations, in order to find the missing 350 cm^{-1} phonon, and to study the temperature dependence of the electronic continuum, as already done with linear Raman scattering in the above mentioned references.

We have to note that the phonon phases can be drawn out by means of the linear Raman spectroscopy too, as done, for instance, in ref [25] for $SmBaCuO$. In that case, it is possible to measure the relative phase-shift between different matrix elements of the Raman tensor. These results cannot be compared, thus, with the ones here reported, since in our experiment, the relative phase-shift between a given phonon and the electronic background is measured. However, it is not possible to exclude that there is a link between these phase shifts. Finally, in linear Raman spectra of YBCO, there is an electronic background, and phonons interfere with it, but we found quite different behaviours, suggesting that the CRS non-resonant background may have a different nature from the so-called "anomalous Raman continuum".

Besides these results, our work demonstrates the feasibility of this kind of technique. CRS can investigate the low-energy excitations of HTCS, which are the most interesting spectral features for superconductivity. It preserves the information about the phases. It is very sensitive to the electronic response and it can selectively excite one excitation and study its lifetime. All these features make the CRS a very promising tool for a better understanding of the underlying mechanism of high-Tc superconductivity.

Part II

Time-resolved Photoluminescence of STO.

Chapter 6

Photoluminescence in solid state.

In order to introduce the time-resolved measurements presented in Ch. 8, a brief overview on the main features of the phenomena on which the experiment is based, is given in this Chapter. We will try to give a theoretical description of the principal photoluminescent transitions, and of the main elementary excitations which are involved in this process.

6.1 Absorption of light.

In order to reach an understanding of the principal features of the photoluminescence process, let us start with a brief summary on the optical properties of solids: we want to stress, in particular, the direct (indirect) transitions and the concept of exciton and polariton.

6.1.1 The Drude-Lorentz Model.

The simplest theory describing the general optical properties of a solid is the Drude-Lorentz model. The assumption is that the solid contains charged particles which behave like dumped classical harmonic oscillators, with mass m, charge e and proper frequency $\omega_0 = \sqrt{K/m}$, where K is the Hook constant. Introducing an electric field in the y direction, with frequency ω, the equation of these oscillators is

$$m\frac{d^2y}{dt^2} + m\gamma\frac{dy}{dt} + \omega_0^2 my = eE_0e^{-i\omega t} \quad , \tag{6.1}$$

where γ is the dumping coefficient. The stationary solution of this equation is

$$y = \frac{eE_0e^{-i\omega t}}{m\left[\left(\omega_0^2 - \omega^2\right) - i\gamma\omega\right]} \quad . \tag{6.2}$$

Now, we introduce the number of oscillators per unit volume N so that the

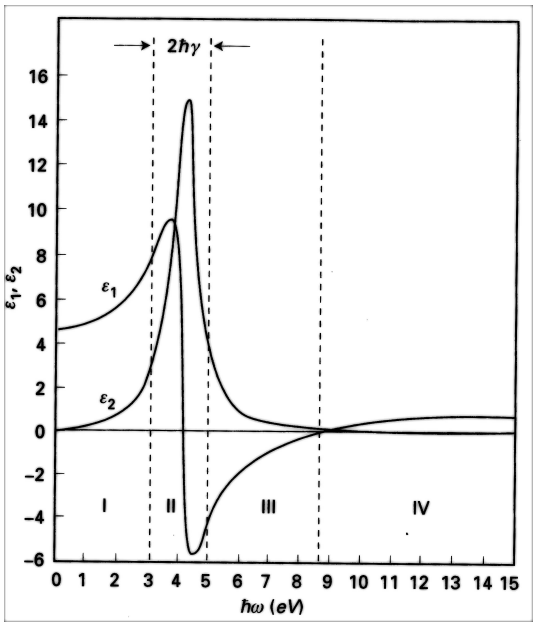

Figure 6.1: Frequency behaviour of the dielectric function [32].

polarization vector induced by them is

$$P = Ney = \frac{Ne^2}{m}\frac{1}{\left(\omega_0^2 - \omega^2\right) - i\gamma\omega}E_0 e^{-i\omega t} = \alpha E \tag{6.3}$$
$$a = \frac{Ne^2}{m}\frac{1}{\left(\omega_0^2 - \omega^2\right) - i\gamma\omega} \ ,$$

and finally, since $\varepsilon(\omega) = 1 + 4\pi\alpha$, we can find the real and imaginary parts of the dielectric constant:

$$\varepsilon_1(\omega) = 1 + \frac{4\pi Ne^2}{m}\frac{\omega_0^2 - \omega^2}{\left(\omega_0^2 - \omega^2\right)^2 + \omega^2\gamma^2} \tag{6.4}$$
$$\varepsilon_2(\omega) = \frac{4\pi Ne^2}{m}\frac{\omega\gamma}{\left(\omega_0^2 - \omega^2\right)^2 + \omega^2\gamma^2} \ .$$

As it is possible to see from Fig 6.1, there are four different regions in the frequency domain: the transparent regions (I and IV), the absorbing region (II) and the reflective region (III). In region II, the absorbing peak has a Lorentzian lineshape.

It is also possible to take into account the presence of many oscillators, with different proper frequencies ω_i. Each oscillator has its own weight, in the sum,

called "oscillator strength" f_i so that

$$\varepsilon(\omega) = 1 + \frac{4\pi e^2}{m} \sum_j \frac{f_j}{\left(\omega_j^2 - \omega^2\right) - i\gamma_j \omega} \tag{6.5}$$

$$\sum_j f_j = N \ .$$

In the case of a metal, free-electrons can be treated as harmonic oscillators with $K = 0$ so that $\forall j \ \omega_j = 0$, $f_j = 1$, and $\gamma_j = \gamma$. The dielectric constant becomes

$$\varepsilon(\omega) = 1 - \frac{\omega_p^2}{\omega^2 + \gamma^2} + i\frac{\omega_p^2 \gamma}{\omega^3 + \omega\gamma^2} \ , \tag{6.6}$$

where $\omega_p^2 = 4\pi e^2 N/m$ is the plasma frequency, which depends only on the charged particles density. For lower frequencies, the metal has a reflective behaviour, for higher frequencies the metal is transparent, and for frequencies near ω_p it exhibits an absorbing behaviour, the absorbing coefficient η being proportional to $1/\omega^2$.

6.1.2 Quantum Theory.

Let us now look at the transition rates between stationary states $|0\rangle$ (ground state) and $|f\rangle$ (final state) of the system, induced by the electromagnetic perturbation H'. From the Fermi golden-rule, we know that this transition rates are

$$W_{0,f}(k,\omega) = \frac{2\pi}{\hbar} \left|\left\langle f \left| H' \right| 0 \right\rangle\right|^2 \delta(E_f - E_0 - \hbar\omega) \ . \tag{6.7}$$

The perturbative term, at the first order, is

$$H' = -e\left(\vec{A} \cdot \vec{p}\right)/mc \ ,$$

and the electric field, polarized in the $\hat{e}$ direction, is

$$\vec{E} = \hat{e} E_0 e^{i(\vec{q}\cdot\vec{r} - \omega t)} = -\frac{1}{c}\frac{\partial \vec{A}}{\partial t} = \frac{i\omega}{c}\vec{A} \ ,$$

being $\vec{A}$ the vector potential, $\vec{p}$ the electron momentum and $\vec{q}$ the field wave-vector.

Since $W_{0,f}(k,\omega)$ is the number of transitions per unit time and volume, the total absorbed energy is $\sum_f W_{0,f}(k,\omega)\,\hbar\omega$, while the mean energy flux of the electric field is $\frac{c}{n}\langle W\rangle$, with $\langle W\rangle = \frac{n^2}{4\pi^2}\left\langle E^2\right\rangle$. The absorption coefficient η is, then, the ratio between the absorbed and incident energy:

$$\eta \equiv \frac{\sum_f W_{0,f}(k,\omega)\,\hbar\omega}{\frac{c}{n}\langle W\rangle} = \frac{4\pi^2 e^2}{nm^2 c\omega} \sum_f \left|\left\langle f \left| e^{i\vec{q}\cdot\vec{r}}\hat{e}\cdot\vec{p} \right| 0 \right\rangle\right|^2 \delta(E_f - E_0 - \hbar\omega) \ . \tag{6.8}$$

In this case the line-shape of the absorption curve is a Dirac delta function, because we have assumed stationary states with infinite lifetime. Taking into account the spontaneous emission, and calling τ the level lifetime, we have again a Lorentzian line-shape, with a width $\Gamma = \hbar/\tau$.

6.1.3 Direct Interband Transitions.

In the case of electronic transitions in a solid, calling ψ_{c,k_f} a conduction band state and ψ_{v,k_0} a valence band state, the matrix element of this transition is

$$\left\langle \psi_{c,k_f} \left| e^{i\vec{q}\cdot\vec{r}} \hat{e}\cdot\vec{p} \right| \psi_{v,k_0} \right\rangle .$$

From the momentum conservation law, we have $\vec{k}_f = \vec{k}_0 + \vec{q} + \vec{G}$ where $\vec{G}$ is a reciprocal lattice vector. Writing it in the first Brillouin zone (BZ), and keeping in mind that the radiation momentum $q \approx 10^5 cm^{-1}$ is very much lower than the typical dimension of the BZ ($\approx 10^8 cm^{-1}$), we can conclude that only "vertical" transition (i.e. $\vec{k}_f \simeq \vec{k}_0$) are possible[1]. The matrix element becomes, therefore

$$\langle \psi_{c,k} \left| \hat{e}\cdot\vec{p} \right| \psi_{v,k} \rangle = \hat{e}\cdot\int_{vol} \psi_c^* \left(\vec{k},\vec{r}\right) \left(-i\hbar\vec{\nabla}\right) \psi_v \left(\vec{k},\vec{r}\right) d\vec{r} \ . \tag{6.9}$$

6.1.4 Indirect Transitions.

From the momentum conservation law, radiative transitions are not allowed if the maximum of the valence band and the minimum of conduction band have not the same k-vector, as happens in indirect gap materials (as Si or Ge, for instance). Nevertheless, these transitions can occur in a second order process, in which a large k-vector particle (as a phonon) is involved. In this case, the transition rate depends both on the electromagnetic perturbation and electron-lattice coupling.

The electron-lattice perturbation can be written as

$$H'_{eL} = \sum_{R_a} \left[V\left(\vec{r} - \vec{R}_a - \delta\vec{R}_a\right) - V\left(\vec{r} - \vec{R}_a\right) \right] \ , \tag{6.10}$$

where $\vec{R}_a$ and $\delta\vec{R}_a$ are the ions positions in the lattice and their variations and V is the atomic potential. By retaining only the first order term in Eq. 6.10 as a function of $\delta\vec{R}_a$, and using the expansion on normal modes, is possible to show that this Hamiltonian can be written as

$$\begin{aligned} H'_{eL} &= a\left(\vec{q}\right) e^{-i\omega_q t} V_p(\vec{q},\vec{r}) + c.c. \ , \quad \text{where} \\ V_p(\vec{q},\vec{r}) &= \sqrt{\frac{\hbar}{2M\omega_q}} \sum_{R_a} e^{i\vec{q}\cdot\vec{R}_a} \hat{e}\cdot\vec{\nabla}_r V\left(\vec{r} - \vec{R}_a\right) \ . \end{aligned} \tag{6.11}$$

Here ω_q is the phonon frequency, $\vec{q}$ its momentum vector, $\hat{e}$ its polarization unit-vector, and $a\left(q\right), a^\dagger\left(q\right)$ are the destruction an creation operators for phonons.

The first term in Eq. 6.11 generates a phonon destruction and its complex conjugate the creation, both having momentum and energy transfer $\hbar\vec{q}$ and $\hbar\omega_q$, respectively.

The electron-phonon interaction in metals can produce intraband transitions between full and empty states with different k-vector (these transitions are responsible

[1] a second, perhaps trivial, selection-rule is the spin-number conservation, since the electromagnetic perturbation does not depend on spin.

for the electrical resistivity), but it cannot produce by itself interband transitions in insulating or semiconducting materials, because it has not enough energy. If this energy is supplied by an electromagnetic perturbation H'_e, the process may happen, and its probability is given by the second order Fermi golden-rule:

$$W^{(2)}_{0,f}(k,\omega) = \frac{2\pi}{\hbar}\left|\sum_n \frac{\langle f|H'_{eL}|n\rangle\langle n|H'_e|0\rangle}{E_n - E_0 - \hbar\omega} + \frac{\langle f|H'_e|n\rangle\langle n|H'_{eL}|0\rangle}{E_n - E_0 \pm \hbar\omega_q}\right|^2 \cdot \tag{6.12}$$

$$\cdot\,\delta(E_f - E_0 - \hbar\omega \pm \hbar\omega_q) \quad . \tag{6.13}$$

Note that the energy is conserved only in the whole transition going from ψ_{v,k_0} to ψ_{c,k_f} and not in all virtual transitions through virtual states $\psi_{n,k}$. The creation and destruction operators depend on the number of phonons n_q, so that the optical constants for indirect transitions depends on the temperature according to the Bose-Einstein distribution. This dependence of the absorption constant on temperature is the clearest sign of an indirect transition.

The absorption coefficient, as defined in Eq. 6.8, is made by two different terms, one which concerns the emission of a phonon and the other which concerns an absorption:

$$\eta(\omega) = \eta_{em}(\omega) + \eta_{ab}(\omega) \quad .$$

The exact calculation of these quantities requires the knowledge of the band structure.

From an experimental point of view, in all indirect semiconductors it is observed a low-intensity tail in the absorption spectrum just before the beginning of the intense absorption peak of direct interband transitions. This tail is due to the indirect transitions, and it is possible to find it in some insulating materials with a particular electronic structure: this is useful in some photographic processes, where the light is absorbed via an indirect process so that the final state has a very long lifetime, because electrons have a very different k-vector compared to holes, so that they cannot relax directly. This fact is responsible for the creation of $Ag-$clusters, and these clusters will form the picture on the photographic film.

These transitions are important in metallic intraband transitions too, where two states (one above and the other below the Fermi energy) with very different k-vector are coupled by the lattice vibrations: in this case, the radiation frequencies are very low (little energy transfer) and the k-vector needed for the transition is almost always given by an acoustic phonon. This calculation of the transition rate can be still applied, but we have to keep in mind that the starting and the final band are the same. At higher frequencies very intense direct interband transitions appear in metals too.

6.1.5 Excitons.

Optical transitions always produce an electron-hole pair. We are used to regard this pair as a free-electron in the conduction band and a free-hole in the valence band. Nevertheless, it is also possible that one electron and one hole, attracting each other by the Coulomb force, behave as a single neutral particle with integer spin: this particle is the so-called "excited bound state" or "exciton".

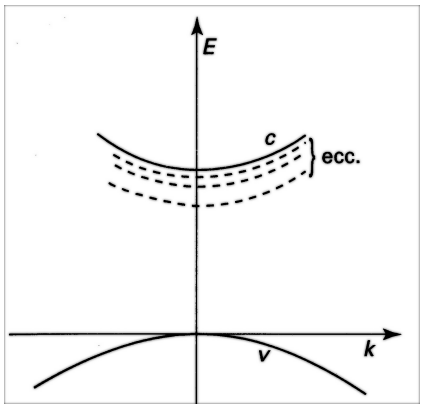

Figure 6.2: Excitons in-gap levels [32].

The first evidence of the existence of these particles (suggested by Frenkel and Peierls) was found in the absorption spectra of pure semiconductors, where there are absorption peaks at energies lower than the energy-gap. The exciton in-gap levels are shown in Fig 6.2.

Because of the binding energy, the energy required to form the exciton is lower than the energy-gap: it means that the bound state is energetically more favoured than the free-pair. Excitons can transport energy, but not current, as they are neutral. They can also be destroyed (electron-hole recombination), producing a photon.

The binding energy of the pair is calculated quite well within a simple two-body model with a Coulomb potential which gives the well-known hydrogenoic levels:

$$E_n = E_{gap} - \frac{\mu e^4}{2\hbar^2 \varepsilon^2} \frac{1}{n^2} \quad , \tag{6.14}$$

where n is the principal quantum number, ε is the static dielectric constant, and μ ($\sim 0.5 m_e$) the reduced mass of the pair (calculated using the effective masses of both electron and hole). In semiconductors ($\varepsilon \sim 10$), this energy is typically of the order of magnitude of few millielectronVolt, so this is a weak bound and electron-hole distance in the lattice is usually about ten times the lattice parameter (Wannier-Mott excitons); on the contrary in insulators, since $\varepsilon \sim 2 - 3$, this energy is higher ($\sim 1\,\mathrm{eV}$), the electron-hole distance is about one lattice parameter, and the exciton is much more localized (Frenkel-Peierls excitons).

In order to set out the quantum description of the bounded pair, we can start from the ground-state ψ_0 which is given by a Slater determinant with all N electrons occupying the whole valence band. The excitations produce a final state ψ_f made from the same Slater determinant with $N - 1$ electrons in the valence band, and just one electron in the conduction band. This state must solve the Schroedinger equation $H_e \psi_f = E \psi_f$, where H_e contains four terms: the kinetic energy of electrons, the spin-orbit term, the Coulomb potentials between each electron and between electrons and ions. This N-particles equation can be reduced to a two-particles equation since the $N - 1$ electrons of the valence band behaves as a single particle

(hole) with charge, spin and momentum opposite to the missing electron. Calling ψ_e (and ψ_h) the state of the electron (hole), we can write ψ_f as a linear combination of products $\psi_h\psi_e$ and the effective Hamiltonian resulting in this way is

$$H_{eff}\left(r_1 r_2\right) = H_s(r_1) - H_s(r_2) - e^2/\varepsilon\left|r_1 - r_2\right| + eV_{ex} \quad , \tag{6.15}$$

where H_s is the single-particle Hamiltonian, which gives the energy band for non-interactive particles, the third term is the Coulomb interaction and the last term is the (in most cases negligible) exchange-potential, due to the form of the Slater determinant, which ensures the correct anti-symmetrization of the total wave-function.

It is possible to solve the eigenvalues problem in the so-called "effective mass approximation", where the energy bands are approximated at the second order near their stationary points, and, thus, to find out the binding energy given in Eq. 6.14. In order to obtain the total energy of the exciton, we have, of course, to add the kinetic energy of the center of mass $\left(\hbar^2 Q^2\right)/2\left(m_e + m_h\right)$, where $\vec{Q}$ is the momentum of the center of mass, and an additional term, due to the exchange-potential: this term have two different values according to the direction (parallel or normal) of the dipole momentum of the exciton with respect to $\vec{Q}$.

6.1.6 Polaritons.

In the anomalous dispersion region, where the dielectric constant varies very rapidly with ω with a negative slope, photons strongly couple with the polarization of the material. This means that we can no longer think of "photons" in the same way we are used to do in the vacuum: we have to think about them as "polaritons". This happens for every resonance of the system, so that we have to specify which kind of polariton we are referring to. For instance, there are phonon-polaritons if we are near a phonon resonance, or there are exciton-polaritons if we are near an exciton resonance. In the last case, for transverse excitons, we can write the exciton contribution to the dielectric constant given in Eq. 6.5:

$$\varepsilon\left(\omega, k\right) = 1 + \frac{4\pi e^2}{m}\sum_n \frac{f_n}{\left(\omega_n^2\left(k\right) - \omega^2\right) - i\gamma\omega} \quad , \tag{6.16}$$

where

$$\hbar\omega_n\left(k\right) \simeq E_n + \frac{\hbar^2 k^2}{2\left(m_e + m_h\right)}$$

is the energy of the transverse exciton (note that the k-dependence, i.e. the dispersion, is held by the free motion of the center of mass) and f_n are the oscillator strengths which drive the polarization of the medium. These quantities can be calculated, for each resonance, starting from the dipole momentum of the exciton, which is the matrix element of the dipole operator between the ground-state and the excited-state:

$$f = \frac{2m\left(E_f - E_0\right)}{\hbar}\left|\left\langle f\left|\vec{r}\right|0\right\rangle\right|^2 \quad .$$

In the case of longitudinal excitons, it is quite the same, but we have to add a term Δ_{LT}, proportional to f and very much lower than the binding energy, because of the exchange-potential.

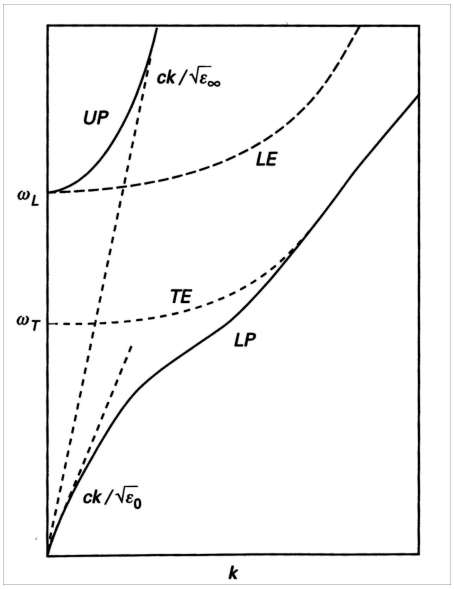

Figure 6.3: Polaritons dispersion curves [32].

Inserting the dielectric constant of Eq. 6.16 in Maxwell equations, we can finally solve the dispersion equation

$$\varepsilon(\omega, k) = \frac{\omega^2}{c^2} k^2$$

for transverse modes, and

$$\varepsilon(\omega, k) = 0$$

for longitudinal modes.

These curves, together with the free-exciton dispersion curves (dashed lines), are plotted in Fig 6.3, where UP/LP is the upper/lower polariton and LE/TE is the longitudinal/transverse free-exciton. Note that the transverse-exciton and the photon are always coupled near the excitation frequency, where two polariton modes, upper and lower, appear: both modes are present in the crystal for $\omega \geq \omega_L$.

The concept of polariton modifies the way we think of light absorption in crystals: when a photon enters the crystal, it becomes a polariton and this polariton changes gradually its k-vector, interacting with the lattice vibration; during these interactions it loses energy, according to the dissipative term γ in Eq. 6.16, which goes into the lattice as thermal energy. The absorption peak is, thus, due to the fact that, in the anomalous dispersion region, the group-velocity decreases very rapidly, as the collision process effectiveness increases.

6.1.7 Two-Photon Transitions.

This kind of processes are characterized by an absorption peak at frequency

$$\hbar(\omega_1 + \omega_2) = E_{gap} - \frac{\mu e^4}{2\hbar^2 \varepsilon^2} \frac{1}{n^2} \quad .$$

It is interesting to make some considerations on the selection rules. If the crystal has not a center of inversion, $s-$states are excitable both with one or two photons, but, in this case, some other transitions are allowed, as, for instance, longitudinal excitons. If the crystal has a center of inversion, the parity conservation law holds true. $S-$states are the accessible with one photon, but are forbidden with two; in this case the final state must be even, since the product of two dipole operators is even.

Moreover there is the possibility to directly verify the polaron nature of excitons, looking at the dispersion curve due to the motion of the center of mass. From the momentum conservation law, we have

$$\vec{q_1} + \vec{q_2} = \vec{k} \ ,$$

where $\vec{k}$ is the momentum of the center of mass and $\vec{q}_{1,2}$ the momenta of photons. In this way, we can find the resonance frequency at different $\vec{k}$ by varying the angle between the two beams which produce the transition, and have, directly, the dispersion curve. This experiment can reveal, for instance, the presence of two distinct peaks, which became more and more separated, as the angle is reduced (as $\vec{k}$ increases): they are the upper polariton and the longitudinal exciton we showed before.

6.2 Photoluminescence.

We have seen how a crystal can absorb light. Let us, now, look at the opposite effect: how a crystal can emit light. There are, basically, two processes: luminescence, where the light is absorbed and then emitted (involving real states) and inelastic light-scattering, where the light is absorbed and scattered away at the same time (involving virtual states, as in the Raman, Brillouin, etc. effects). We will focus on the first case.

When an electronic excited-state is filled because of some kind of energy transfer (optical/photoluminescence PL, thermal/thermoluminescence TL, etc...), after some time, it will relax to the ground-state, via two different kind of channels: radiative and non-radiative. In the first case, we have again the creation of a photon from an electron-hole recombination, while, in the second, we have a sequence of anelastic collisions with phonons in order to reach the thermal equilibrium.

At thermal equilibrium, the carrier population decreases exponentially with the energy and, therefore, the lower energy the state has, the stronger emission it gives: luminescence is, thus, a sensitive probe of low-lying energy levels, and it can be represented in a three-step-process (excitation-thermalization-recombination). The visible emission produced by a thermalized body at room temperature is very small, so that the most part of the experiments have to be carried out in a non-equilibrium condition. One possibility to make this, is to excite the medium with light, as shown in §6.1, reaching a non-equilibrium distribution of electron-hole pairs (I step: excitation). In most cases, these pairs will thermalize among themselves and reach the "quasi-thermal" equilibrium in a time shorter than the recombination time (II step: thermalization). Here we emphasize that "quasi-thermal" means that the

Fermi sea is in a thermal equilibrium, but the whole system (charge carrier and lattice) does not. Finally we have the recombination, and spontaneous emission of light (III step: recombination).

Since luminescence is produced by thermalized pairs, the emitted photons are not correlated with the excitation process: the energy of the emitted photons depends only on the band structure and energy levels of the material. Since the pairs accumulates in conduction and valence bands extrema before recombination, the emission is quite strong in direct band-gap materials (as GaAs, $\tau \sim 2.8\,\mu$s), where the electric dipole transitions are allowed, and it is much lower in indirect band-gap materials (as Si, $\tau \sim 4.6\,$h, and Ge, $\tau \sim 0.6\,$s), where they can recombine radiatively only via phonon-assisted transitions.

Indirect emission can be increased by means of the pairs localization, as happens in GaP or in Si nano-crystals, because, in this case, the k-vector is undetermined.

Let us define the radiative recombination time τ_r: if the free-electron and hole concentrations are n_e and n_h, the emission rate is, then, $n_e n_h/\tau_r$ (assumed that τ_r is the same for all possible choices of recombining pairs), otherwise we have to use its average value $\langle\tau_r\rangle$. For a thermalized pair distribution, τ_r depends on the electron and hole energies, so it changes with the photon energy. In photoluminescence experiments, we always excite an equal number of electrons and holes ($n \equiv n_e = n_h$), so that the radiative recombination rate for a single photoexcited charge carrier is

$$\frac{1}{\tau_{rad}} = \frac{n}{\langle\tau_r\rangle} \quad .$$

The total decay rate is, then, the sum of the radiative and the non-radiative terms:

$$\frac{1}{\tau_{tot}} = \frac{1}{\tau_{rad}} + \frac{1}{\tau_{nonrad}} \quad .$$

6.2.1 Band-to-Band Transitions.

Let us now calculate the photoemission line-shape, in case of a direct band-gap. The photo-emitted spectral intensity $I(\hbar\omega)$ is proportional to the population of charge carriers, i.e. the product between the joint-density of states and the Fermi function.

The joint-density of states for conduction (c) and valence (v) bands is defined as

$$D_j(E_c - E_v) = \frac{1}{4\pi^3} \int \frac{dS_k}{|\nabla_k (E_c - E_v)|} \quad , \tag{6.17}$$

where S_k is the surface on which $E_c - E_v = const.$ Taking the difference $E_c - E_v$ near the band-gap E_g we can expand it in power series, and stop at the second order term $E_c - E_v = E_g + \left(\hbar^2/2\mu\right) k^2$, where μ is the reduced mass of electron-hole pair. Thus, Eq. 6.17 becomes

$$D_j(E_c - E_v) = \begin{cases} \left[\sqrt{2\mu^3}/\left(\pi^2\hbar^3\right)\right](E_c - E_v - E_g)^{\frac{1}{2}} & \text{for } E_c - E_v > E_g \\ 0 & \text{for } E_c - E_v < E_g \end{cases} \quad ,$$

Since, for low photo-excitation density, the electron and hole Fermi function f_e and f_h can be approximated with the Boltzmann distribution, we obtain the emission

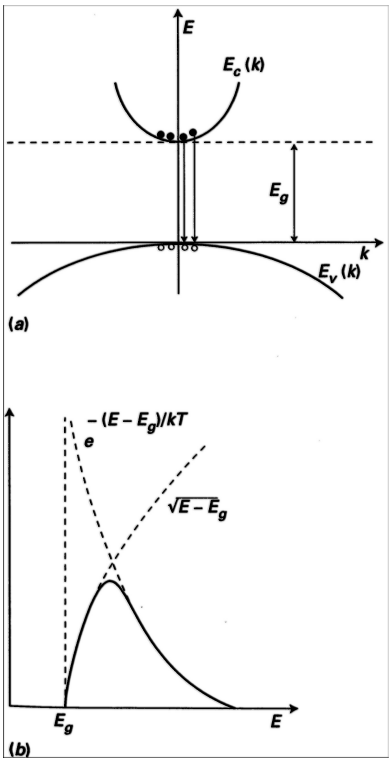

Figure 6.4: Luminescence transitions and lineshape [32].

spectral shape

$$I(\hbar\omega) \propto (\hbar\omega - E_g)^{\frac{1}{2}} \exp\left[-\hbar\omega/k_B T\right] \quad , \tag{6.18}$$

where $\hbar\omega = E_c - E_v$ is the emitted photon energy, as shown in Fig 6.4.

For higher excitation beam intensity, the electron-electron and hole-hole interaction may be stronger than the electron-phonon or hole-phonon interaction, so that the carrier temperature is higher than the lattice one. Photoluminescence is, thus, a way to directly measure the carrier temperature.

The temperature dependence of the lifetime τ_r of a free-carrier for a direct band-to-band recombination can be inferred from

$$\tau_r = \frac{1}{2\sigma n_i v},$$

where n_i is the intrinsic free-carrier density, σ is the direct recombination cross-section and v is the electronic speed. The last two quantities depends on temperature. At high temperatures, the measured lifetimes are often found to approach this value, while at lower temperatures, a free-to-bound recombination may be dominant. In general, impure insulators and wide band-gap semiconductors at room temperature will be characterized by a carrier lifetime which is limited predominantly by free-to-bound or bound-to-bound transitions. This should not be surprising since, in band-to-band recombinations, a considerable momentum transfer as well as energy

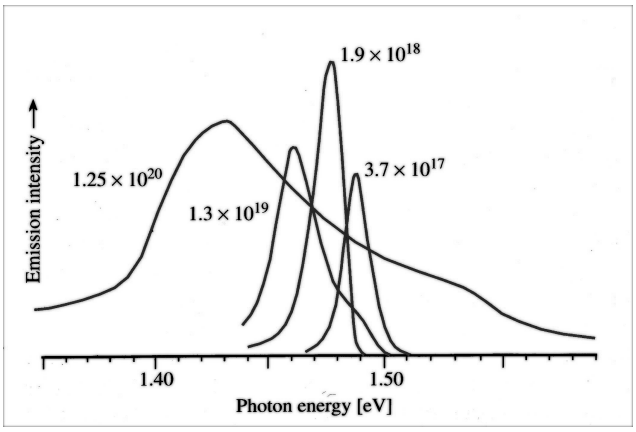

Figure 6.5: Emission lineshapes changing with doping [33].

transfer is usually taking place. Free electrons and holes have, thus, to meet each other with opposite velocities, in order to conserve the momentum.

6.2.2 Free-to-Bound Transitions.

At low-temperatures, some carriers are frozen on impurities, so that it is possible to have a recombination between a band and a bound state. In this case $\hbar\omega_{peak} = E_g - E_A$, where E_A is the binding energy of the impurity-site, so that this kind of emission is a good way of directly measuring the impurity binding energy.

In Fig 6.5, several emission spectra are shown for various doping concentrations in p-GaAs. Starting from the lower concentrations of acceptors $N_A = 3.7 \times 10^{17} \div 1.9 \times 10^{18}$, which can be assigned to free-to-bound transition, we have many features by changing the doping: broadening, changing of the line-shape and redshift. The spectra broaden because, as the acceptors become closer to each other, their wave-functions overlap, forming an impurity band. When the band is so broad that it overlaps the valence band, holes are no longer localized and become free-carrier. This is called Mott transition[2]. The shape for higher doping concentrations deviates from the Boltzmann form, to reach the Fermi-Dirac one: this is due to the spin degeneration. Finally the redshift is due to a many-body effect, called "band-gap renormalization", but here we will not face this subject.

The free-to-bound radiative recombination rate, as calculated by Dumke [40], is

$$\frac{1}{\tau_{eA}} = \frac{64\sqrt{2}\pi n_r e^2 \hbar^2 \omega}{c^3 m^2 \sqrt{(m_h E_A)^3}} |P_{cv}|^2 N_A \ , \tag{6.19}$$

where m_h is the averaged hole mass and P_{cv} is the averaged electron-momentum matrix element, between conduction and valence bands. For instance, GaAs with $N_A \sim 10^{18}$ acceptors per cubic centimeter have a lifetime of about 2 ns, comparable with the band-to-band lifetimes.

[2] A Mott transition can, actually, take place before the ovelapping too, because of spin degeneration.

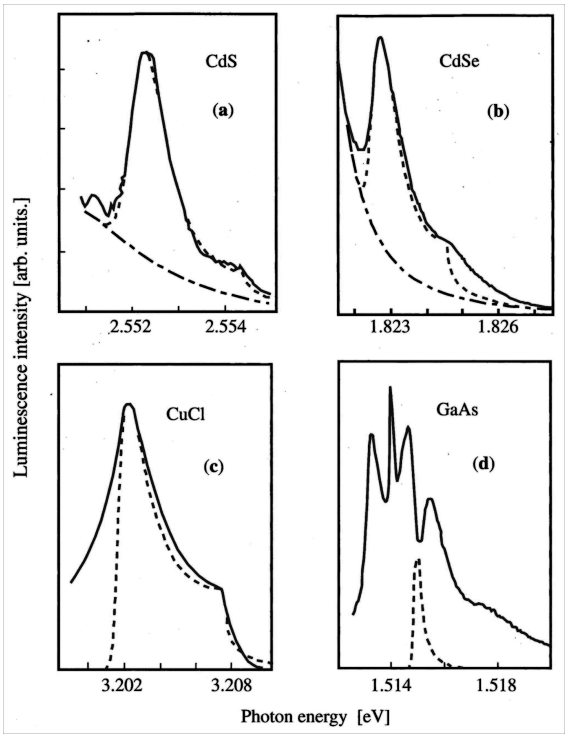

Figure 6.6: Free excitons emission spectra, asymmetrical lineshape [33].

6.2.3 Excitons and Bound-Excitons.

At low-temperatures, photoexcited electrons and holes form excitons, and the emission spectra are dominated by their radiative annihilation, producing a "free-exciton peak". But there is the possibility to have bounded excitons too, near some neutral impurity, attracted by Van der Waals forces, since this attraction lowers the exciton energy.

6.2.4 Free-Exciton Emission.

As we saw in §6.1.6, we should refer to exciton-polaritons rather than excitons, but, in order to better understand the importance of the polaritons approach, let us neglect this effect for the moment.

In this case, we have a simple radiative decay of excitons into photons. By the momentum conservation law, only $k \simeq 0$ excitons can be converted into photons. This leads to a delta function or, taking into account the finite exciton lifetime, a Lorentzian line-shape. But the observed free-exciton spectra always have an asymmetric line-shape, quite different from a Lorentzian, plus a shoulder for higher energies, as shown in Fig 6.6.

In the polariton approach [41], external photons are converted inside the medium into exciton-polaritons which can relax towards lower energies by means of the scattering with phonons via their exciton-component, since the photon-term has a

very weak interaction with phonons. Some polaritons will be back-scattered and will emerge from the sample as luminescence photons.

In order to understand experimental spectra, we have to refer to the polariton dispersion curve in Fig 6.3. In the lower polariton curve there are not energy minima, where thermalized particles are usually accumulated, so that, in principle, there should not be a peak in the spectrum.

Actually, polaritons do not accumulate near an energy minimum, but near the group-velocity ($d\omega/dk$) minimum, which is located in the transverse-exciton energy $E_T = \hbar\omega_T$, called "bottle-neck". Lower polaritons which are above the bottle-neck have a large exciton-component. They rapidly relax towards lower energies, since their interaction with phonons is very strong. Lower polaritons which are below the bottleneck have short lifetime too, because of their high group-velocity, so they can escape easily from the sample as photons.

For these reasons, we observe a peak of the lower polaritons distribution function near the bottle-neck energy E_T.

Besides the distribution function, we need also the transmission coefficient in the sample surface, in order to know how many polaritons will be transmitted or reflected back inside the medium. Unfortunately this coefficient cannot be computed from Maxwell boundary conditions as usual. One needs to introduce some Additional Boundary Conditions (ABCs), in order to describe the behaviour of excitons near the sample surface.

The ABCs choice is a quite complex problem, and, perhaps, it depends on the sample surface details. Nevertheless, the large peak at E_T is not so sensitive to the ABCs, while the shoulder at higher energies is very sensitive to them. It is possible to show that the shoulder is due to a change in the transmission coefficient near the longitudinal exciton energy $E_L = \hbar\omega_L$, corresponding to the growth of the upper polariton.

The agreement between experimental data and theoretical calculation (dashed curves) in Fig 6.6 is quite good in three of four samples, providing the addition of a background, probably due to defects scattering. In GaAs, the behaviour is completely different from what expected: there is a dip at $\hbar\omega_T$ because there the group-velocity have a minimum, so that the scattering process from impurities is more probable. The dip disappears in very high quality pure samples.

6.2.5 Bound-Exciton Emission.

In the emission spectra of many semiconductors, it is possible to see very sharp peaks, due to bound-excitons recombinations. An exciton can be bound to a donor (D) or an acceptor (A) in their neutral state at low temperature, resulting in the complexes (D^0X) and (A^0X) respectively. These complexes can be regarded as an hydrogen molecule H_2 with an hole placed instead of a proton. Since the hole effective mass is smaller than the proton mass, the complex binding energy will be smaller than the H_2 one.

Is possible to show that the bound-exciton binding energy, in unit of the binding

energy of a free-exciton, depends on the ratio

$$r = \frac{m_h^*}{m_e^*}$$

for (D^0X) and on $1/r$ for (A^0X), where $m_{e,h}^*$ are the effective masses of electron and hole. In general the bound-exciton binding energy decreases as r decreases[3].

Excitons can also bind to ionized impurities, forming (D^+X) and (A^-X) complexes. In principle, one can regard the complex (D^+X), for instance, as a hole bound to a neutral donor (giving the electron of the $e-h$ pair entirely to the donor, and, thus, forming a (D^0h) complex), but it is not so, because the binding energy for the (D^+X) complex is bigger than the (D^0h) one.

Since the complex (D^+X) is not stable for $r < 1.4$ (or (A^-X) is not stable for $1/r < 1.4$) it follows that, in a given material, excitons can bind either to ionized donors or acceptors, but not with both.

Infrared illumination is usually an helpful tool in order to enhance the ions density and to measure this kind of bound-excitons recombinations.

Finally, there is the possibility to have (D^0e) or (A^0h) complexes too (or D^- and A^+ respectively), but, in this case, the binding energy is very small. To have an idea, just think that D^- is similar, for instance, to the H^- ion where the extra-electron has a binding energy of 0.75 eV only, and for D^- it is even smaller. However D^- peak is, actually, observed, for instance, in n-doped Si.

[3] All proofs, omitted in this section, can be found in ref [39].

Chapter 7

Main features of strontium titanate.

The perovskites are a family of crystals made of three different chemical elements, which are, in general, denoted by A, B, X. Their chemical general formula is ABX_3.

Such crystals have a cubic unit-cell, where A-atoms (Ba, Ca, Y ...) are surrounded by twelve X-atoms and B-atoms (Cu, Ti, Tl ...) are surrounded by six X-atoms, as show in Fig 7.1. In most cases, they are oxides, i.e. X is an oxygen. Some examples of perovskites are $BaSnO_3$, $SrZrO_3$, $SrTiO_3$.

The crystal structure of perovskites can be significantly deformed, and change its macroscopic features, by means of slight changes in the relevant parameters, as temperature, pressure or doping. The extent of these changes depends mainly on the size of the A-atom, which is into an empty space between the eight octahedral cages made by the oxygens: the bigger A-atom, the smaller lattice deformations.

These crystals have a great scientific interest in applications as well as in the fundamental research: they play an important role in the fields of corrosion, friction and lubrication, but, above all, they completely change their electric and optical behaviour even if very small changes in their chemical composition are made. For instance, they can be opaque or transparent and they can present an insulator phase, as well as a superconductor phase, as shown previously for cuprates, which are, as mentioned, a particular class of perovskites.

In the following, we will give some informations, in open order, on the physics of the perovskite crystal which is the subject of the second part of this work, the strontium titanate $SrTiO_3$ or STO.

7.1 General properties.

The principal features of the strontium titanate descend from its very high polarizability.

A cubic-to-tetragonal transition in the STO lattice structure is found at 105K$\div$110K by means of several different kind of measurements [50] [51] [52]. STO is a paraelectric material until very low temperatures. An incipient ferroelectric state is prevented by the quantum fluctuations for $T < 10$K [44]. As a result, its dielectric

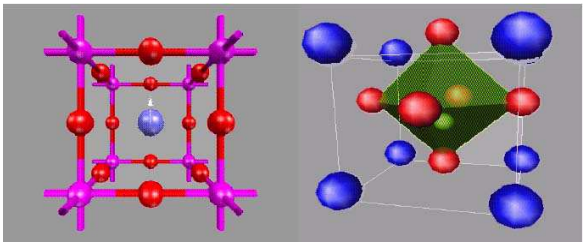

Figure 7.1: Perovskite unit-cell.

constant increases as the temperature decreases, following a modified Curie law, $\varepsilon \approx C/T^{\gamma}$, and reaching very high values. For instance, at 4K its value is about 5000 [45], or even very much higher [54], while between 0.3K and 4K it was found to be almost temperature independent. Its room temperature value is about 300. Such a high dielectric constant is one of the main features of this compound.

This feature is usually attributed to the presence of the T_{1u} (or TO) type soft-mode [55]. Since the Ti-atom has a small radius, it is weakly boxed into the octahedral oxygen cages, leading, thus, to the presence of this odd and soft phonon mode. However, a simple harmonic (or even enharmonic) description of this soft-mode seems to be quite inadequate to explain such a quantum-para-electricity [56].

In 1964, Kahn and Leyendecker [48], whose results were experimentally supported by Cardona in 1965 [70], calculated the electronic energy bands within the tight-binding approximation. From this assumption, the empty conduction band is derived predominantly from the titanium $3d$-orbitals and the filled valence band mainly from oxygen $2p$-orbitals. The lowest energy conduction band was predicted to form six ellipsoidal equi-energy surfaces at the BZ boundaries in the (100) direction. Such many-valley structure is confirmed also by the magneto-resistance measurements [49].

The symmetry of the conduction band is due mainly to the Ti $3d$ T_{2g} and E_g bands, followed by the bands of Sr $4d$ T_{2g} and E_g states. Free-electron-like bands dominate at energies from 15 eV above the valence band maximum on.

The upper valence band consists of 18 electrons in dominantly O-$2p$ states, hybridized with Ti and Sr states, and it has a bandwidth of about 5 eV. The lower valence band consists of 12 electrons in Sr-$4p$ and O-$2s$ states, which are separated by 2 eV, and the bandwidth is about 5 eV. Some shallow core-levels are found to be related to the Sr-$4s$ and Ti-$3p$ states [63].

7.2 Transport properties and elementary excitations.

STO is an insulator, with a direct absorption edge of about 3.75 eV and an indirect energy-gap of about 3.27 eV [69]. Nevertheless, n-doped samples of various kinds present a very small resistivity between 4K and room temperature (about $10^{-1} \div 10^{-3}$ Ω cm) [47]. The electrical transport properties of STO were first investigated by Frederiske and coworkers in 1964, who measured the conductivity and the Hall and Seebeck coefficient of a conductive samples. The Hall mobility (Fig 7.2) was found

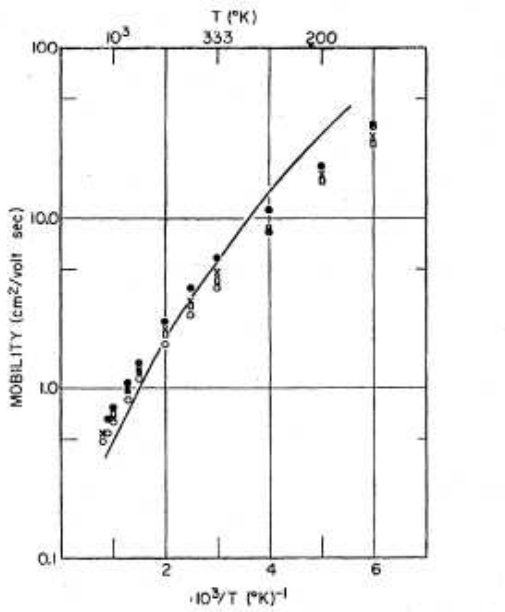

Figure 7.2: Hall mobility of STO [46].

to be 7 cm^2/volt·sec at room temperature and to reach values as large as 5×10^3 $cm^2V^{-1}s^{-1}$ at 10K [46]. Doped samples were even found to be superconductive [62].

While an n-doping is quite simple to be achieved (by means, for instance, of the oxygen vacancies creation, or $Nb^{5+} \rightarrow Ti^{4+}$, $La^{3+} \rightarrow Sr^{2+}$ substitutions), the p-doping is harder to be done, even if some progresses in that sense were made [61]. Actually, many works seem to demonstrate that the holes (or, better, hole-polarons) are easily self-trapped, also in a perfect lattice structure [60].

The charge carrier mobility is one of the most debated subjects. According to the Hall measurements, the electron effective mass m^* in STO is about ten times the free-electron one m_e, suggesting that electrons are highly mobile large polarons [64], while optical absorption data are described using a small polaron picture [72]. Holes are expected to be localized near the oxygens [65]. Moreover, the effective mass increases from $6m_e$ to $16m_e$ between $77K$ and 300K [46]. Nowadays, although it is quite accepted that charge carriers have a strong polaron nature [66], and many unusual properties can be explained in the framework of the so-called "mixed-polaron theory" [71], the discussion on this subject is still open. In the mixed-polaron theory, in which the lowest energy state of the charge carriers is a superposition of a comparable number of large and nearly small polarons, the transport mass of the mixed-polarons is determined by a weighted average of the reciprocal masses of the two types of polaron. It is, thus, dominated by the lighter component, while the temperature dependence of the effective mass arises because the proportion of nearly small polaron states in the carrier wave-functions increases with temperature.

It was found that the electronic properties of this compound present a lot of new and interesting aspects. For instance, in such an highly polarizable compound, there are many nonlinear unharmonicities, due to the strong vibrionic interaction, and, hence, some new polaron-like excitons are found to be likely to exist in the material. An example is given by the so-called charge-transfer vibrionic exciton (CTVE) [58], [59]. CTVE is a spatially well-correlated pair of electron and hole polarons or "bipolaron". The main driving force of its formation is the charge transfer between the oxygen and the titanium atoms. The lattice deformations which are caused by this charge transfer create a new minimum in the lattice potential, while the ground-state remains stable with respect to the charge transfer lattice effects. The reduction of the potential energy in the CTVE state due to the lattice relaxation can lead to the CTVE self-trapping. The main experimental evidence of the CTVE manifestation can be obtained from optical measurements rather than transport ones, since, of course, the CTVE is not conductive. But the probably most surprising discovery in this field was the creation of a conducting quasi-two-dimensional electron gas at the interface between STO and another dielectric perovskite insulator, $LaAlO_3$ or LAO [67]. The electrons at this interface were found to be highly mobile (more than 10^4 $\mathrm{cm^2V^{-1}s^{-1}}$ at 4.2K) and their density is order of magnitude higher than a semiconductor-interface electron-gas. Moreover, this interface can be dynamically tuned across a metal-insulator transition by applying an external gate-field . The result is a system which can be easily switched from highly insulating to highly conducting for a wide range of possible devices and applications, as, for instance, an "high electron mobility transistor" (HEMT).

7.3 Optical properties.

Recently, a prominent enhancement of ε has been observed under ultraviolet light irradiation [53], leading many researchers to use the word "giant" to describe it.

It was also pointed out that this enhancement remains only during the illumination, and disappears as the UV-light is switched off. Thus, one can think that this is a kind of photoinduced phase-transition, and it is expected to come from the coupling between the photo-excited electrons and the soft-phonons modes. An UV-photon excites a valence band electron to the conduction band, in which its interaction with phonons leads to a polaron. Since the conduction band is mainly composed by the titanium $3d$-orbitals, the excited electron could find in the Ti-oscillations (having the T_{1u}-symmetry) its "natural" coupling partner. But, for symmetry reasons, the coupling between them is allowed only at the second order. At the first order, i.e. through the ordinary electron-phonon interaction, instead, it can couple with the A_{1g} mode of O^{2-}-ions. This results in the formation of two distinct kinds of polarons: the super-para-electric (SPE) large polaron and a strongly localized self-trapped polaron. In the SPE state, the quadratic electron-phonon coupling results in the phonon-softening of T_{1u}-mode. This phonon-softening is supposed to cause a giant enhancement of the static dielectric constant [57].

In the next section, we will focus on the wide range of photoluminescence studies available on this material, since this is the subject of the present work too.

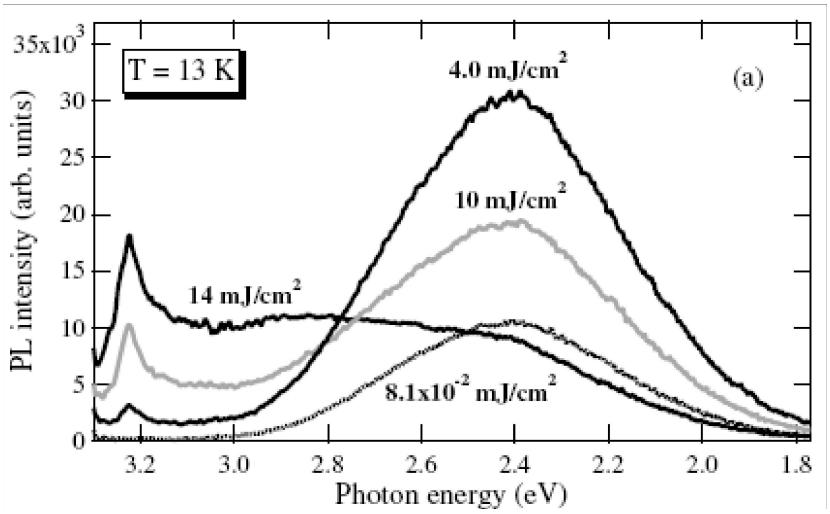

Figure 7.3: The behaiviour of NBE, A and B bands with laser-intensity [79].

7.3.1 Previous photoluminescence studies on STO.

The pioneer paper on the STO photoluminescence (PL) is the work of L. Grabner, in 1968 [73]. He found a near-infrared narrow band at 1.6 eV and a broad "green" low-temperature (4K) luminescent band at 2.4 eV (about 500 nm), whose lifetime was found to be 5×10^{-3} s. These PL bands have a considerable Stokes shift. The author found to be unlikely that such emission band could come from extrinsic impurities. Subsequently, authors of ref [74] proposed to attribute it to an exciton self-trapping. These idea was supported by other works too. This band was assumed to be of excitonic origin, since it was observed in many compound containing titanate octahedra and it was found to be not related with any particular impurity. Time-resolved measurements [75] showed that both unimolecular and bimolecular processes were involved: electrons form small polarons, while the holes interact with them to form a Self-Trapped Exciton (STE), either immediately or after being trapped for a certain time by impurities or defects. Also PL-studies on STO nano-particles were supposed to confirm the STE origin of the green band. In a more recent paper [77], electron beam luminescence from bulk STO was studied, and the green band is, on the contrary, attributed to some defect-trapped polarons (although these defects were supposed to be intrinsic), and another blue band, peaked at 2.8 eV, whose intensity was found to increase in the range 80K÷300K, was attributed to the charge transfer vibrionic exciton (CTVE, §7.2). In this picture, the photoinduced carriers are small polarons. The phonon interaction can overcome the potential barrier between electron and hole polaron, in order to reach a CTVE state. The temperature dependence of the PL intensity seems to confirm the CTVE origin of this band.

A very complete and detailed study on these bands and their features, can be found in refs [78], [79] and [80]. In those papers, Mochizuki and co-workers clarified that the 2.4 eV band (B-band in the notation of that paper) is due to excitons

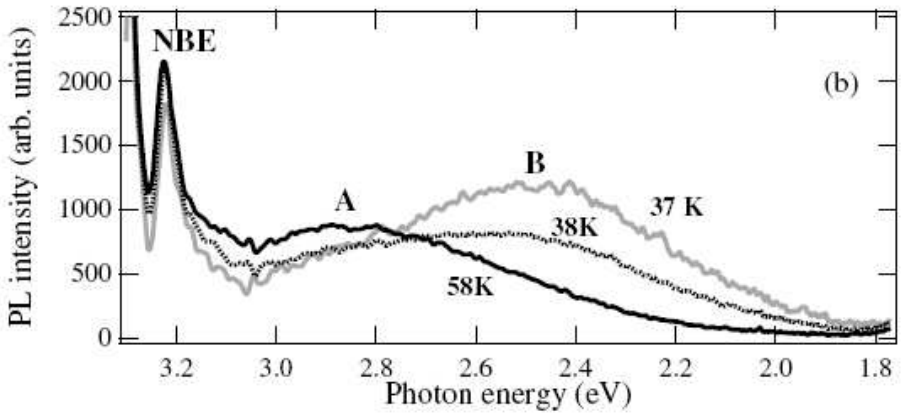

Figure 7.4: The behaiviour of NBE, A and B bands with temperature [79].

trapped near oxygen-defects, and not to a self-trapped exciton. Their fundamental observation was that the green band grows under a 325 nm laser-line irradiation in vacuum, while it disappears in oxygen atmosphere under the same irradiation. The band is, thus, closely related to the oxygen defects creation under the irradiation. The same does not happen when 355 nm laser-line is used. Moreover, they found two other bands: a near-band-edge (NBE) band at 3.2 eV and a blue band (A-band) at 2.9 eV. These two bands were found to have a different nature with respect to the green band. First of all, if the laser flux increases, the B-band saturates, while the A and the NBE bands continue to grow (Fig 7.3). Secondly, the B-band disappears as the temperature rises to the room temperature, while the NBE band become weaker and broader, but still visible, and the A-band remains clear even at room temperature (Fig 7.4). Finally, the B-band has a long lifetime (≥ 1 ms), while both the NBE and A bands have short lifetimes ($\ll 50$ ns). Their room temperature spectral structures are hardly changed by changing the excitation wavelength from 325 to 355 nm. The authors suggest that the NBE and A bands have the same origin and arise from same kind of phonon-assisted or intrinsic-defect-assisted electron-hole recombination. The NBE-band is assigned to one of the optical phonon-lines, while the A-band, since it displays an almost smooth and continuous shape, is assigned to the creation of many transverse and longitudinal acoustic phonons, beside the optical ones. Another tentative explanation for NBE and A bands is a defect-induced resonant Raman scattering, although other possible explanations are not excluded by the authors.

Recently, the interest in the field of STO photoluminescence was renewed by the works of Kan and colleagues [82], [83], also highlighted in ref [81]. In those works, it was showed that creating oxygen vacancies turns on a new radiative pathway, giving a blue light emission at room temperature. Moreover, since the oxygen vacancies can be created also by means of Ar^+-ion bombardment, the photoluminescent region can be patterned into any size and shape, using the conventional photolithography: this possibility opens the route to a wide range of possible applications. The authors

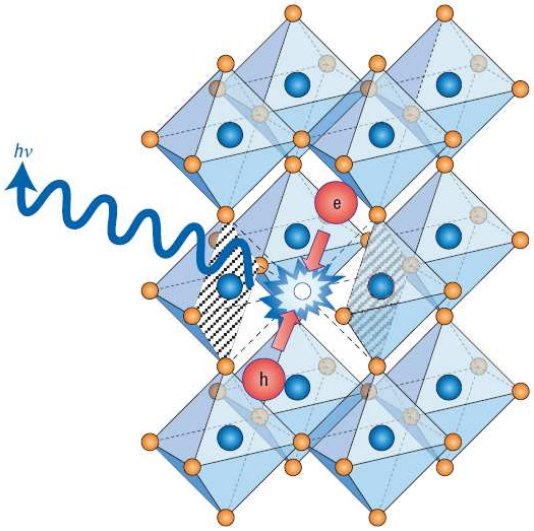

Figure 7.5: An illustration of the oxygen-vacancy assisted e-h recombination [81].

propose that the oxygen vacancy creates a defect-site where an electron and a hole can recombine, to generate a radiative event, as depicted in Fig 7.5. Let us describe, briefly, the first work. The He-Cd laser line at 325 nm was used, and a 430 nm (2.9 eV) PL-band is observed in Ar^+-irradiated samples. The PL intensity increases as the Ar^+-irradiation time increases, and saturates after about ten minutes. The non-irradiated sample was found to show no emission (Fig 7.6 a). In the same irradiation time range, the sample was found to become conductive. This is an indication that the ion irradiation creates oxygen vacancies. In order to prove that these vacancies are responsible for the PL emission, oxygen deficient STO thin films were studied, and a linear behaviour of the integrated PL intensity versus the film thickness was found (inset of Fig 7.6 b). The authors assert that this is a proof of the oxygen vacancy involvement, but they do not explain why the interception value for a zero-nm thick film is not consistent to zero. Besides the blue band, the authors found the green and the near-the-band-edge bands, having the same temperature dependence of the bands seen by Mochizuki. In this work, however, the NBE band is seen only for oxygen deficient samples for low-intensity photo-excitation, while it is present in stoichiometric samples too for intense photo-excitation. This result is in partial agreement with the one of Mochizuki, since, in that work, the blue band was found to follow the same NBE-band behaviour with the excitation intensity.

Finally, in the second work, Kan and coworkers found the same spectral features in La and Nb doped samples, concluding that the PL emission is strongly connected to the presence of conduction electron, and not with the defect type.

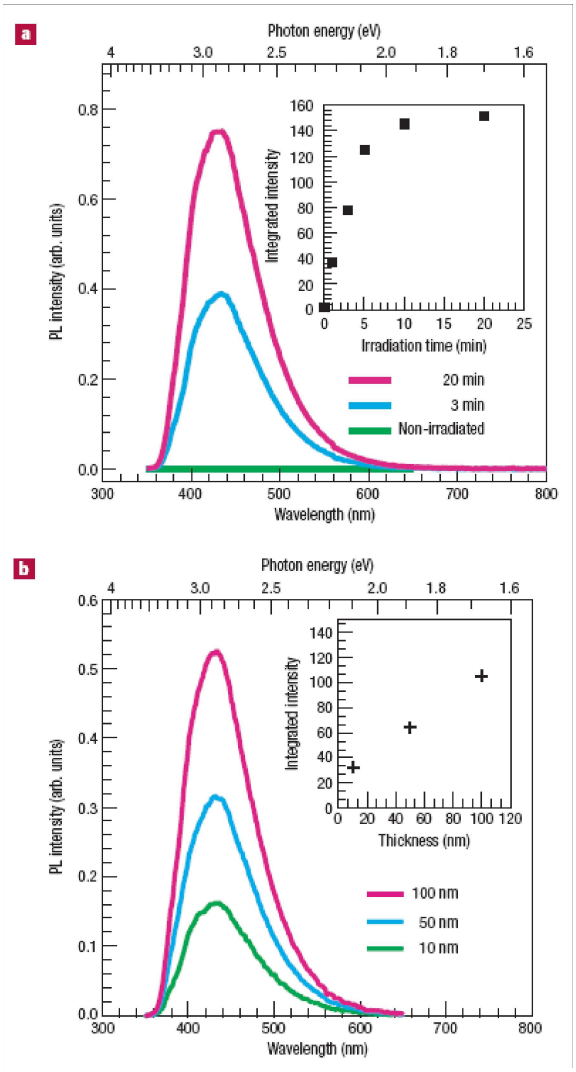

Figure 7.6: PL spectra at different irradiation times (a) and film thickness (b) [82].

Chapter 8

Results and discussion.

In this Chapter, the PL experimental setup is described in quite detail and the main experimental problems are faced. The principal experimental results are described within a bimolecular-unimolecular kinetic model, and some other possible models are ruled out, with the help of an accurate best-fit procedure. This procedure, here called "Global fit", is described in detail, and the full Matlab program is enclosed in App. D. A tentative model of the underlying microscopic recombination mechanism is given in the last section.

8.1 Description of the experiment.

The photoluminescence (PL) experimental setup is shown in Fig 8.1. Our UV-light source is the third harmonic of a mode-locked Nd:YAG laser, whose wavelength is 355 nm, which corresponds to a photon energy of about 3.49 eV. This value is well above the STO indirect band-gap (3.26 eV) and just above its direct transition edge (3.46 eV). Its repetition rate is 10 Hz and its pulse duration is about 25 ps (full width at half maximum). The UV-beam is slightly focused on the sample surface by means of a 20 cm lens (L) and the spot size on the sample was directly measured to be 1.2 ± 0.1 mm (radius at $1/e^2$ of the maximum). The UV scattered light is blocked by a long-pass filter (cutoff wavelength of 375 nm), not shown in the figure. The emitted light is then collected by a lens system (LS) made of three lenses which reproduces the image of the illuminated sample on the detector's head. The setup is designed to make both time-resolved or spectral resolved measurements. In the former kind of measurement, the PL intensity is recorded as a function of time with the help of a very fast oscilloscope, while, in the latter, the same PL signal is measured at different wavelengths by using a monochromator-photomultiplier series. Let us describe in detail the experimental instruments we used for these two kind of measurements.

Time-decay curves are measured by means of a fast photodiode (PH), whose rise-time is about 150 ps. The signal is, thus, spectrally integrated with the spectral efficiency of the photodiode. The electric signal is then recorded by a 20 Gsample/s digital oscilloscope (DO), which has an analog bandwidth of 5 GHz. The response function of the revelation instruments is measured by sending in the revelation

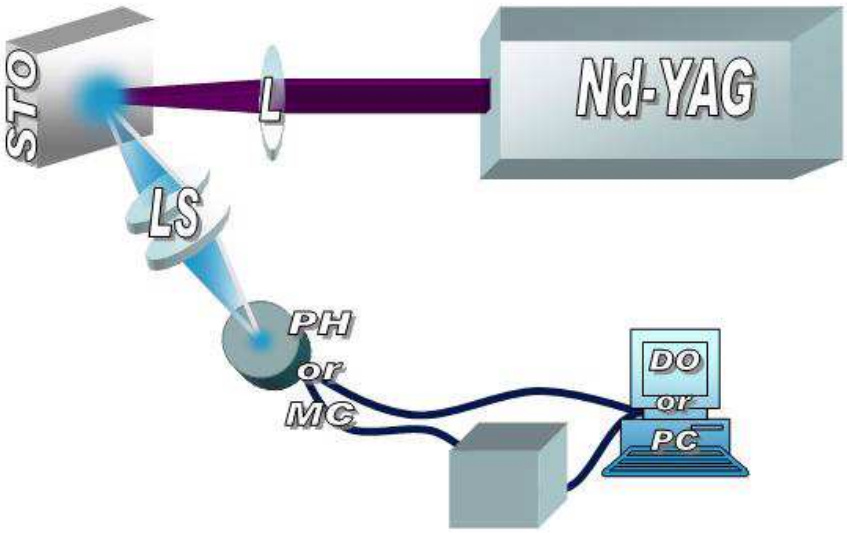

Figure 8.1: PL experimental setup. L is a lens, LS is a lens system, PH is a fast photodiode, MC is a monochromator, DO is a digital oscilloscope and PC is a personal computer.

lens system the UV residual scattered light. Since the pulse duration is very short compared to the PH rise-time, the resulting curve is a very good approximation of the instrumental response function. Moreover, since the pump frequency is not far from the measured luminescence band peak and the investigated frequency range corresponds to an almost flat zone of the PH spectral efficiency curve, we exclude that the UV response function is different from the one in the visible domain. To reinforce this statement, a response function was measured by means of the second harmonic line of the Nd:YAG laser (532 nm), which is almost in the middle of the STO PL-spectrum, and we found that 355 and 532 nm response functions present only negligible discrepancies. A new response function and dark-current signal were recorded before each measurement.

Frequency resolved curves are measured by means of a photomultiplier (Hamamatsu mod. R928, $185 \div 900$ nm) and a monochromator (MC), whose spectral resolution limit is 0.1 nm. However, the spectral resolution we chose, in order to have a reasonable (~ 40 min) time of measurement, is 1 nm. The electric signal is then time-integrated by a gated integrator (Stanford, mod. SR250) and recorded on a personal computer. The photomultiplier time-response is very much slower than the photodiode one (several nanoseconds) and the time windows of the gated integrator was set to about 50 ns.

Time and frequency resolved curves were recorded as a function of the pump-pulse intensity and as a function of the sample temperature. The former was mea-

sured with a large head power meter (Ophir, mod. PE9) and adjusted by using a set of neutral filters. The latter was controlled by a thermal controlled stage (Instec, mod. HCS600V). The sample temperature can, thus, be varied in the range $-190 \div 600$ °C with accuracy ± 0.1 °C. The final spectrum is corrected with the detection instruments spectral efficiencies. All measurements, both in the time or frequency domain, are taken in air and were found to be reproducible. No visible damage was seen on the sample surface at the end of each measure session.

8.1.1 Samples.

We investigated several STO samples, all having (1 0 0) orientation, here called "I" (intrinsic), "Nb" (niobium doped) and "O" (oxygen deficient). I samples are six nominally pure, transparent , stoichiometric, $5 \times 5 \times 1$ mm^3 samples from four different companies (Surface Net, Escete, Crystal, Crystec). All I samples have nominal impurity concentration below 150 ppm. Nb samples are four commercial Nb-doped, dark blue samples (all supplied by Crystal) with 0.2% mol Nb concentration. Finally O samples are four annealed dark blue samples. They were obtained from pure samples, of the same kind of I samples, by annealing for 1 h at 950 °C and 10^{-9} mbar (base pressure 10^{-11} mbar).

8.2 Experimental results: time domain.

In this section we will expound our main experimental result: the presence of a mixed kinetics in the PL emission decay. Besides this, the PL emission behaviour with temperature can add other interesting informations about the nature of the underlying recombination mechanism which is responsible for the photoluminescent band under investigation.

8.2.1 Time-resolved decays.

In Fig 8.2 the normalized time-resolved decay curves of I, Nb and O samples are shown in a semilogarithmic vertical scale. Some preliminary considerations can be done.

First of all, although we did not perform an absolute quantum yield measurement, it is clear that non-radiative processes are dominant, since the photoluminescence, as seen with naked eyes, is weak compared to the very high pump intensity.

Since the experimental conditions are the same in each measurement session, the relative yield can be measured from the integral of the decay curves in time. It was found that all samples of the same kind have a roughly comparable fluorescence yield. The maximum sample-to-sample variation is found in I samples and it is within the 80%, while the initial emission intensity is even more stable (30%). The Nb and O samples yield is found to be slightly lower, but the not negligible absorption of doped samples in the visible range could account for this feature.

The overall dynamics is very similar in each kind of sample, indicating that the doping plays a minor role in the kinetics too, and some minor differences can be found only in the values of the best fit parameters, as shown in the following. Background

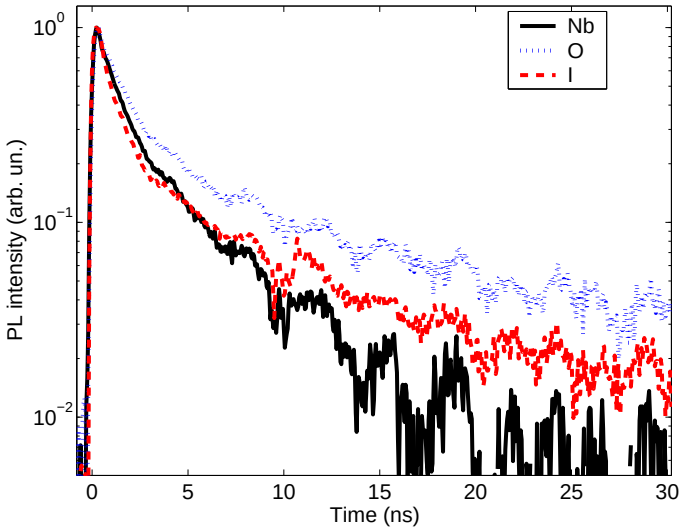

Figure 8.2: Time-resolved normalized decay curves of I (red dashed line), Nb (black solid line) and O (blue dotted line) samples in a semilogarithmic vertical scale.

oscillations and other minor features are due to the instrumental response function and it will be taken into account by the best fit procedure.

The PL emission is very fast: it has almost vanished after $25 - 30$ ns in all samples. These values are in agreement with the upper limit value (50 ns), which is reported in ref [79]. On a deeper look, it should be noted that the decay is not a simple exponential one. It is possible to use several exponential functions, and we found that the minimum number of different functions, in order to obtain a reasonable best-fit curve, is three. The last qualitative consideration is that STO has a quite high damage threshold. In our experiment, the maximum pump-pulse energy is 2 mJ, which means a maximum spot center flux of about 90 mJ/cm^2.

Since at a wavelength of 355 nm the optical penetration depth is about 1 μm and the reflectance is about 25% [69], the estimated peak energy density absorbed in the material surface layer is 600 J/cm^3. Even at the highest pump-pulse intensity, no photoinduced damages are seen on the sample surface of pure as well as doped samples. All measurements were repeated increasing and decreasing the pump intensity, in order to find the presence of possible irreversible signal variations, but all measurements were found to be perfectly reproducible.

The most remarkable feature of those decay curves is shown in Fig 8.3. The experimental time-constant τ_{exp} is defined here as the full width at half maximum of the decay curve. This empirical lifetime was found to decrease as the excitation pulse energy increases, i.e. as the photoinduced carrier density increases. As a consequence, the intrinsic bandwidth of a possible emitting device, calculated as the inverse of τ_{exp}, can increase to a value as high as ~ 2 GHz. There are several recombination mechanisms which can lead to a carrier density dependent characteristic lifetime. In particular the bimolecular recombination and the Auger effect could lead to this result. In the next section, some possible kinetic models will be tested,

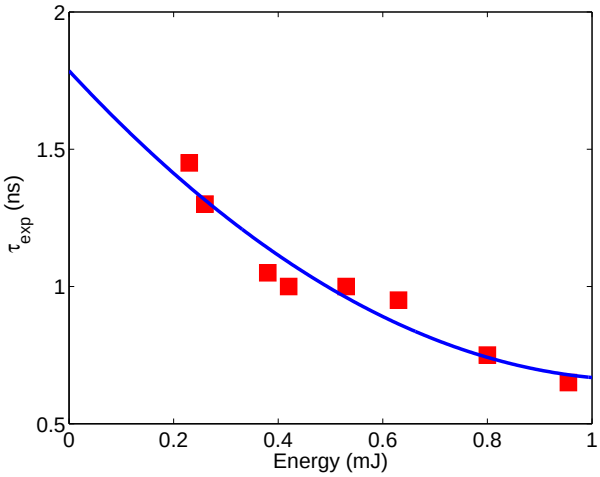

Figure 8.3: Experimental time-constants versus the pump-pulse energy. Red data are experimental points. The blue solid curve is a guide for the eye.

in order to find out the correct dynamics.

Another important experimental result is that the PL emission was found to have a very high saturation threshold. In Fig 8.4, a typical measurement of the time-integrated PL intensity is shown (in the case of an I sample) as a function of the pump-pulse energy. The usual saturated intensity formula $I(E) \propto E/(1+E/E_s)$ gives the saturation energy best-fit parameter $E_s > 1$ mJ for all samples ($E_s = 1.3$ mJ in the case of Fig 8.4), while a linear best-fit in the range $0 \div 1$ mJ (also shown in the figure) is a good approximation of the behaviour of the curve in the first half of the energy range. This holds true for each kind of sample.

A pump-pulse energy of 1 mJ corresponds to a peak density of photo-generated electron-hole pairs ($e - h$) of about 6×10^{20} cm^{-3}. In this sense, the expression "photoinduced plasma" can be used here to stress that the photoexcited carrier density is extremely high compared with the typical impurity density, which is less than 10^{19} cm^{-3}. This definition does not regard the strength of the electrostatic interactions or many-body effects, which are usually connected to the concept of "plasma". For these reasons, it is clear that such an high saturation threshold cannot be ascribed to the filling of the impurity levels. It may be rather related with Auger recombination effect or with plasma screening effects. The estimated plasma frequency of the photo-generated carriers at the highest pulse energy, assuming free electron masses for both electrons and holes, is about 6×10^{14} Hz, i.e. 500 nm. Therefore, it is possible that some partial screening of the UV excitation light is taking place, and it is decreasing the absorption efficiency. For this reason, the discussion and the model-test, in the following sections, will be focused on the non-saturated energy range ($0 \div 1$ mJ).

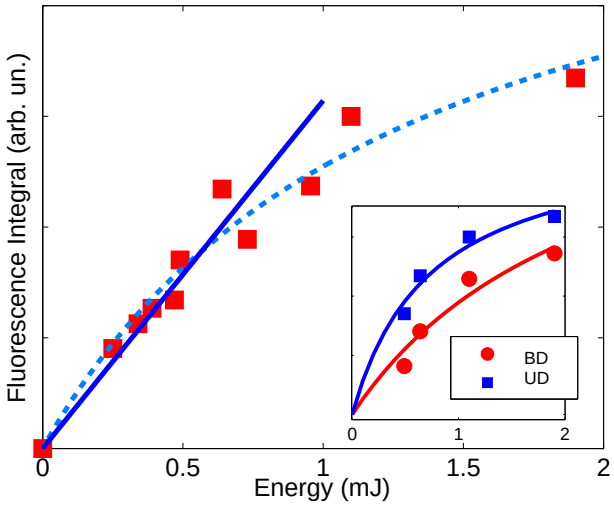

Figure 8.4: Time-integrated PL intensity (I sample) as a function of the pump pulse energy: blue solid curve is a linear fit in the range $0 \div 1$ mJ. Dashed curve is the saturated behaviour in the whole energy range ($E_s = 1.3$ mJ). Inset: the same saturation behaviour for the unimolecular and bimolecular components (see next sections).

8.2.2 Kinetic models.

As mentioned before, a simple exponential decay cannot describe our data. This excludes, thus, the presence of a simple "unimolecular" recombination mechanism or unimolecular decay (UD), as happens, for instance, in a typical impurity-assisted emission. In that case, the fluorescence is due to the recombination of the charge carriers which are trapped near an impurity level. The trapped carrier has its own characteristic lifetime τ_{UD} and the intensity $I(t)$ of the luminescent emission at any instant t is proportional to the rate of recombinations through a quantum yield constant. If $n(t)$ is the photoinduced carrier population of the fluorescent level or band, we can write the following rate equation:

$$I(t) = -Q\frac{d}{dt}n(t); \quad \frac{d}{dt}n(t) = -\beta n(t), \tag{8.1}$$

where Q is the quantum yield constant, which has to account for the quantum efficiency of the emission process, and β is the recombination probability per unit time.

The solution of Eq. 8.1 is

$$I(t) = I_0 \exp(-t/\tau), \tag{8.2}$$

where $\tau_{UD} \equiv 1/\beta$ is the characteristic lifetime and $I_0 = Q\beta n_0$ is a constant, and it depends of the initial carrier density $n_0 = kU$, where k is the absorption coefficient and U is the laser flux. In summary, the UD intensity as a function of the laser flux

U has a constant lifetime while the initial peak has a linear behaviour with the laser flux.

This kind of recombination mechanism cannot lead to a carrier density dependent lifetime.

If the electron-hole recombination takes place between mobile carriers (electron, hole or both), one has to take into account a partner-capture probability per unit time. This means that the mobile electron, for instance, needs some time to find a recombination center (hole), but, once it happened, the mobile carrier suddenly recombines. The capture event is, thus, the rate-limiting step for the electron-hole recombination. Let us note that the final recombination process can correspond to a direct recombination as well as a recombination via an intermediate short-lived state. This leads to a so-called "bimolecular" recombination rate equation.

In a bimolecular decay (BD), the recombination rate is, thus, proportional to the product between the density of electrons (n_e) and the density of available recombination sites (n_h). Both quantities depend on doping: in our case (n-doping) we have $n_e = n_0 + D$ and $n_h = n_0$, where D is the doping-induced carrier density. Let us assume that the doping level is negligible, since, if it is not true, only slight changes have to be considered in the following results. In the case of photoinduced electron-hole pairs in a pure material, these two quantities are both equal to the number of absorbed photons n, and, thus, we have:

$$I(t) = -Q\frac{d}{dt}n(t); \quad \frac{d}{dt}n(t) = -\gamma n^2(t), \tag{8.3}$$

where γ is so-called "bimolecular constant".

The solution of Eq. 8.3 is

$$I(t) = \frac{I_0}{1 + n_0\gamma t}. \tag{8.4}$$

The value $\tau_{BD} \equiv 1/(n_0\gamma) = 1/(kU\gamma)$ can be thus defined as the bimolecular carrier density dependent lifetime. The amplitude $I_0 = Q\gamma n_0^2 = Q\gamma k^2 U^2$ scales as the square of the laser flux U.

Another mechanism which can lead to a variable lifetime is the so-called Auger effect. Auger recombination occurs predominantly at very high carriers injection, since three charge carriers are involved in it. Since it is a non-radiative process, the quantum yield constant Q has to vanish, and the emitted intensity is therefore $I(t) = 0$. The third carrier gets the energy and momentum in order to let the electron-hole recombination happen. The recombination rate-equation which rules this process is, thus, cubic in the carrier density:

$$\frac{dn}{dt} = -\delta n^3, \tag{8.5}$$

where δ is the Auger constant. The solution of Eq. 8.5 is:

$$n(t) = \frac{2n_0^3}{\left(1 + 2n_0^2\delta t\right)}. \tag{8.6}$$

The Auger lifetime $\tau_A = \left(2n_0^2\delta\right)^{-1}$ is, again, dependent on the carrier density, but it scales as the inverse square of n_0. If there is a radiative decay channel too, whose carriers belong to the same population $n(t)$ which is emptied by Auger effect, it will be possible to see the Auger dynamics through the radiative decay, superimposed with the radiative dynamics of that channel. If the latter is much slower, only the Auger effect will be seen.

8.2.3 Best-fit procedure and program.

In order to discriminate between several different kinetic models, one needs a very accurate and careful numerical analysis of the data. In this section we will expose the best-fit procedure we used to this purpose.

Since more than one model was found to give a quite good best-fit result on a single curve, for a given pump-pulse energy, we measured many decay curves $(8-10)$ in the same experimental conditions, at different energies: the measured pump-pulse energy, relative to each decay curve, is given to the best-fit program as an external parameter. Many test-functions are calculated with these energies, and compared with the data. The final χ^2 function is then the sum of all the χ^2 functions obtained by this comparison. In this way, we can understand how much the test-function is capable to predict the energy behaviour of the decay curves rather than the quality of the single best-fit. We called this procedure "Global fit".

The major difficulties which can arise from this approach are linked to the precision of the measured pulse-energy, since even a small error on it can prevent the test-function to correctly predict the curve slope.

In order to avoid this, one can note that the integral of the decay curve itself can be a good measure of the pulse energy, since a linear relationship exists between these two quantities, at least in the non-saturated regime $(0 \div 1$ mJ). Thus, for each data set, the measured energies are used to make a linear fit of the decay curve integrals and to find out the linear coupling constant. The decay curve integrals are then used as a direct measurement of the pulse energy. Finally, these values are given to the best-fit program as input parameters.

A further test of our proposed kinetic model can be obtained from the energy behaviour of the linear coefficients too. If the test-function is made by several terms, each of them must have an amplitude with a well defined energy behaviour. The amplitude best-fit values are found separately for each curve by a linear regression, and their behaviour can be compared with the predicted one.

Another subtle problem which has to be considered with great attention is the deconvolution procedure of the as-recorded PL signal with the instrumental response function.

In Fig 8.5 the instrumental response function (RF) is compared to a typical decay curve. Although it is evident that the PL decay is slower than the RF, the difference is not so strong to allow the approximation of the RF with a simple Dirac delta function. The PL signal has to be deconvolved in order to extract the correct waveform. Being $S(t)$ the PL signal, and $r(t)$ the response function, the recorded

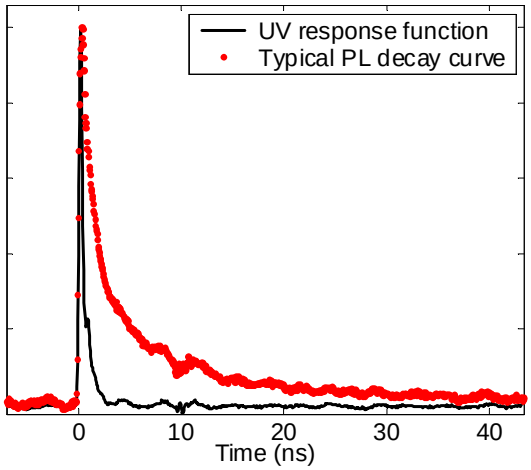

Figure 8.5: A comparison between the UV response function (black solid curve) and a typical STO PL decay curve (red points). Each curve is normalized to its maximum.

signal $I(t)$ is, actually, a convolution product between $S(t)$ and $r(t)$:

$$I(t) \propto \int_{-\infty}^{\infty} r(t-\tau)S(\tau)d\tau.$$

In order to obtain $S(t)$ from $I(t)$ one should deconvolve the recorded function. Since numerical deconvolutions are known to amplify the noise of high-frequency data, this approach was found to be not the more suitable one.

A convolution product becomes an algebraic product in the Fourier space. Starting from this fundamental theorem, it is possible to choose the following approach: called $F(t)$ the theoretical function under test, we can calculate the Fourier transformed function $\tilde{F}(t)$ by a Fast Fourier transform (FFT) algorithm. For input vector x having N elements, the FFT is a $N-$vector X:

$$X(k) = \sum_{n=1}^{N} x(n)e^{-2j\pi(k-1)(n-1)/N},$$

while the Inverse Fast Fourier transform (IFFT) is given by

$$x(n) = \frac{1}{N}\sum_{k=1}^{N} X(k)e^{-2j\pi(k-1)(n-1)/N}.$$

The function $\tilde{F}(t)$ can be, then, multiplied with the Fourier transform $\rho(\omega)$ of the response function $r(t)$ and the final convolved function will be the inverse transform of that product. In Fig 8.6 the real and imaginary parts of $\rho(\omega)$ are shown. In this way, it is possible to directly compare the as-recorded function $I(t)$ with the

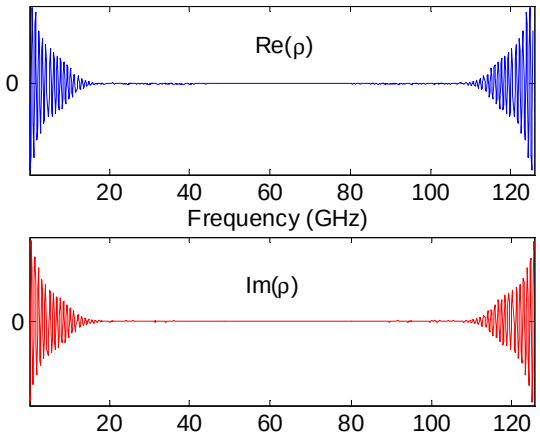

Figure 8.6: Real and imaginary parts of the Fourier transform $\rho(\omega)$ of the response function $r(t)$.

convolution product of $F(t)$ and $r(t)$ in the time-domain. The χ^2 function can be, thus, calculated in this domain and eventually minimized in order to find the best-fit parameters. Besides the theoretical test-function, each curve has to be fitted with two non-physical parameters: the background shift and the zero-time point. The former is easily set to zero, before starting the fitting procedure. To fit the time-shift constant t_0 represents the main difficulty. The problem resides in the discrete time-sampling: in the continuous Fourier transform theory, a time-shift constant t_0 would result into a phase-shift $e^{i\omega t_0}$ of the transformed function. This statement is not true for the discrete Fourier transform. In this case, the time-shift constant has to be a integer multiple of the time-step Δt. If it is not so, the amplitude of the transformed function will be affected by an "interference" effect, which can result in the vanishing of the whole function for $t_0 = \Delta t/2$. Moreover, in the time-domain, an adjustment of the time-shift constant, which is not a integer multiple of the time-step, should require an interpolation of the time-scale, introducing some unwanted troubles. In order to avoid all these problems, the time–shift constant t_0 is not best-fitted within the minimization command for the χ^2 function, as the other parameters are. The best-fit program starts from the initial value $t_0 = 0$, since the data-set is forced to have its maximum in the $t = 0$ point. After the best-fit procedure is finished, the program calculates the half-rise point of the fitted curve and compare it with the half-rise point of the data set. If the difference between this value is higher than the unit time-step, the program gives a "true" output (bit 1), in the other case it gives a "false" output (bit 0). Since there are several curves (one for each pump-pulse energy), the final output is a vector. The number of its non-vanishing elements is called $\#t_{sh}$. If this number is higher than a threshold number N^*, the program shifts that curves which corresponds to the non-vanishing elements of the time-shift vector and the procedure is repeated over again until the condition $\#t_{sh} < N^*$ is true. The usual value of N^* is 1. The choice of the half-rise point rather than the

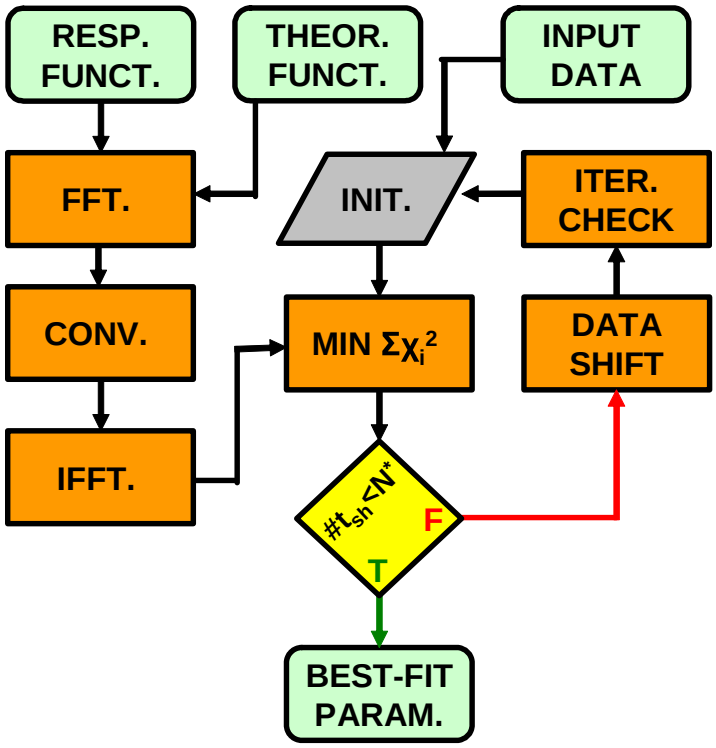

Figure 8.7: Flux diagram of the Global Fit Program (see text).

maximum was done since that is the point at which the derivative of the curve is larger. This allows the highest precision in the choice of the time-shift constant.

In Fig 8.7, a simplified flux diagram is shown: the RF and the theoretical test function are passed to the Fast Fourier Transform function (FFT), they are convolved together (CONV.) and then transformed again with the Inverse Fourier Transform function (IFFT). The input data (i.e. the set of all PL emission curves) is initialized in the INIT. module, where the energies relative to each curve are calculated from the time-integral of each curve as explained before, the background is set to zero, and some other technical initializations have been done. The initialized data and the convolved theoretical test function are then passed to the function MIN $\Sigma\chi_i^2$, in which the χ_i^2 functions are calculated for each curve (label i) and the sum of all χ_i^2 functions is minimized by the Matlab "fminsearch" function. In the next block, the t_{sh} vector is calculated, and the number of its non-vanishing elements $\#t_{sh}$ is compared to the threshold N^*. If the logic value is false, the DATA SHIFT block provides to shift only those curves which correspond to the non-vanishing elements of the vector t_{sh} and the best-fit procedure starts again. The ITER. CHECK block stops the procedure when a certain threshold of iterations is exceeded.

The complete best-fit program is reported in App. D.

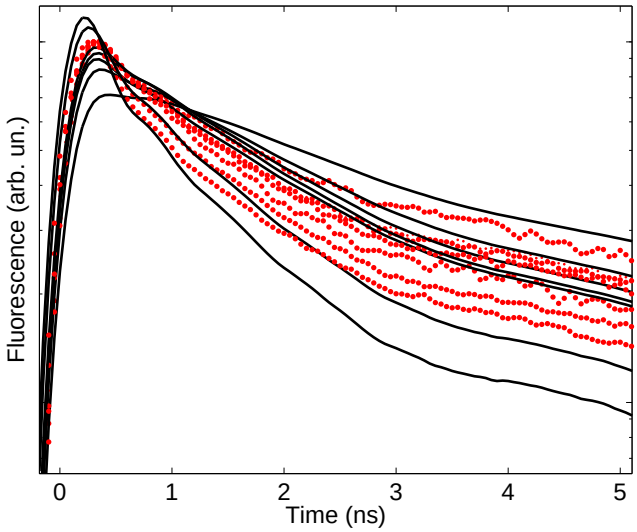

Figure 8.8: Global fit on a set of decay curves (Nb sample) within the Auger decay model. This is a zoom on the first part of the decay curve in a semilogarithmic vertical scale. Red points are data, black solid lines are the best-fit curves.

8.2.4 Data analysis.

The first theoretical test function we used to interpret our data, is the Auger decay model, since in a high carrier density regime it is usually the most important contribution in semiconductors [90],[91]. In Fig 8.8 an example of the result of the Global fit is shown: it is clear that the Auger model cannot follow correctly the behaviour of the first part of the PL emission curves with the pump-pulse energy. In particular it seems that the Auger model is "too fast", with respect to the data. Moreover, since the Auger effect is entirely non-radiative, its presence should also result into a saturated quantum yield, which, in our, case starts to appear only above a pump-pulse energy of 1 mJ. We can infer that the Auger effect is negligible at least below this threshold, and this sets an upper limit for the Auger coefficient δ:

$$\delta \leq 10^{-33}\ \mathrm{cm}^6\ \mathrm{s}^{-1}$$

This value is two or three orders of magnitude smaller than the usual Auger coefficient value in normal semiconductors, which is about $10^{-30} - 10^{-31}$ cm^6 s^{-1} ([90],[91]). The reason can be found, probably, in the large band-gap of the STO, since the Auger coefficient is known to decrease exponentially as the band-gap width increases [92].

We have seen that the Auger lifetime scales as the inverse square of the laser flux. Since this behaviour is not confirmed by our data, the next attempt was to put a pure bimolecular decay model to the test. The result of the Global fit for the BD model is shown in Fig 8.9: it is seen that the model reproduces correctly the behaviour of the first part of the curve, where the Auger model failed, but it is not able to correctly fit the longer "tail" of the curve, which starts after about $3-5$ ns.

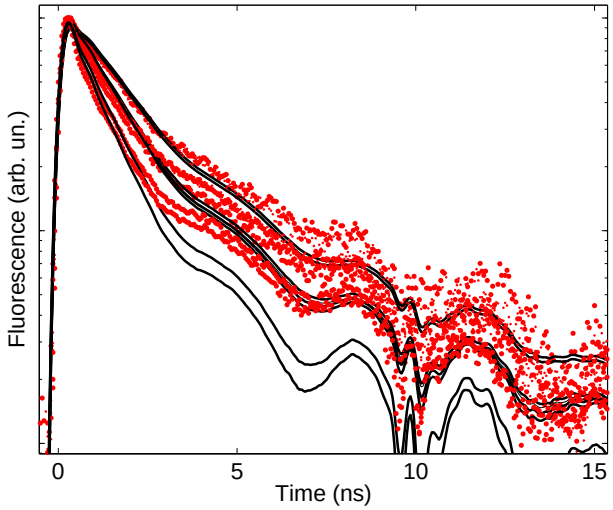

Figure 8.9: Global fit on a set of decay curves (O sample) within the bimolecular decay model. The plot is in a semilogarithmic vertical scale. Red points are data, black solid lines are the best-fit curves.

To a deeper investigation, it is possible to see that the initial decay becomes clearly faster as the pulse energy increases, but the slower "tail" changes only its amplitude and not its decay rate. This excludes an interpretation as a simple unimolecular (UD), bimolecular (BD) or Auger decay.

It has to be noted that Eq. 8.4 holds true under the hypothesis that the electron and hole density are equal. It is possible to prove that the presence of a doping term into the BD recombination rate equation, i.e. $n_e = n_h + D$, where n_{e-h} is the electron (hole) density and D is the doping carrier density, produces an exponential "UD-like" term in the final form of the PL emission. Despite this result, this model was found to not give a correct best-fit, even in doped samples, where the approximation $n_e \simeq n_h$ is surely false.

Starting from these considerations, a combination between different kinetic models has to be invoked. The hypothesis is that there is a mixed kinetics, i.e. there is the presence of two different decay channels.

In particular we can choose a BD model to account for the faster initial peak and an UD model which could account for the slower tail, where the bimolecular contribution is vanishing.

If both UD and BD decay channels are present in the material, several ways are possible to mix them.

One is to write a rate equation of the form:

$$\frac{d}{dt}n(t) = -\gamma n^2 - n/\tau,$$

in which a single balanced population $n(t)$ obeys to a single UD-BD rate equation, where γ is the bimolecular coefficient and τ is the unimolecular exponential time. This model leads to a PL intensity form which is able to fit the single decay curve.

Nevertheless, the Global fit procedure ruled out this model, since it cannot fit the whole set of curves.

Finally, the model which gave the best results is based on the assumption that there is a very rapid initial branching of the charge carrier population into two separate non-communicating channels. Each channel obeys, then, to a different rate equation. This means that, immediately after the UV-excitation, two different electron-hole populations are formed: one shall follow an unimolecular decay law while the other a bimolecular one. We assume that, in each population, the number of electrons and holes is the same (even in doped samples) and that the branching ratio is not dependent on the pulse energy, so that at time $t = 0$ we have $n_{UD}(0) = k_{UD}U$ and $n_{BD}(0) = k_{BD}U$, where U is the excitation energy density and $k_{UD,BD}$ are two constants which account for both the branching ratio and the UV absorption coefficient (the latter being common to both channels). The rate equations will be, thus:

$$\frac{d}{dt}n_{UD}(t) = -n_{UD}/\tau_{UD},$$
$$\frac{d}{dt}n_{BD}(t) = -\gamma n_{BD}^2.$$

Being Q_{UD} and Q_{BD} the UD and BD channels quantum yields, the resulting PL intensity is given by:

$$\begin{aligned} I(t) &= -Q_{UD}\frac{d}{dt}n_{UD} - Q_{BD}\frac{d}{dt}n_{BD} = \\ &= c_{UD}\exp(-t/\tau_{UD}) + c_{BD}\left(1 + t/\tau_{BD}\right)^{-2}, \end{aligned}$$

where $\tau_{BD} = 1/\gamma k_{BD}U$ is the energy dependent bimolecular time-constant and

$$c_{UD} = Q_{UD}k_{UD}U/\tau_{UD} \;\; ; \;\; c_{BD} = \gamma Q_{BD}k_{BD}^2U^2$$

are the UD-BD amplitudes.

This model can fit very well the whole set of decay curves, both in pure and doped samples. Let us note that τ_{UD} and τ_{BD} are independently constrained by each single decay curve, so that they are independent of the excitation energy. Thus, they provide a strong confirmation of this model. In Fig 8.10 an example of the Global fit procedure, which tests this model, is shown.

Let us note that the initial decay follows very well the predicted behaviour. In Fig 8.11 the UD and the BD decays and their sum are plotted separately. The UD and BD amplitudes are found to follow quite well the predicted behaviour too, as shown in Fig 8.12. Besides confirming the model, this result leads also to the conclusion that the BD channel is not sensitive to the doping level, since c_{BD} scales as U^2 without any linear term in doped samples too, while it is easy to prove that the doping constant D in the carrier density n_e should result into a linear term in the c_{BD} expression. Moreover, both channels are not saturated in the investigated range, while, in the whole range ($0 \div 2$ mJ), we observe the onset of saturation in both (see the inset of Fig 8.4).

Let us now compare the quantitative results in I, Nb and O samples. In Fig 8.13 the UD and BD PL-integrals are shown as a function of the pulse energy. The

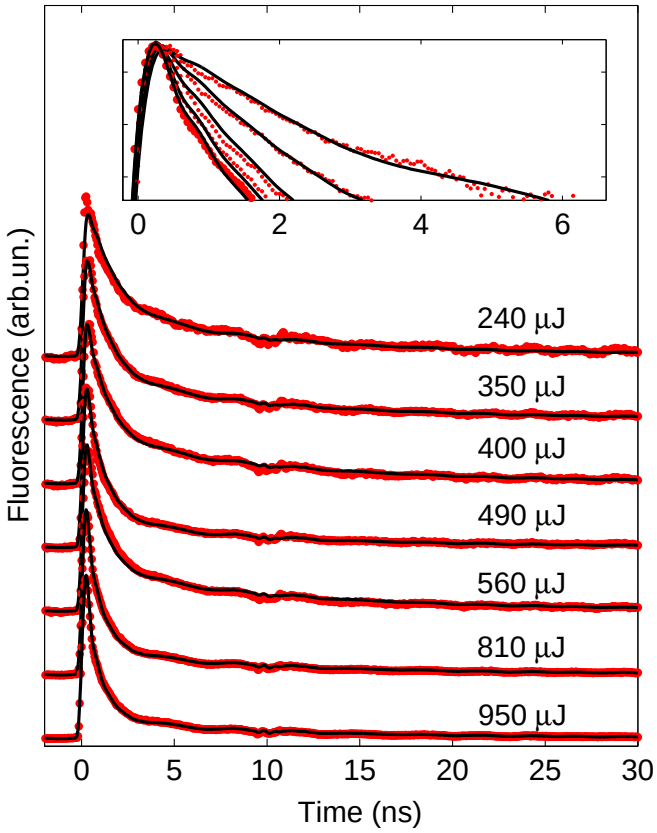

Figure 8.10: Example of a Global fit on a set of decay curves (I sample). Pulse energies are given on the right of each curve. Black solid lines are the best-fitting curves. Inset: zoom of the peak in the same set on a semilogarithmic vertical scale. Some curves are not shown for clarity.

behaviour is almost linear for all, and the BD (UD) yield is the slope. The differences are very small, and they are smaller than the sample-to-sample variations. The doped samples yield was found to be almost systematically smaller with respect to the pure samples one, probably because of optical absorption in the visible range. The measured yield ratios of the BD to UD channels are in the range $0.6 \div 0.8$ for all samples. The most relevant differences between I, Nb and O samples are found in the UD lifetimes: I and O samples show an UD lifetime in the range $11 \div 24$ ns, while the Nb samples lifetime is systematically lower, with $\tau_{UD} \sim 5 - 6$ ns. The BD dynamics of Nb samples is found to be faster too, but the difference is less pronounced: in every kind of sample the BD lifetime is in the range $300 \div 600$ ps for the highest pump-pulse energy (1 mJ).

Since the ratio k_{UD}/k_{BD} is unknown, we cannot extract the value of γ from these data. However, assuming a balanced branching ratio (i.e. $k_{UD}/k_{BD} \sim 1$) we can get a rough estimate of the bimolecular constant: $\gamma \sim 10^{-11}$ cm^3/s. This value is two-three orders of magnitude larger than those reported for indirect semi-

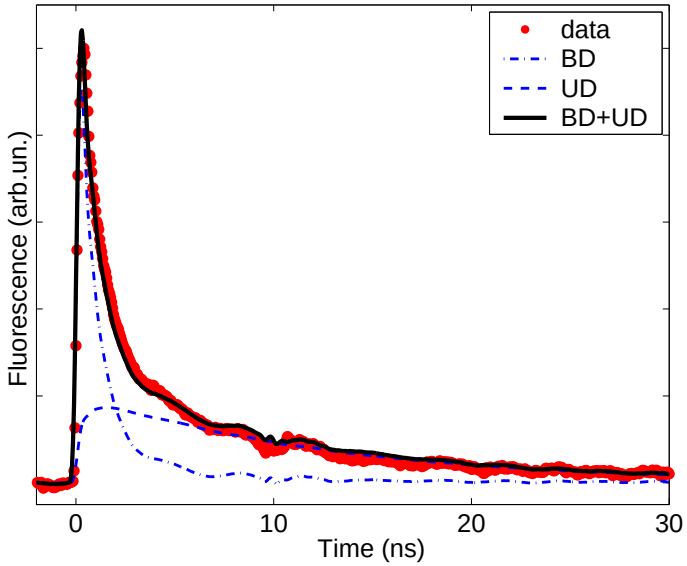

Figure 8.11: UD (blue dashed) and BD (blue dot-dashed) curves are drawn separately for a particular decay curve (I sample). Black solid curve is the best fit curve, defined as the sum of the UD and BD contributions.

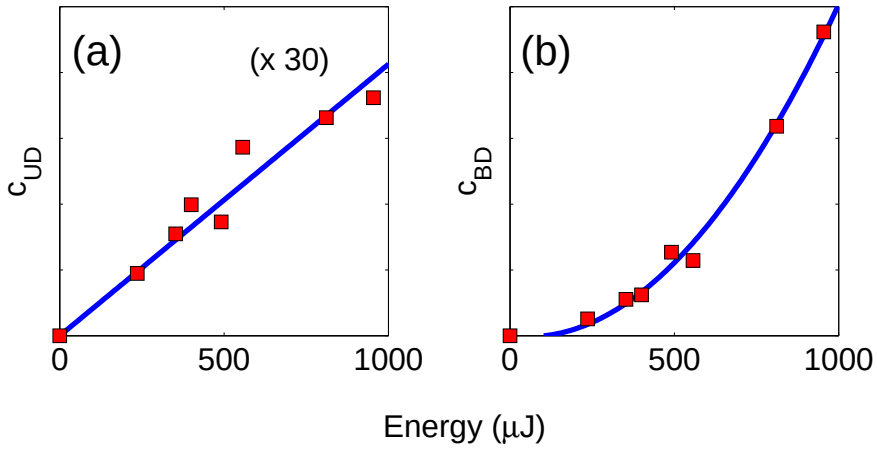

Figure 8.12: UD (a) and BD (b) amplitudes versus the pulse energy. Red squares are data, blue solid lines are a linear (UD) and pure-quadratic (BD) best-fit curves. UD and BD amplitudes are on the same scale, but the former is multiplied by a factor 30.

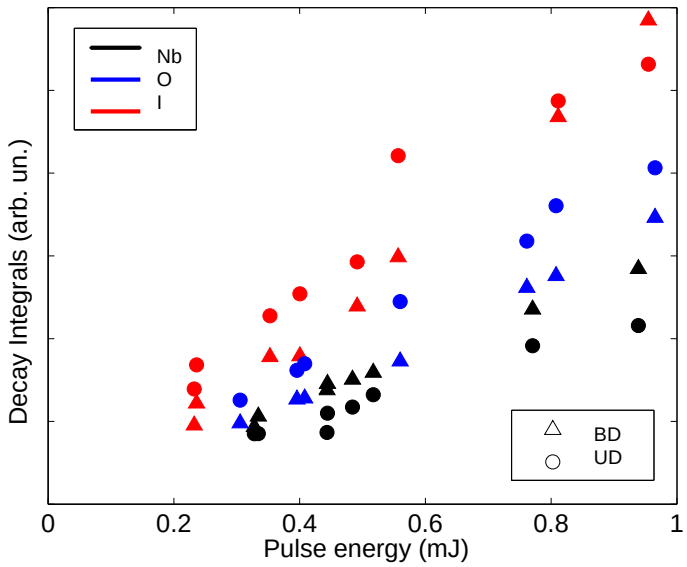

Figure 8.13: BD (triangle) and UD (circles) PL integrals versus the pulse energy in I, Nb and O samples.

conductors, usually ascribed to phonon-assisted radiative or defect-assisted Auger recombinations [91], but it is one-two orders of magnitude smaller than the values which have been found in direct band-gap semiconductors [93].

8.3 Experimental results: frequency domain.

The typical photoluminescence spectra of I, Nb and O samples are shown in Fig 8.14. The spectra were collected with pulse energies ranging from 50 μJ up to 1 mJ and it was found that the spectral integral scales linearly with the energy at room temperature. All spectra have their peak at about $425-430$ nm (2.9 eV) with a long tail reaching about 650 nm (1.9 eV). These spectra are quite similar to those reported in literature (for instance in Fig 7.6), although they seem to present a slightly more pronounced green-red tail. A very pronounced difference, with respect to that work, is that we saw a roughly equal emission yield from each kind of sample, while Kan and coworkers [82] found a strong difference between pure and doped samples. This discrepancy will be discussed in the last section of this Chapter.

Since the time-domain study revealed the presence of two distinct decay channels, we tried to resolve some possible spectral differences between UD and BD channels by inserting some additional filters in the detection line and checking for variations in the yield ratio or in the decay lifetime. In particular we use a $390-480$ nm band-pass filter and a 495 nm long-pass filter, in order to select the blue and the green part of the spectrum, respectively. In both cases, no significant changes were found. Let us note that the time-resolved measurements are sensitive to the radiative as well as the non-radiative channels, while the spectral features depends entirely on the radiative recombinations. This result could, thus, suggest that the UD and BD

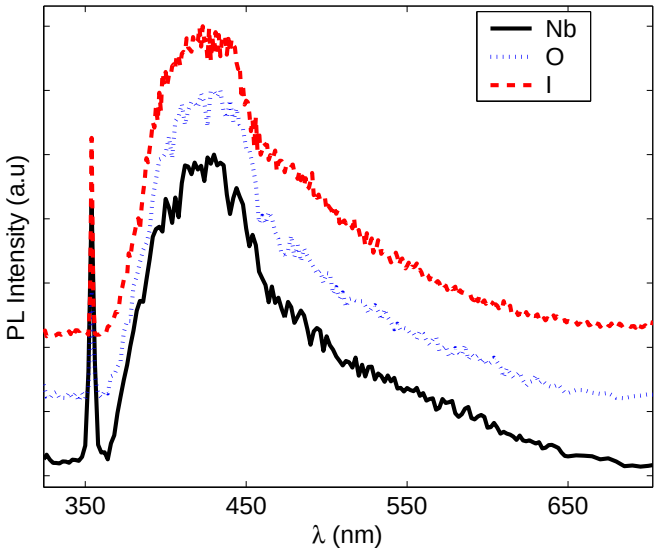

Figure 8.14: Normalized PL spectra of I, Nb and O samples. Spectra are vertically shifted for clarity.

channels emission spectra are largely overlapping or, alternatively, one of the two decay channels can be a non-radiative one.

8.3.1 Temperature investigation.

The most remarkable differences between pure and doped samples can be obtained from an investigation of both spectra and decay curves at different temperatures. The investigated temperature range is $300 \div 900$ K and all measurements were performed in air. Since it is known that STO is very sensitive to the oxygen concentration, and since the annealing at such temperatures can change this value, we performed several measures by increasing, decreasing and "randomizing" the temperatures, in order to be sure that all measurements are perfectly reproducible, i.e. that the air exposure at these temperatures does not change significantly the optical behaviour of the sample. This was found to be true for I and Nb samples, but not for O samples, which completely change their nature, and become white-transparent insulators. In other words, O samples return to their original status before the annealing in vacuum. This is expected, since the oxygen present in the air has the effect to reverse the annealing in vacuum which was used to prepare them. For this reason, O samples were not investigated, and, in this section, only measurements on I and Nb samples are reported.

In Fig 8.15, several I sample spectra at different temperatures are shown: the pump pulse energy is about 50 μJ. These spectra exhibit many remarkable features, common to all pure samples. First of all, we can easily see a progressive depletion of the overall PL generation efficiency. This is not surprising, since thermally activated non-radiative decay channels become stronger and stronger as the temperature increases. This depletion does not take place as a decreasing amplitude for the whole

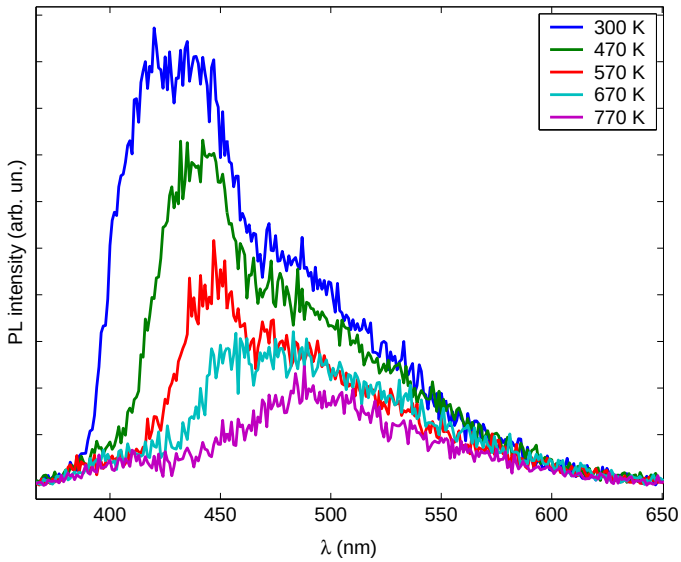

Figure 8.15: I sample spectra at different temperatures. Pulse energy: 50 μJ.

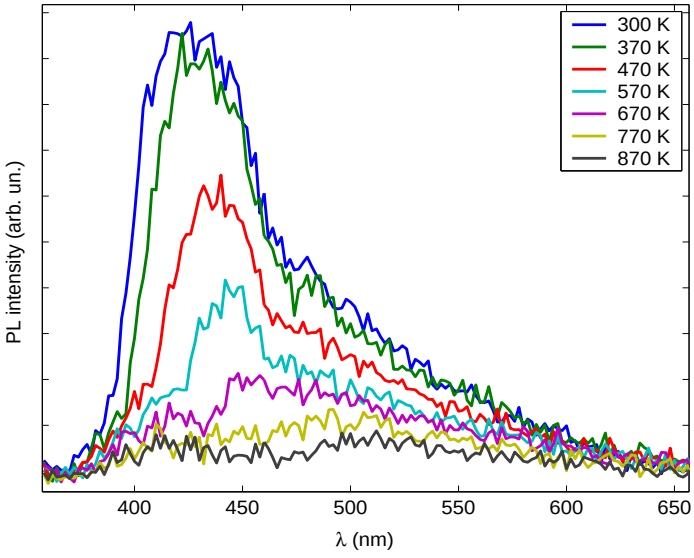

Figure 8.16: I-sample spectra at different temperatures. Pulse energy: 500 μJ.

spectrum: the shape of the spectrum clearly changes. The PL color, as seen with naked eyes, changes from blue to green. In particular it is possible to resolve two bands: a blue band peaked at about $430 - 440$ nm ($2.8 - 2.9$ eV) and a green band at about $490 - 500$ nm (~ 2.4 eV). These bands have the same energies of those observed by Mochizuki and coworkers [78]. The temperature behaviour of the two bands is different: the green band shows an usual depletion of its amplitude, while the blue band presents a "high frequency edge shift" effect. Moreover, a blue band residual still remains visible, although weak, at the highest temperature too.

In Fig 8.16 we can see the same spectra, on the same I sample, but with a pulse energy of about 0.5 mJ, i.e. ten times higher. All the previous considerations are still valid, but the ratio between the high and the room temperature spectra is different: the high-energy high-temperature spectrum is weaker than the low-energy high-temperature one, with respect to the relative low-temperature spectra. This seems to concern in particular the green band. Although the room temperature spectra are very similar in both cases, it is possible to see that the low-energy spectrum has a more pronounced green shoulder than the high-temperature one. We cannot relate directly this evidence with the presence or absence of a bimolecular decay channel, since the lowest energy at which we can perform a time-resolved measurements is about 200 μJ, but it can be an useful indication in order to spectrally resolve the BD and UD contributions, if possible.

The model we used in order to account for these features, is based on the presence of three bands: two blue bands and one green band. The green and one of the blue bands (label 1) are Gaussian bands. The other blue band (label 2) is a Gaussian band too, but it is multiplied by the Fermi distribution, in order to account for the spectral shape changes. The Fermi function cannot correctly account for them unless the chemical potential μ can change its value with temperature. Let us make an important consideration about this statement: the chemical potential, as it is usually defined, is referred to a system which is in a thermodynamical equilibrium. It can change with temperature, but usually, unless a very high temperature is reached, its variations have only a minor importance and are often negligible.

In our case, the photoinduced electron-hole plasma is, obviously, in a non-equilibrium condition. Thus, an effective chemical potential can be correctly defined only if the relaxation of the system to the original equilibrium condition happens on a time-scale which is larger than the time-scale of the thermalization of the photoinduced plasma. In our case the former time-scale is, as seen before, of the order of few tens of nanoseconds, while the thermalization of the carrier plasma usually happens in few picoseconds. The effective chemical potential can be thus defined as referred to a quasi-equilibrium condition of the photoexcited charge carriers. In this case, a stronger variation with temperature can be expected.

In order to put this empirical model to the test, we successfully tried to fit the whole set of spectra with a single minimization procedure, in a similar way to that exposed in the previous section for the time-resolved decays. Working in the energy domain, rather than wavelengths, the energy positions, the widths and the chemical potential values of each band are obtained, from the whole set, from the following

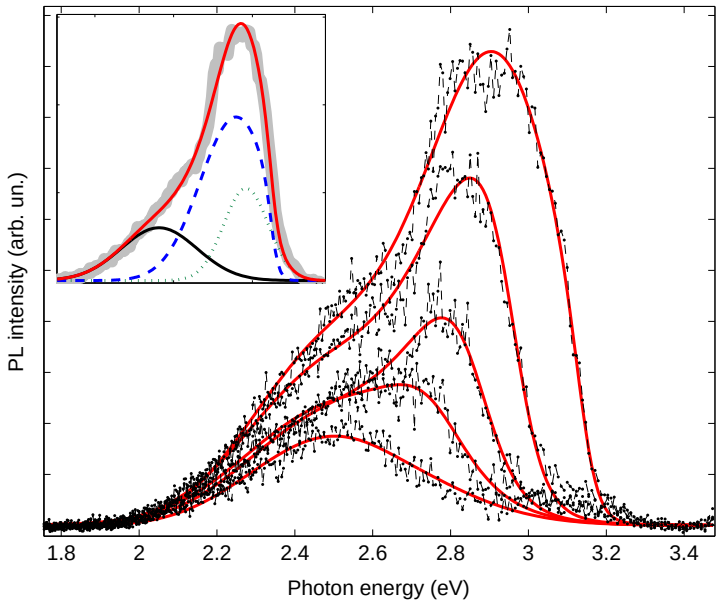

Figure 8.17: An example of the Global fit of spectra: the same low-energy spectra of Fig 8.15 are best-fitted by the three-bands model. Inset: the three bands are drawn separately for a particular spectrum.

relationship:

$$I(E) = \exp\left[-\left(\frac{E-E_g}{\sigma_g}\right)^2\right] + \exp\left[-\left(\frac{E-E_b^1}{\sigma_b^1}\right)^2\right] + \exp\left[-\left(\frac{E-E_b^2}{\sigma_b^2}\right)^2\right] \cdot f(E)$$

where

$$f(E) = \left[1 + \exp\left(\frac{(E-\mu(T))}{KT}\right)\right]^{-1}$$

is the Fermi function at temperature T, E_g is the green band energy, σ_g is its width, $E_b^{1,2}$ and $\sigma_b^{1,2}$ are the energies and widths of the two blue bands. In order to account for the chemical potential changes with temperature, one can assume, as a first approximation, a linear dependence: $\mu(T) \simeq A \cdot T + B$. If the temperature is given as an external parameter, the best-fit program will give the linear parameters A, B best-fit values.

In Fig 8.17 the result of this best-fit procedure is shown, while in the inset the three bands are plotted separately for a particular spectrum. In all samples the variation of the chemical potential falls in the range between $3.1 - 3.2$ eV at room temperature and $2.6 - 2.7$ eV slightly below 900 K. This means that we observe a 15% decreasing on a temperature range of 600 K. The green band peak lies between 2.4 and 2.45 eV and its width is about $0.3 - 0.4$ eV. The blue band 1 peaks at about $2.9 - 2.97$ eV with $\sigma_b^1 \sim 0.2 - 0.3$ eV. Finally, the blue band 2 peaks at about $2.87 - 2.89$ eV, and $\sigma_b^2 \sim 0.2 - 0.3$ eV. These results are very similar both in the high and low energies measurements, while the main difference can be found

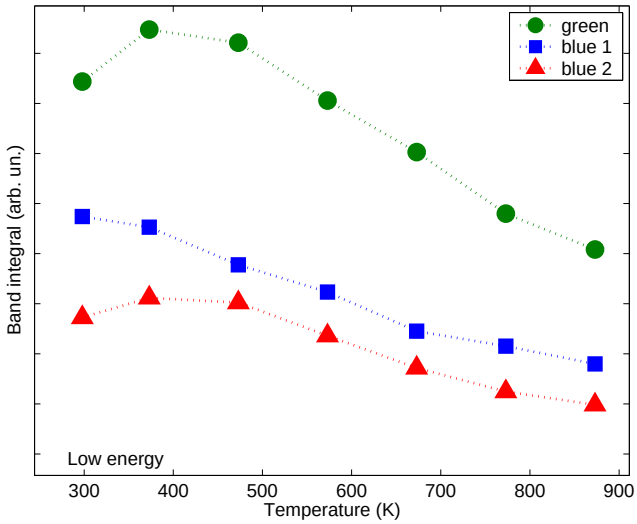

Figure 8.18: Band integral of the green, blue 1 and blue 2 bands as a function of the temperature in the low energy regime.

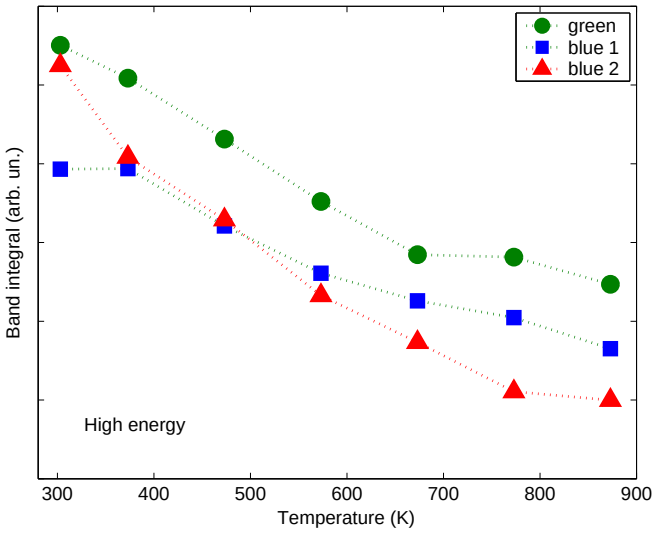

Figure 8.19: Band integral of the green, blue 1 and blue 2 bands as a function of the temperature in the high energy regime.

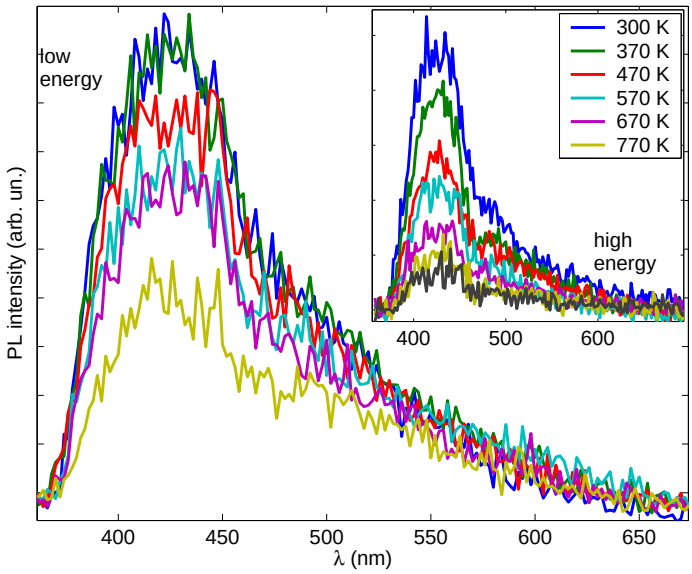

Figure 8.20: Low energy spectra of a Nb sample at different temperatures. Inset: the same spectra at higher energy. The highest temperature, not shown in the legend, is 870 K (black solid curve).

looking at the band integrals plotted in Fig 8.18 and 8.19: in the high energies regime the green band yield is larger but comparable with the blue bands yields, while in the low energies regime the difference is more pronounced since the green yield is comparable with the sum of the two blue yields. We have to mention that the measurements reported in Fig 8.18 and 8.19 are referred to a particular I sample in which these features are more marked than in other samples. However, this behaviour is qualitatively similar in all pure samples. The best-fit results seem to indicate that the peak energy of the two blue bands is the same. This suggests that we can assume a single energy band composed by two distinct populations, and, in turn, this could suggest a direct link between these two populations and the UD and BD populations. Nevertheless, the doped samples spectra go towards the opposite direction.

Doped samples, i.e. Nb samples, show a quite different behaviour, as can be seen in Fig 8.20. The overall yield is still decreasing, as for pure samples, but in this case the "high frequency edge shift" effect does not take place. However, it is still clear that the spectra are composed by the same two bands we have seen before. The high-to-low temperature integral ratio at high energy is smaller than the low energy one, but, in this case, the blue band remains slightly stronger than the green band even at the highest temperature. The green shoulder of the low energy spectra is more pronounced than in the high energy spectra, as in the case of pure samples.

For these reasons, we used a simplified best-fit model, with only two bands and without the Fermi function contribution. An example of the results of these best fit is given in Fig 8.21. The best-fit value of the green band peak is about 2.5 eV with $\sigma_g = 0.40$ eV, while the one of the blue band is about 2.9 eV with $\sigma_b = 0.25$ eV. On

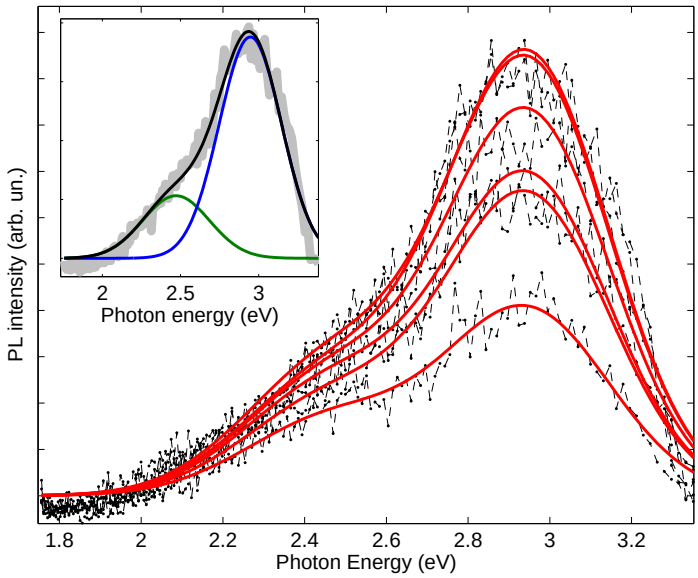

Figure 8.21: An example of the Global fit of spectra: the same N sample low-energy spectra of Fig 8.20 are global fitted within the two-bands-model. Inset: the two bands are drawn separately for a particular spectrum.

a deeper glance, it can be seen that all best-fit curves are above the experimental data in the very extreme high-frequency part of the spectra (above 3.2 eV). This is possibly due to the presence of the Fermi function, but its effect is very weak, and it is not possible to extract some reliable value of the effective chemical potential from these data.

8.3.2 Activation energies.

Non-radiative decay channels are usually thermally activated. When the PL emission kinetics is dominated by a non-radiative activated channel, the PL lifetime decreases as the temperature increases, since the fluorescent band is emptied by that activated channel. A radiative PL lifetime, on the contrary, is almost independent of temperature, since its value depends on the bandwidth. For this reason, if the activation energy of the total PL emission is found to be equal to the activation energy of its lifetime, this is a proof that non-radiative channels dominate the recombination kinetics. The probability per unit time to have a non radiative recombination event P_{NR} is ruled by an Arrhenius law:

$$P_{NR} = \nu_{NR} \exp\left[-E_a/k_B T\right]$$

where ν_{NR} is a constant, k_B is the Boltzmann constant and T is the lattice temperature. The total probability P per unit time to have a recombination event, being it radiative or not, is $P = P_R + P_{NR}$, where P_R is the radiative probability, and its inverse is the PL radiative lifetime $\tau_R = 1/P_R$. The total PL lifetime τ, i.e. the

inverse of P, is thus:

$$\tau = \frac{1}{P_R + P_0 \exp\left[-E_a/k_B T\right]} = \frac{\tau_R}{1 + \nu_{NR}\tau_R \exp\left[-E_a/k_B T\right]}. \tag{8.7}$$

Here ν_{NR} can be now regarded as a non-radiative recombination rate.

A similar relation holds true for the PL yield Y, since the radiated intensity is proportional to the ratio between the radiative probability P_R and the total recombination probability P:

$$Y = \frac{P_R}{P_R + P_{NR}} = \frac{1}{1 + \nu_{NR}\tau_R \exp\left[-E_a/k_B T\right]}. \tag{8.8}$$

We used Eq. 8.8 in order to fit the green, blue 1 and blue 2 yields and find the activation energies of the three processes. The band activation energy was found to lie in the range $140 - 160$ meV for the green band, $180 - 195$ meV for the blue 1 band (100 meV in one sample only) and $230 - 290$ meV for the blue 2 band. An example, in the case of the blue band 1, is given in Fig 8.22. We have to mention that these results hold for the high energy spectra, while Eq. 8.8 was not be able to correctly fit the low-energy data. The same relationship was applied on doped samples spectra: the activation energy best fit values are ~ 115 meV and ~ 155 meV for the green and the blue band, respectively.

8.4 Lifetime temperature dependence.

In this section, we report on the decay curves behaviour of pure and doped samples in the temperature range $300 \div 900$ K. These measurements are performed by recording a set of several different decay curves, at different energies, for each temperature. The Global fit procedure is applied, as previously mentioned, on each set, and the BD-UD parameters are then analyzed as functions of temperature. Let us now illustrate the results of this investigation on I samples. The behaviour of the unimolecular and bimolecular lifetimes (at fixed pulse energies) is shown in Fig 8.23 and 8.24. The activation energies, 130 and 123 meV, respectively, are found to be very similar. The UD yield activation energy (~ 130 meV) is found to be very similar to the UD lifetime activation energy, while the BD yield activation energy (~ 50 meV) strongly differs from the BD lifetime one. This result suggests that the bimolecular kinetics could be non-radiative (or not visible) and it would be revealed indirectly through a radiative channel. UD and BD yields as a function of temperature are shown in Fig 8.25.

The UD lifetime activation energies of doped samples (Fig 8.26, $E_a \sim 500 - 700$ meV) are very different from the I samples values as well as BD lifetime activation energies ($\sim 80 - 220$ meV). The value of the UD lifetime is almost constant below 700 K, and than it decreases abruptly. The same does not happen for the BD lifetime, as shown in Fig 8.27. The activation energies of the doped samples yields are in the range $195 - 250$ meV for the UD channel and $130 - 180$ meV for the BD channel. Both channel integrals are plotted together in Fig 8.28. These results seem to suggest that more than one activated channel is actually present, but a

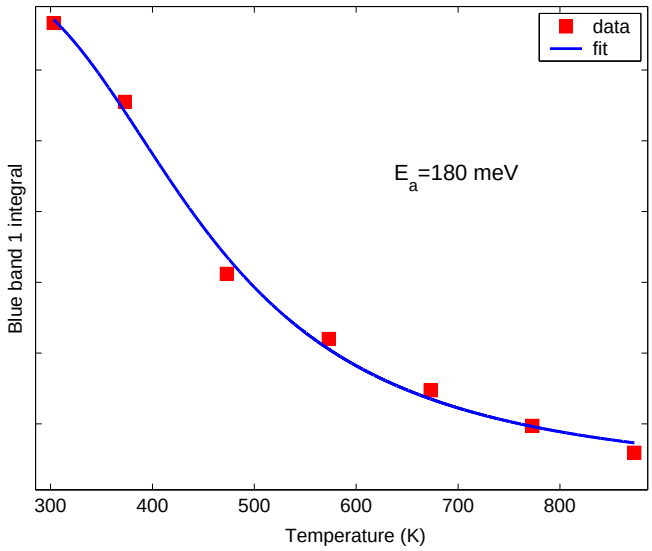

Figure 8.22: Activation energy best-fit curve (blue solid line) of the blue band 1 of a pure sample. Red points are the data. The best-fit value of the activation energy is 180 meV.

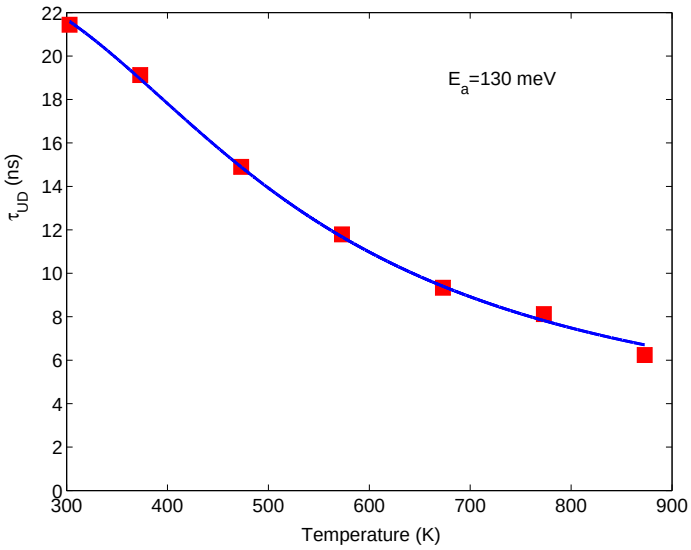

Figure 8.23: Temperature behaviour of the UD lifetime of an I sample. The activation energy is 130 meV. Red points are the data, blue solid line is the best-fit curve.

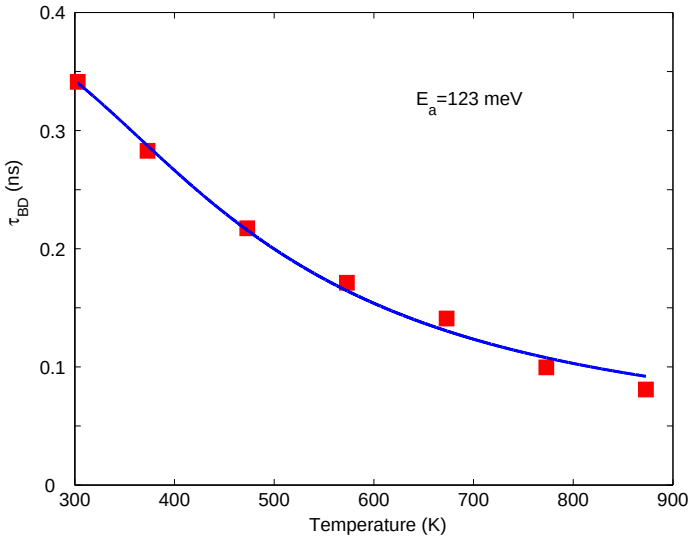

Figure 8.24: Temperature behaviour of the BD lifetime of an I sample. The activation energy is 123 meV. Red points are the data, blue solid line is the best-fit curve.

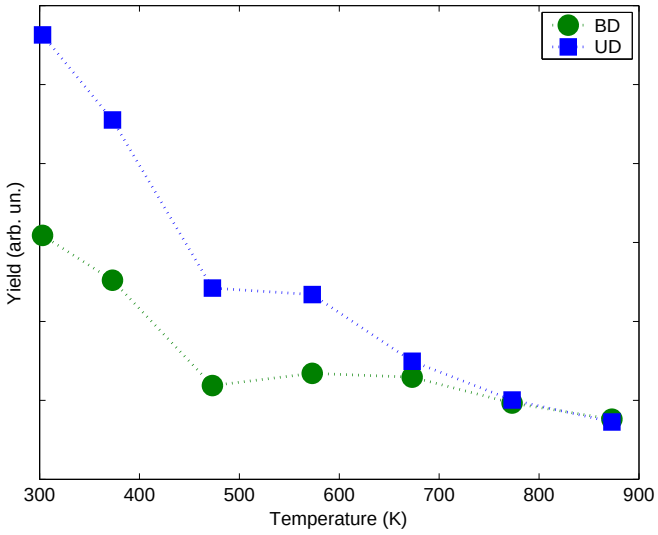

Figure 8.25: Temperature behaviour of BD and UD yields in the case of an I sample.

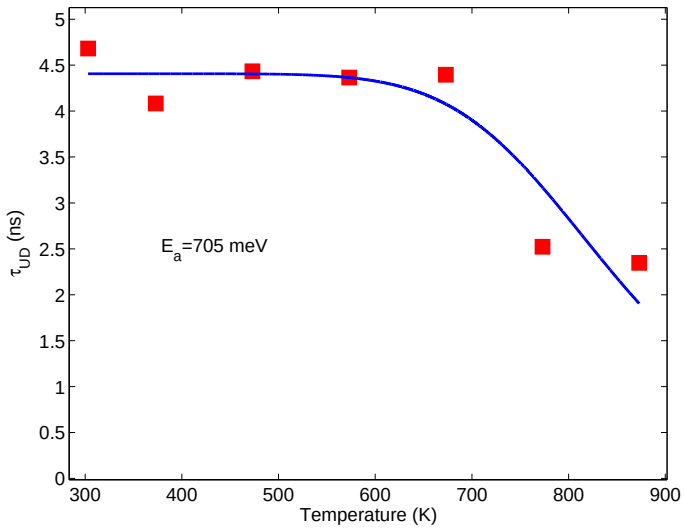

Figure 8.26: UD lifetime of a Nb doped sample as a function of temperature. The activation energy is 705 meV. Red points are the data, blue solid line is the best-fit curve.

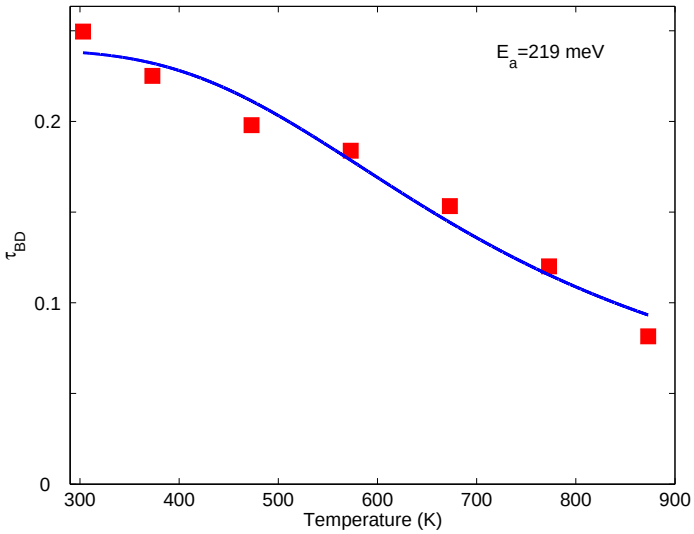

Figure 8.27: BD lifetime of a Nb doped sample as a function of temperature. The activation energy is 219 meV. Red points are the data, blue solid line is the best-fit curve.

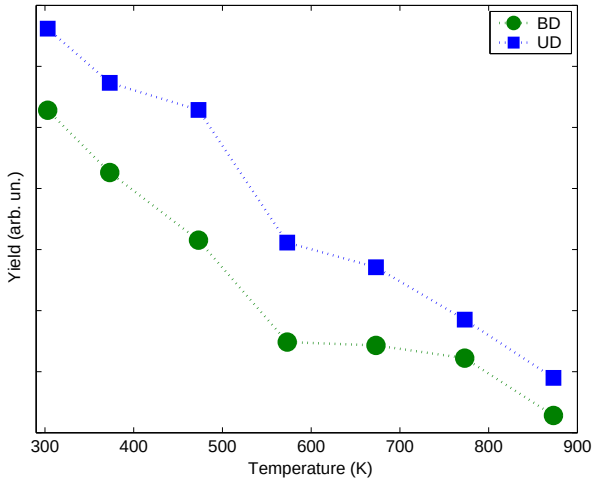

Figure 8.28: UD and BD yields as a function of temperature in a Nb sample.

conclusive statement cannot be proposed on the base of them. Finally, we made some preliminary measurements at low temperatures (between room and liquid nitrogen temperatures). Although a systematic study has not been performed yet, we can here report that both BD and UD lifetimes remain of the same order of magnitude in all studied samples. This statement, although qualitative, can be useful to compare these results with the one reported in literature, where the low temperature PL lifetime was found to lie in the range of several milliseconds [78].

8.5 Discussion.

First of all, let us note that frequency and time domain results are not directly comparable, since the spectrum is completely ruled by the radiative channels, while time-domain decay curves are ruled by both radiative and non-radiative channels, which dominate the recombination kinetics, as we have seen in the previous sections.

In order to obtain a reliable microscopic model of the PL emission in strontium titanate, many observed features have to be explained. Let us summarize briefly the main experimental results which have to be considered. The first is, of course, the presence of two distinct and mixed kinetics, the bimolecular and the unimolecular. The second is that the BD and UD contribution seem to be not spectrally resolved. The saturation energy threshold is extremely high. The BD-UD kinetic model affirms that two distinct and not interacting populations are formed few instants after the excitation. On the other hand, there is no reason to think that both channels have to be radiative. Pure and doped samples spectra, decays and yields are very similar (at room temperature). The temperature dependence of the spectra shows an "edge shift" effect in pure samples which is absent in Nb doped samples. The green band seems to saturate with the pulse energy before than the blue band, in both kind of samples.

The observed BD kinetics is likely to be ascribed to the direct non-radiative recombination of conduction band electrons (-polarons) and valence band holes (-polarons). At least one of them has to be mobile, in order to obtain a bimolecular kinetics. This process has to be defect- or phonon-assisted, because of the indirect band-gap of STO.

The observed peak of the PL spectra is shifted of about 0.35 eV (Stokes shift) with respect of the indirect band-gap, and the tail is extended over more than 1 eV below the excitation energy. These features cannot be explained by the emission of some phonons, since the highest phonon energy in STO is about 0.1 eV, neither by midgap impurity levels, which would be surely saturated in the investigated high excitation density regime. On the contrary, the lattice relaxation due to the formation of polarons can account for the observed Stokes shift. Intrinsic lattice defects can play a crucial role too, since they can enhance to local lattice polarizability, allowing a polaron-like self-trapping of the charge carriers.

The UD kinetics is typical of some kind of bound excitations, or excitons. Such excitation can be defect-induced or not. In the second case we have the self-trapped vibrionic exciton (STVE) we saw in the previous Chapters. The STVE was claimed to account for the 2.4 eV band in some works, and it could be a possible candidate to explain our results.

Let us now speak about the model of the spectral temperature dependence. In this model, the "edge shift" effect is due to the variation of the effective chemical potential with the temperature. The chemical potential value is set by the conservation law of the number of charge carriers. In the investigated temperature range, only the last tail of the Fermi function is observed. Since the population is given by the product between this tail and the density of state of the conduction band (electrons) or the valence band (holes), this makes some difference between the electron and hole populations. It is known, indeed, that the conduction band in STO is quite flat, and thus the density of states is very large, while the density of states of the valence band, which has a usual quadratic shape, is very much lower. This means that the variation of the chemical potential is different for the electron and hole populations. Starting from these considerations, let us assume that the "edge shift" effect concerns only the electron population.

Secondly, in order to account for the UD and BD spectral similarities, the simplest hypothesis is to assume that there is only one radiative decay channel (the unimolecular one), while the non-radiative channels (bimolecular) can interact with the population of the radiative channel in order to stimulate the unimolecular recombinations. This hypothesis is in contrast with the BD-UD model assumption that the UD and BD populations are not interacting. However, an alternative "stimulated emission" model can be developed, and it was found to fit the data as well as the BD-UD model, or even slightly better in some cases. The "stimulated emission" model is based on the idea that the photoexcited carriers are divided very rapidly into two populations: a small fraction is trapped (or self-trapped) into bound-excitons while the most part is composed of free charges, which have to be regarded as polarons because of the strong polarizability of the STO lattice.

These two populations follow two different decay channels: bound trapped excitons will decay radiatively, following an unimolecular law, while the free polarons

will decay non-radiatively, following a bimolecular law. These populations can be coupled if the UD decay is assisted by the interaction with a free polaron. This is different from an Auger effect, in which the third charge carrier takes the energy excess of the transition. In this case the third charge carrier is subjected to an elastic scattering with the exciton, and these scattering leads to the radiative exciton relaxation. This model results in the following rate equations:

$$\frac{d}{dt}n_{UD}(t) = -n_{UD}/\tau_{UD} - \beta n_{UD} n_{BD} \tag{8.9}$$

$$\frac{d}{dt}n_{BD}(t) = -\gamma n_{BD}^2. \tag{8.10}$$

The solution is:

$$n_{BD}(t) = 1/\left(\gamma t + C_1\right)$$
$$n_{UD}(t) = C_2\left(\gamma t + C_1\right)^{-\beta/\gamma} \exp\left(-t/\tau_{UD}\right),$$

where $C_{1,2}$ are two integration constants which can be found from the usual initial conditions $n_{UD,BD}(0) = k_{UD,BD}U$. The PL intensity is given, now, by the $n_{UD}(t)$ population alone:

$$I(t) = -Q_{UD}\frac{d}{dt}n_{UD} = \frac{Q_{UD}n_{UD}(t)}{\tau_{UD}} + Q_{UD}\beta n_{UD}(t)n_{BD}(t),$$

and, thus

$$I(t) = \left[\frac{Q_{UD}k_{UD}U}{\tau_{UD}\left(1 + t/\tau_{BD}\right)^{\beta/\gamma}} + \frac{\beta Q_{UD}k_{UD}k_{BD}U^2}{\left(1 + t/\tau_{BD}\right)^{\beta/\gamma+1}}\right]\exp(-t/\tau_{UD}).$$

Although it is not equivalent to the BD-UD model, the "stimulated emission" model resembles the BD-UD one in the limit $\beta \ll \gamma$, and the model was found to correctly reproduce the data within this hypothesis. Also in this model, the BD term scales as U^2 and the UD term scales as U. The main advantage of this model is to easily explain why the BD and UD channels have the same spectrum.

Besides this, we have to account for the "edge shift" effect. Why is it present in pure samples and not in doped ones? Looking at Fig 8.29 a possible explanation can be found: starting from the left, we can see the UV excitation, which creates the $e - h$ pair. The pair can be bound near a lattice defect as a trapped exciton. The high saturation threshold seems to indicate that the trap levels can be photoinduced. The same trap can present two distinct levels, with two different UD transitions, which are indicated with blue and green arrows, but it is also possible that we have to deal with two distinct kind of traps. In this case it seems unrealistic that many features are so similar in so different kind of samples. The UD transition is stimulated by the interaction with free pairs which can recombine non-radiatively (dotted arrow). The measured energies (2.8 and 2.4 eV, respectively) are related to the gap between e and h levels, but they are independent of the absolute positions of the electron and hole levels. This position depends on the kind of traps which are present in the material. Let us assume that, in Nb doped samples, the niobium

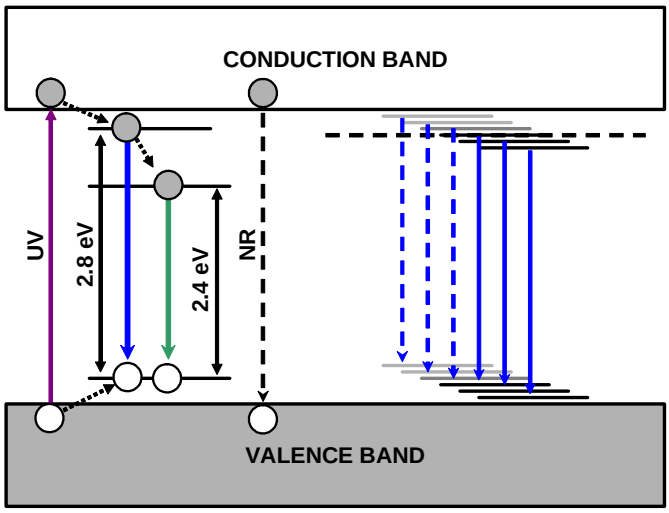

Figure 8.29: The proposed PL microscopic model. The fundamental scheme of the recombination levels is shown in the case of a Nb doped material (left side), and of pure material (right side). UV is the excitation light, NR is a non-radiative channel.

atoms force the e and h levels to have a well defined energy, as depicted on the left side of Fig 8.29. When the temperature increases, nothing changes in this picture but the non-radiative channels effectiveness, as results from the temperature yields behaviour as well as the time and yield activation energies.

In pure samples, the situation can be different, since there is not a "special" trap center (the niobium atoms in case of Nb samples). The absolute energies of the bound-excitons can be spreaded, leading to the situation depicted on the right side of Fig 8.29. When the temperature increases, a certain fraction of the highest electron levels (shown in gray above the dotted line in the figure) is emptied by thermal fluctuations, and, thus, an increasing fraction of excitons are destroyed. This can lead to the observed "edge-shift" effect.

Let us now compare our model with the one proposed by Kan and coworkers in Fig 8.30 (ref [82]). First of all, let us note that the 3.2 eV band (NBE band, in the notation of Mochizuki) is not present in our measurements, probably since its frequency lies in the filtered frequency range. We will not speak, thus, about the transition depicted in Fig 8.30 b). The main discrepancy between our results and what reported in ref [82] is that we observed a significant PL yield from pure samples, while the authors of ref [82] found almost no emission from them. We can ascribe this difference to two experimental conditions: the intensity regime (a CW laser with a flux of 5 W cm^{-2} was used in ref [82]) or the excitation wavelength (325 nm). Further measurements will help to understand which of them could be the more relevant one.

Looking at the a) and c) parts of Fig 8.30, another interesting hypothesis (sketched in Fig 8.31) can be formed. In this alternative framework, it is no longer needed to have some *ad hoc* levels to obtain the observed PL bands: one can assume only that

a certain fraction of the photoexcited carriers goes into an in-gap level placed at 0.4 eV below the conduction band (electrons) and above the valence band (holes). This shift could be related possibly with the lattice relaxation due to the formation of small polarons. The main interest of this model is that it could explain the BD-UD mixed kinetics without requiring the "stimulated emission" model, since each PL band would be filled (or emptied) following a bimolecular process due to the conduction and valence band mobile carriers and an unimolecular one, due to the formation of a polaron exciton, whose binding energy is 2.4 eV. The presence of a lower saturation threshold of the green band with the carrier density, as shown in the previous sections, suggests that the polaron exciton can be not really self-trapped, but it can be formed preferentially near a lattice defect rather than a real trap level.

On the other hand, the main disadvantage of this model is the difficulty in explaining the "edge-shift" effect.

At the moment, we have not enough informations to discriminate between these and several other possible models.

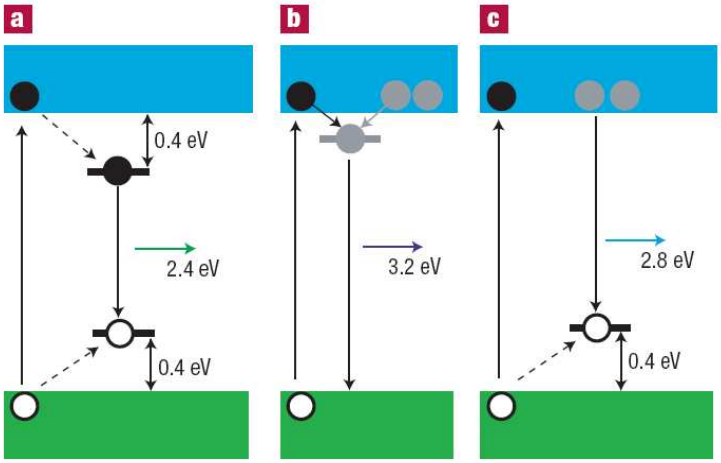

Figure 8.30: The recombination mechanism as proposed by Kan and coworkers [82].

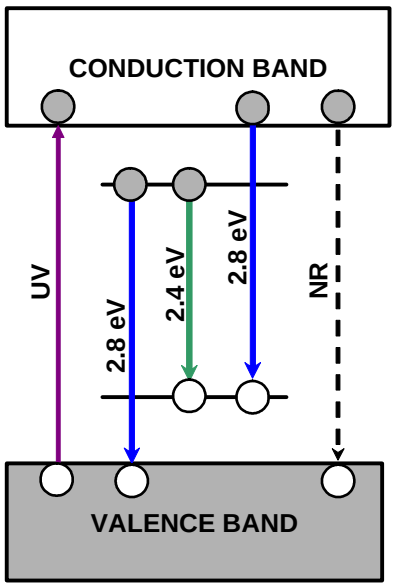

Figure 8.31: An alternative model for the microscopic recombination mechanism.

Appendix A

Brief recall on the Group Theory.

In this Appendix, some elements of the Group Theory will be exposed (without the proofs), starting from the basic definitions and arriving to the relations between a group, its irreducible representations and the characters table. The aim of this Appendix is to give those tools which can be useful for the reading of Ch. 3.

A.1 Finite Groups Theory.

A.1.1 Starting definitions.

A finite set of elements A, B, C, ... from a finite group $\mathcal{G}$ when the following conditions are satisfied:

1. The product between two generic elements of the group is still an element of the group: $AB = C\epsilon\mathcal{G}$.
2. The product is associative: $(AB)C = A(BC)$.
3. It exists the neutral element, called E (identity), and the product between E and each element of the group coincides with that element: $EA = AE = A$.
4. For each generic element A, it exists the inverse element: $A^{-1} : AA^{-1} = A^{-1}A = E$.

The product is not in general commutative: $AB \neq BA$. When it is, the group is called "abelian".

An example of a group is the set of permutation of three elements $P(3)$, made by $3! = 6$ elements we can list as follows:

$$E = \begin{pmatrix} 1 & 2 & 3 \\ 1 & 2 & 3 \end{pmatrix} \quad A = \begin{pmatrix} 1 & 2 & 3 \\ 2 & 1 & 3 \end{pmatrix} \quad B = \begin{pmatrix} 1 & 2 & 3 \\ 1 & 3 & 2 \end{pmatrix}$$
$$C = \begin{pmatrix} 1 & 2 & 3 \\ 3 & 2 & 1 \end{pmatrix} \quad D = \begin{pmatrix} 1 & 2 & 3 \\ 3 & 1 & 2 \end{pmatrix} \quad F = \begin{pmatrix} 1 & 2 & 3 \\ 2 & 3 & 1 \end{pmatrix}$$

A group is identified by its product table. The following table, for instance, is associated to the permutation group $P(3)$:

$P(3)$	E	A	B	C	D	F
E	E	A	B	C	D	F
A	A	E	D	F	B	C
B	B	F	E	D	C	A
C	C	D	F	E	A	B
D	D	C	A	B	F	E
F	F	B	C	A	E	D

A.1.2 Basic definitions and fundamental theorems.

- **Order or dimension of the group:** is the number of the elements of the group. If the number of the elements is infinite, the group is called Infinite Group, but the Infinite Group Theory will not be faced here.
- **Subgroup:** is the set of elements of a group which preserves its properties. The order of a subgroup is always a divisor of the order of the group. A subgroup always contains, of course, the identity element E.
- **Rearrangement theorem:** if E, A_1,...,A_h are the element of a finite group, being A_k a generic element, the set A_kE, A_kA_1,...,A_kA_h contains each element only once. Looking at the product table, it means that the elements will be rearranged in such a way to occur along each row or column without repetitions.
- **Conjugation and classes:** an element B is called "conjugate" of the element A if an element of the same group X such that $B = XAX^{-1}$ exists. A "class" is the set of all elements which can be obtained by conjugation, starting from a given element. Is clear that E forms a class by itself. Moreover, in every abelian group, each element is auto-conjugated, i.e. forms a class by itself.
- **Isomorphic Groups and representations:** two groups are "isomorphic" if they have the same order and a one-to-one correspondence between the elements that preserves the product operation exists. This implies that all isomorphic groups are represented by the same product table, in which all properties of the group is included. Thus, a "representative" group can be choose. In particular, it is possible to choose a square matrix set, the so-called "representation" of the group. Of course, the representation of a given group is not unique.
- **Irreducible representations:** if the matrices of a given representation can be "blocked", i.e. written as made of several diagonal sub-matrices, is called "reducible", otherwise it is called "irreducible". An irreducible representation cannot be given in terms of lower dimension representations.
- **Wonderful Orthogonality Theorem (WOT):** if two irreducible representations Γ_1 and Γ_2 are not equivalent, i.e. not corresponding to a pure coordinate transformation, being $\mathcal{D}^{(l_1)}(R)$ and $\mathcal{D}^{(l_2)}(R)$ their matrices relative to a

generic element R of the group $\mathcal{G}$ of dimension h, the following orthogonality relation holds:

$$\sum_R D^{(l_2)}_{\mu\nu}(R)\, D^{(l_1)}_{\nu'\mu'}\left(R^{-1}\right) = \frac{h}{l_1}\,\delta_{\Gamma_1,\Gamma_2}\delta_{\mu,\mu'}\delta_{\nu,\nu'}.$$

It can be proved that $D^{(l_1)}_{\nu'\mu'}\left(R^{-1}\right) = D^{(l_1)*}_{\nu'\mu'}(R)$, where the star $*$ indicates the complex conjugate. From this, generalizing the index of the representation from 1 and 2 to j and j', we have:

$$\sum_R D^{(l_j)}_{\mu\nu}(R)\, D^{(l_{j'})*}_{\nu'\mu'}(R) = \frac{h}{l_j}\,\delta_{j,j'}\delta_{\mu,\mu'}\delta_{\nu,\nu'}.$$

This orthogonality relationship, the so-called "Wonderful theorem" (WOT), deserves a brief comment. It is an orthogonality relation between $h-$dimensional vectors:

$$V^{(l_j)}_{\mu\nu} = \left[D^{(l_j)}_{\mu\nu}(A_1), ..., D^{(l_j)}_{\mu\nu}(A_h)\right].$$

The indices l_j , μ and ν identify a particular vector. Fixed l_j, there are l_j^2 orthogonal vectors (by varying μ and ν), and they are, in turn, orthogonal to the $l_j'^2$ vectors with $l_j' \neq l_j$. Since the whole number of independent vectors is h, the inequality $\sum_j l_j^2 \leq h$ must hold true. Actually, it is possible to prove that $\sum_j l_j^2 = h$, and, thus, to introduce a very strong relationship between the number of irreducible representations and the dimension of the group.

- **Characters:** the "character" $\chi(R)$ of a matrix representation $\mathcal{D}(R)$, associated with a symmetry operator R, is the track of the element associated matrix. Since the track is unchanged under a coordinate transformation, the character can identify a class.

- **Wonderful Orthogonality Theorem for characters:** when a group is divided into its classes, the WOT can be written, for the characters of those classes, as follows:

$$\sum_k N_k\, \chi^{(l_j)}(\mathcal{C}_k)\left[\chi^{(l_{j'})}(\mathcal{C}_k)\right]^* = h\,\delta_{j,j'},$$

where $\mathcal{C}_k$ and N_k is the number of elements of the class and k is the class index. Moreover, it is possible to prove that two representations are equivalent if and only if they have the same characters.

- **Reduction of a reducible representation:** it is possible to prove that the reduction of a representation into irreducible representations is unique. The relationship between the reducible representation characters $\chi(\mathcal{C}_k)$ and the irreducible ones $\chi^{(l_j)}(\mathcal{C}_k)$ is:

$$\chi(\mathcal{C}_k) = \sum_j a_j\, \chi^{(l_j)}(\mathcal{C}_k),$$

where j denotes the irreducible representation index.

The coefficients a_j are the number of times in which the j-th representation is present in the blocking of the reducible representation. Their values are given by:

$$a_j = \frac{1}{h} \sum_k N_k \left[\chi^{(l_j)}(\mathcal{C}_k) \right]^* \chi(\mathcal{C}_k).$$

- **Number of irreducible representations:** it is possible to prove that the number of irreducible representations is equal to the number of classes.
- **Second orthogonality relationship for characters:** the sum over all possible irreducible representations leads to a new orthogonality rule for characters of different classes:

$$\sum_j \chi^{(l_j)}(\mathcal{C}_k) \left[\chi^{(l_j)}(\mathcal{C}_{k'}) \right]^* N_k = h\, \delta_{k,\,k'}.$$

A.1.3 Characters table.

With this tools, we can now build the characters table, i.e. a table where the rows are indexed by the irreducible representations associated to the group and the columns are indexed by the different classes of the group. Note that the two orthogonality theorems becomes orthogonality relations between rows (the first) and columns (the second).

Let us now summarize the rules to build this table:

1. The number of irreducible representations is equal to the number of classes. The classes can be taken directly by the product table. In general, the classes are associated with the symmetry operators.
2. The dimension of an irreducible representation can be found with the rule $\sum_j l_j^2 = h$.
3. The identity representation, i.e. the representation made by monodimensional identical unitary matrices, is always present, since it is clear that this representation satisfies all properties of any group described in the product table. Thus, in the character table there is always a row made by only the number 1.
4. The first column of the table is the track of the identity matrix, and, thus, each element of that column it is equal to the dimension of the relative representation.
5. By the application of the WOT between the first row and the others, the characters of the irreducible representations different from the identity will follow the rule:

$$\sum_k N_k \chi^{(l_j)}(\mathcal{C}_k) = 0.$$

6. The WOT is a normalization relation too:
$$\sum_k \chi^{(l_j)}(\mathcal{C}_k) \left[\chi^{(l_j)}(\mathcal{C}_k)\right]^* N_k = \sum_k N_k |\chi^{(l_j)}(\mathcal{C}_k)|^2 = h.$$

7. In the same way, working on columns with the second orthogonality relationship, and keeping in mind that, for the class of E, the respective character is equal to the dimension of the representation ($\chi^{(l_j)}(E) = l_j$), we have the following relations:
$$\sum_j l_j \chi^{(l_j)}(\mathcal{C}_k) l_j = 0 \quad \text{and} \quad \sum_j |\chi^{(l_j)}(\mathcal{C}_k)|^2 = \frac{h}{N_k}.$$

As an example, the following classes belong to the permutation group $P(3)$: $\mathcal{C}_1 = \{E\}$, $\mathcal{C}_2 = \{A, B, C\}$, $\mathcal{C}_3 = \{D, F\}$. With the rules just showed, it is easy to find that the characters table of this group is:

$P(3)$	$\mathcal{C}_1$	$3\mathcal{C}_2$	$2\mathcal{C}_3$
Γ_1	1	1	1
Γ_1'	1	-1	1
Γ_2	2	0	-1

A.2 Symmetry Groups.

A.2.1 Base functions.

Every physical system have a finite number of symmetries. It is, thus, possible to associate it with a finite group structure, which will collect the whole number of its symmetry operations, i.e. it is a complete set. One has to be sure that the set is really complete: for instance, in the hydrogen atom study, the spin-orbit interaction is not negligible at all. A symmetry operation R acts on a physical system by moving its points in such a way to place every point into an equivalent one. If a function is defined into a geometrical space, being $\vec{r}$ the generic position vector, the same considerations can be made when the symmetry operation acts on this function. Let us think, for instance, to the rotations: it is clear that a rotation of an angle α around an axis is equivalent to the rotation of an angle $-\alpha$ of the coordinate system, i.e. of the space in which the function is defined. Thus, a symmetry operation R which brings a function $f(\vec{r})$ into the function $f'(\vec{r})$ can be expressed as:
$$f(\vec{r}) \xrightarrow{R} f'(\vec{r}) = f(R^{-1}\vec{r}).$$

We can use a set of functions $f_1, f_2 ..., f_n$ as a base for a group representation if the following relationship is satisfied:
$$\begin{pmatrix} f_1 \\ f_2 \\ \vdots \\ f_n \end{pmatrix} \xrightarrow{R} \begin{pmatrix} f_1' \\ f_2' \\ \vdots \\ f_n' \end{pmatrix} = \Gamma(R) \begin{pmatrix} f_1 \\ f_2 \\ \vdots \\ f_n \end{pmatrix}.$$

$\Gamma(R)$ is the group representation in the n-dimensional base $f_1, f_2 ..., f_n$.

A.2.2 Wave-functions.

Let us suppose to be interested in the symmetry properties of the wave-functions which solves the following Schrödinger equation :

$$\hat{\mathcal{H}}\psi = E\psi.$$

Let R be a symmetry operation of the system. Since R transforms the system into an equivalent one, we expect that the associated operator $\hat{\mathcal{R}}$ commutes with the Hamiltonian. This has some important consequences for the eigenfunctions of $\hat{\mathcal{H}}$:

1. Not-degenerate case: $\hat{\mathcal{H}}\psi_i = E_i\psi_i$.

   By the application of the commutation property, we have:

   $$\hat{\mathcal{H}}\left(\hat{R}\psi_i\right) = \hat{R}\hat{\mathcal{H}}\psi_i = \hat{\mathcal{R}}E_i\psi_i = E_i\left(\hat{\mathcal{R}}\psi_i\right)$$

   The function $\hat{R}\psi_i$ is still an eigenfunction of the Hamiltonian and this means that ψ_i is a base function for a monodimensional irreducible representation of the group.

2. k-degenerate case: $\hat{\mathcal{H}}\psi_{il} = E_i\psi_{il} \quad \forall \quad \psi_{i,1\ldots k}$.

   As before, we have

   $$\hat{\mathcal{H}}\left(\hat{R}\psi_{il}\right) = E_i\left(\hat{\mathcal{R}}\psi_{il}\right).$$

   $\hat{\mathcal{R}}\psi_{il}$ is an eigenstate of the k-degenerate subspace relative to E_i, and, thus, it can be expanded over the eigenfunctions base $\{\psi_{il}\}$, i.e. $\hat{R}\psi_{il} = \sum_{s=1}^{k} \mathcal{D}_{sl}(R)\psi_{is}$. In this case, the k-dimensional $\Gamma(R)$ representation is defined by the $k \times k$ matrices $\mathcal{D}(R)$ in the eigenfunctions base, and it can be proved that it is an irreducible one.

To summarize, the eigenfunction of the Hamilton operator are base functions for the representations of the symmetry group of the physical system, ruled by the Hamiltonian itself. The fixed energy subspaces are associated with the group irreducible representations whose dimension is equal to the degeneration of the energy level. Thus, the irreducible representation $\Gamma^{(l_i)}$ is associated with the l_i-dimensional subspace of energy E_i. The matrices of this representation $\mathcal{D}^{(l_i)}(R)$ can be obtained using the eigenfunctions as base functions.

A.2.3 Base functions orthogonality.

Let us consider two base functions of the same or different irreducible representations: such representations will be, thus, orthogonal. The proof is that, let $\psi_{\alpha}^{(l_i)}$ and $\psi_{\alpha'}^{(l'_i)}$ be the base functions of two Γ and Γ' irreducible representations, with l_i and l'_i dimensions respectively, the following relationships holds true:

$$\hat{\mathcal{R}}\psi_{\alpha}^{(l_i)} = \sum_{j=1}^{l_i} \psi_{j}^{(l_i)} \mathcal{D}_{j,\alpha}^{(l_i)}(R) \qquad ; \qquad \hat{\mathcal{R}}\psi_{\alpha'}^{(l'_i)} = \sum_{j'=1}^{l'_i} \psi_{j'}^{(l'_i)} \mathcal{D}_{j',\alpha'}^{(l'_i)}(R).$$

The scalar product $\left(\psi_{\alpha}^{(l_i)}\,,\,\psi_{\alpha'}^{(l'_i)}\right)$ does not depend of the coordinate system, so that we have

$$\left(\psi_{\alpha}^{(l_i)}\,,\,\psi_{\alpha'}^{(l'_i)}\right) = \left(\hat{\mathcal{R}}\psi_{\alpha}^{(l_i)}\,,\,\hat{\mathcal{R}}\psi_{\alpha'}^{(l'_i)}\right) = \sum_{j,j'} \mathcal{D}_{j,\alpha}^{(l_i)}(R)^* \mathcal{D}_{j',\alpha'}^{(l'_i)}(R) \left(\psi_{j}^{(l_i)}\,,\,\psi_{j'}^{(l'_i)}\right),$$

with R a generic operation. Taking the average value over the whole set of coordinate transformations of the h symmetries of the group, we have

$$\left(\psi_{\alpha}^{(l_i)}\,,\,\psi_{\alpha'}^{(l'_i)}\right) = \frac{1}{h} \sum_{j,j'} \sum_{R} \mathcal{D}_{j,\alpha}^{(l_i)}(R)^* \mathcal{D}_{j',\alpha'}^{(l'_i)}(R) \left(\psi_{j}^{(l_i)}\,,\,\psi_{j'}^{(l'_i)}\right).$$

By means of the WOT theorem, we arrive, finally, to the desired orthogonality relationship:

$$\left(\psi_{\alpha}^{(l_i)}\,,\,\psi_{\alpha'}^{(l'_i)}\right) = \frac{1}{l_i} \delta_{l_i,l'_i} \delta_{\alpha,\alpha'} \sum_{j=1}^{l_i} \left(\psi_{j}^{(l_i)}\,,\,\psi_{j'}^{(l'_i)}\right).$$

A.2.4 Direct product of two irreducible representations.

The direct product between two irreducible representations is the first step in order to study the selection rules. Let us start with the definition of the matrix direct product $A_{n\times n} \otimes B_{m\times m} = C_{l\times l}$ where $l = m \cdot n$ and the matrix elements are

$$A_{ij} B_{kl} = C_{ik,jl}.$$

This relationship defines the direct product between the matrices of two different representations. It can be proved that the product between two representations of the same group, is still a representation of that group, as well as that the direct product of two irreducible representations will be a reducible one.

The characters of the direct product.

It can be proved that the direct product of two representations $\Gamma^{(\lambda)}$ and $\Gamma^{(\mu)}$ of the same group is the algebraic product of the characters of these representations:

$$\chi^{(\lambda\otimes\mu)}(R) = \chi^{(\lambda)}(R)\chi^{(\mu)}(R).$$

Since the product will be, in general, reducible, one can expand its characters on the irreducible representations characters:

$$\chi^{(\lambda\otimes\mu)}(R) = \chi^{(\lambda)}(R)\chi^{(\mu)}(R) = \sum_{\nu} a_{\lambda\mu\nu} \chi^{(\nu)}(R),$$

in which the coefficients $a_{\lambda\mu\nu}$ are given by:

$$a_{\lambda\mu\nu} = \frac{1}{h}\sum_{C_\alpha} N_{C_\alpha}\left[\chi^{(\lambda)}(C_\alpha)\chi^{(\mu)}(C_\alpha)\right]\chi^{(\nu)}(C_\alpha)^*,$$

where C_α indicates the group class and N_{C_α} its dimension.

A.3 Selection rules: IR and Raman transitions.

Let us consider the generic interaction $\mathcal{H}'$, which acts on a system described by the Hamiltonian $\mathcal{H}$, whose eigenstates are $\psi_\alpha^{(j)}$. We can, now, use the mathematical background achieved in the previous sections, in order to obtain the selection rules for the matrix elements $(\psi_\alpha^{(l'_i)}, \mathcal{H}'\psi_\beta^{(l_i)})$. This elements are transformed as scalars, i.e. they have to transform as the total-symmetric representation of the group. This request implies that the direct product of the two representations which corresponds to the matrix elements have to contain the total-symmetric representation, as shown in the following.

A.3.1 Radiation-matter interaction.

We want to stress, now, our attention on the roto-vibrational modes of a molecule under the presence of an electromagnetic wave. The interaction energy of the molecule (being $\vec{\mu}$ its dipole moment), excited by the incident radiation $\vec{E}$, is given by the perturbative term:

$$\mathcal{H}' = -\vec{E}\cdot\vec{\mu}.$$

There are two kinds of dipole transitions: infrared (IR) and Raman, and they are related with two different definitions of the dipole moment $\vec{\mu}$.

IR transitions.

The absorption spectrum of the roto-vibrational states of a molecule, is in the infrared region. In this case, we can define $\vec{\mu}$ as follows:

$$\vec{\mu}_{IR} = \sum_i q_i\,\vec{r}_i, \tag{A.1}$$

where q_i is the charge and r_i is the displacement from the equilibrium position of the $i-$th nucleus.

Let us, now, consider the electric-dipole transitions, as described by the matrix element $(\psi_\alpha^{(f)}, \mathcal{H}'\psi_\beta^{(i)})$, where the indices f and i indicates the final and initial state. Let $\Gamma^{(f)}$ and $\Gamma^{(i)}$ be the irreducible representations associated with that states. In order to have a not-vanishing matrix element, the total-symmetric representation have to be present in the direct product $\Gamma^{(f)}\otimes\Gamma^{(\mu)}\otimes\Gamma^{(i)}$, where $\Gamma^{(\mu)}$ is the electric-dipole representation. In order to have its characters, it is sufficient to note that, from Eq. A.1, the IR-dipole moment is transformed as a position vector $\vec{r}$, so that its components μ_x, μ_y and μ_z are transformed as the base functions x, y and z.

The character $\chi(R)$ of the perturbation $\Gamma^{(\mu_{IR})}$ will be, thus, the character of the representation written on the base functions x, y, z, which can be found in the tables.

Raman transitions.

For Raman transitions, the dipole moment is given by:

$$\vec{\mu} = \widehat{\alpha} \cdot \vec{E},$$

where $\widehat{\alpha}$ is the dielectric polarizability tensor. The induced momentum $\vec{\mu}$ can be expanded around the equilibrium position q_0 of the molecule (let us consider, for simplicity, only one dimension):

$$\mu = \alpha_0 E + \left(\frac{d\alpha}{dq}\right)_0 qE + \frac{1}{2}\left(\frac{d^2\alpha}{dq^2}\right)_0 q^2 E + ...$$

If the incident radiation is $E_0 \cos(\omega t)$ and only the first order of the series is considered, we have:

$$\begin{aligned}\mu &= \alpha_0 E_0 \cos(\omega t) + \left(\frac{d\alpha}{dq}\right)_0 q_0 \cos(\omega_0 t) E_0 \cos(\omega t) = \\ &= \alpha_0 E_0 \cos(\omega_0 t) + \left(\frac{d\alpha}{dq}\right)_0 q_0 \left\{\cos[(\omega - \omega_0)t] + \cos[(\omega + \omega_0)t]\right\},\end{aligned}$$

where ω_0 is the proper frequency of the vibrational mode and ω is the radiation frequency. The first term is the so-called Rayleigh radiation, while the second and the third are the Stokes and anti-Stokes terms, respectively.

In general, we can expand the dielectric tensor around the equilibrium position along a vibrational mode of frequency ω_v as follows:

$$\widehat{\alpha} = \widehat{\alpha}_0 + \widehat{\Delta\alpha} \cos\omega_v t,$$

and get the dipole moment $\vec{\mu}$:

$$\vec{\mu} = \left(\widehat{\alpha}_0 + \widehat{\Delta\alpha} \cos\omega_v t\right) \cdot \vec{E}_0 \cos\omega t = \widehat{\alpha}_0 \cdot \vec{E}_0 \cos\omega + \frac{\widehat{\Delta\alpha}}{2} [\cos(\omega - \omega_v) + \cos(\omega + \omega_v)] \cdot \vec{E}_0.$$

The Raman perturbative Hamiltonian, thus, is:

$$\mathcal{H}'_{RAMAN} = -\vec{\mu} \cdot \vec{E} = -\frac{\widehat{\Delta\alpha}}{2} \vec{E}\vec{E} cos(\omega \pm \omega_v).$$

Such perturbation is characterized by the so-called Raman tensor $\widehat{\Delta\alpha}$, which is symmetric and contains the symmetries of the molecule states. Let us see how the Raman tensor elements are transformed under a symmetry operation:

$$\widehat{\Delta\alpha} = \begin{pmatrix} \alpha_{11} & \alpha_{12} & \alpha_{13} \\ \alpha_{21} & \alpha_{22} & \alpha_{23} \\ \alpha_{31} & \alpha_{32} & \alpha_{33} \end{pmatrix},$$

$$\alpha'_{ij} = \sum_{kl} R_{ik} R_{jl} \alpha_{kl},$$

and thus:

$$\alpha'_{xx} = R^2_{xx}\alpha_{xx} + R^2_{xy}\alpha_{yy} + R^2_{xz}\alpha_{zz} + 2R_{xx}R_{xy}\alpha_{xy} + 2R_{xx}R_{xz}\alpha_{xz} + 2R_{xy}R_{xz}\alpha_{yz}$$

Let us compare the last equation with the transformation of the function x^2:

$$\begin{aligned}\left(x'\right)^2 &= \left(R_{xx}x + R_{xy}y + R_{xz}z\right)^2 = \\ &= R^2_{xx}\,x^2 + R^2_{xy}\,y^2 + R^2_{xz}\,z^2 + 2R_{xx}R_{xy}\,xy + 2R_{xx}R_{xz}\,xz + 2R_{xy}R_{xz}\,yz.\end{aligned}$$

If one repeats the comparison with the other matrix elements, one finds that the Raman tensor components are transformed as the quadratic forms x^2, y^2, z^2, xy, xz, yz.

As in the IR case, the character of the representation $\Gamma^{(\mu)}$ can be found from the characters of the group representation written on the x, y, z base functions. In this base, one has to know the characters of R as well as R^2 operators. Being $\chi(R)$ and $\chi(R^2)$ these characters, it can be proved that

$$\chi(R)_{Raman} = \frac{1}{2}\left[\chi(R)^2 + \chi(R^2)\right].$$

With the Raman characters, one can expand the Raman perturbation representation into the irreducible representations of the group, and find the symmetries of all Raman modes, as seen in Ch. 3.1.6.

Appendix B

Relaxation times.

Nonlinear optical susceptibilities are characteristic features of the material, and, thus, they depend on its electronic and molecular structure. The most suitable tool in order to give a microscopic expression of them is, thus, the Quantum Mechanic. In particular it is convenient to refer to the formalism of the density matrix.

B.1 The density matrix.

Given a pair formed by a statistical ensemble of quantum data of the system $\{|\psi\rangle\}$, and by a classical distribution of probabilities on this ensemble $P_{\{|\psi\rangle\}}$, the density matrix is defined as the average over the whole ensemble of the projection operator:

$$\rho = \overline{|\psi\rangle\langle\psi|}.$$

The mean value of a generic observable is

$$\langle \mathbf{P} \rangle = \overline{\langle\psi|\mathbf{P}|\psi\rangle} = Tr(\rho\mathbf{P}).$$

If the wave-function $|\psi\rangle$ satisfies a Schroedinger equation, with an Hamiltonian H, the density matrix will satisfy the Liouville equation

$$\frac{\partial\rho}{\partial t} = \frac{1}{i\hbar}[\mathcal{H}, \rho].$$

B.2 Longitudinal and transverse lifetimes.

Let us now consider a material system, subjected to a electromagnetic stress, and in contact with a thermal reservoir. The Hamiltonian which describes this system is

$$\mathcal{H} = \mathcal{H}_0 + \mathcal{H}_{int} + \mathcal{H}_{ran},$$

where H_0 is the unperturbed Hamiltonian (being $|n\rangle$ its eigenvectors and E_n its respective eigenvalues), $H_{int} = e\vec{r}\cdot\vec{E}$ represent the interaction with the electromagnetic radiation and H_{ran} accounts for the random perturbation acting on the system because of the thermal reservoir. The Liouville equation, thus, becomes:

$$\frac{\partial\rho}{\partial t} = \frac{1}{i\hbar}[\mathcal{H}_0 + \mathcal{H}_{int}, \rho] + \frac{1}{i\hbar}[\mathcal{H}_{\text{rand}}, \rho] \equiv \frac{1}{i\hbar}[\mathcal{H}_0 + \mathcal{H}_{int}, \rho] + \left(\frac{\partial\rho}{\partial t}\right)_{ril}.$$

The Hamiltonian H_{ran} is, thus, responsible for the relaxation of the system, i.e. for its return, after some times, to the thermal equilibrium. Since the eigenvectors set $|n\rangle$ is a complete set, it is possible to express the wave-function of the system $|\psi\rangle$ as a linear combination of eigenstates: $|\psi\rangle = \sum_n a_n|n\rangle$. In this base, it is possible to give a physical interpretation of the density matrix elements. The diagonal elements $\rho_{nn} = \langle n|\rho|n\rangle = |a_n|^2$ represent the populations of the eigenvectors $|n\rangle$, while the out-diagonal elements $\rho_{nn'} = \langle n|\rho|n'\rangle = \overline{a_n a^*_{n'}}$ give informations on the coherence of the superposition between the states $|n\rangle$ and $|n'\rangle$; in the thermal equilibrium, the elements $\rho^{(0)}_{nn}$ are given by the Boltzmann distribution, while all the out-diagonal elements vanish (strictly incoherent superposition): $\rho^{(0)}_{nn'} = 0 \qquad \forall n \neq n'$.

If $W_{n\to n'}$ is the transition rate from the state $|n\rangle$ to the state $|n'\rangle$, due to H_{ran}, the time-variation of the diagonal elements is given by

$$\left(\frac{\partial}{\partial t}\rho_{nn}\right)_{ril} = \sum_{n'} \left[W_{n\to n'}\rho_{n'n'} - W_{n'\to n}\rho_{nn}\right],$$

and, since in the thermal equilibrium it holds the following expression

$$\frac{\partial \rho^{(0)}_{nn}}{\partial t} = \sum_n \left[W_{n\to n'}\rho^{(0)}_{n'n'} - W_{n'\to n}\rho^{(0)}_{nn}\right] = 0,$$

one obtains

$$\frac{\partial}{\partial t}\left[(\rho_{nn})_{ril} - \rho^{(0)}_{nn}\right] = \sum_n \left[W_{n\to n'}\left(\rho_{n'n'} - \rho^{(0)}_{n'n'}\right) - W_{n'\to n}\left(\rho_{nn} - \rho^{(0)}_{nn}\right)\right].$$

In most cases, the equation which rules the variation of the population compared to the equilibrium population $(\Delta\rho)_n = (\rho_{nn})_{ril} - \rho^{(0)}_{nn}$ can be written as

$$\frac{\partial}{\partial t}(\Delta\rho)_n = -\left(\frac{1}{T_1}\right)_n (\Delta\rho)_n .$$

The relaxation mechanism of the out-diagonal elements are quite more complex, but we can expect an exponential decay of the form

$$\left(\frac{\partial}{\partial t}\rho_{nn'}\right)_{ril} = -\left(\frac{1}{T_2}\right)_{nn'} \rho_{nn'}.$$

The characteristic times T_1 and T_2 are called respectively longitudinal and transverse relaxation times.

Appendix C

Brief reminder on superconductivity.

C.1 Experimental evidence.

The phenomenon nowadays known as "superconductivity" was discovered by H. Kamerling Onnes in 1911, and a first complete theory was proposed in 1957 by Bardeen, Cooper and Schrieffer. It took the name of BCS theory [42]. The first experimental evidence of this phenomenon was that the resistivity as a function of temperature has a quite pronounced "step-like" behaviour in correspondence of a particular temperature in many common metals, as mercury or aluminium. Below that temperature threshold, the resistivity is found to be definitely zero.

To give an idea of the orders of magnitude, suffice it to say that a supercurrent flowed into a superconductive ring for many years, and experimentalist were not able to measure a significant decrease of the charge flow. Magnetic resonance experiments gave a lower limit to the current decay time which is about 10^5 years, while this time was theoretically estimated to be $10^{10^{10}}$ years!

Such an abrupt variation of the resistivity happens below a well precise temperature, the so-called "critical temperature" (T_c), which is of the order of few Kelvin degrees. The critical temperature is a characteristic of the material.

Nevertheless, this is not their unique features. They are also perfect diamagnets, i.e. in the presence of a magnetic field the magnetic induction inside the material is perfectly zero.

Note that this does not descend automatically from the perfect conductivity, which, alone, requires only that the variation of the magnetic flux inside the material has to vanish. In other words, if one inserts a magnetic field inside a superconductor when the temperature is above T_c, and after cools the sample below it, the magnetic field will be expelled outside the sample!

But when the external field exceed a certain limit, the magnetic induction goes abruptly into the material, and, from this moment on, the superconductivity ends and the relationship between the field and the induction will follow a linear behaviour, as happens in normal metals. These are the so-called "type I" superconductors.

Very soon, it was discovered that there is another different behaviour: the ex-

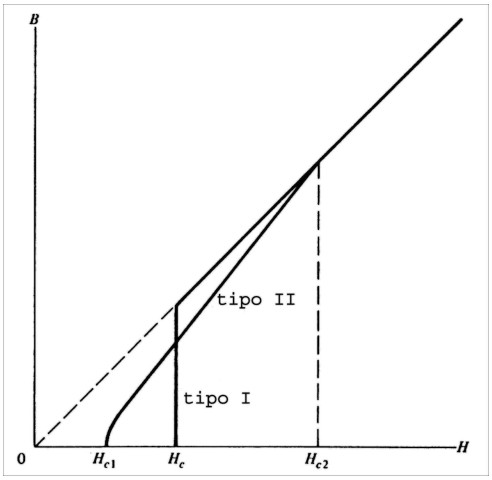

Figure C.1: Magnetic behaviour of type I and type II superconductors [7].

ternal magnetic field can have, actually, two distinct critical values.

The magnetic flux starts to enter the material above a first critical value of the external field H_{c1} and reaches the linear behaviour $B \propto H$ in correspondence of a second critical value H_{c2} (as showed in Fig C.1). Between these two values the magnetic flux lines enter as vortex-like quanta. These current-vortices do not prevent the superconductivity, although the portion of material inside a vortex is not superconductive. The density of the vortices increases as the external magnetic field increases, until it destroys the superconductivity in correspondence of H_{c2}. This kind of materials are called "type II" superconductors.

C.2 Cooper's pairs.

In order to understand these phenomena, it is needed to investigate the microscopic behaviour of the elementary particles inside the crystal lattice. In 1956, Cooper showed that the electronic Fermi sea becomes unstable when even only one pair of bounded electron is formed, and this happens independently from the weakness of the binding energy. The only requirement is that the interaction potential in the Hamilton operator have a negative sign, i.e. it is an attractive potential. The origin of this attractive force was singled out from the electron-phonon interaction, inside the crystal lattice. It is, actually, easy to prove that the Coulomb interaction cannot give in any case, as expected, a negative potential. But a phonon can act as an agent of the interaction between two electrons, giving the birth to a so-called Cooper's pair. Beyond the mathematical formalism, a physical interpretation of this interaction is the following: the first electron induces a polarization inside the lattice, attracting the positive ions, and this excess of positive carriers can attract, in turn, another electron. If this attraction is strong enough to be able to overcome the Coulomb force, the pair will be formed.

The generation of a Cooper's pair is the keystone to understand the physics of

superconductors. Because of its fermion nature, an electron cannot condensate into a Bose-Einstein condensate as a boson particle does. But, since it is possible to prove that a Cooper's pair is already made by two electrons having anti-parallel spins, the total spin of a single pair always vanishes, so that it can be regarded as a boson, and it can condensate, as happens, for instance, for liquid helium.

When the stability of the Fermi sea is broken by the formation of a single pair, the system will evolve until it reaches a new equilibrium. This condition takes place when the binding energy requested for the formation of a new pair vanishes.

One of the most relevant quantities, which characterize a Cooper's pair, is its mean radius, the so-called "coherence length". An easy but rough estimate can be made, starting from the Heisenberg principle: the electrons, whose energy is close to the Fermi energy within $k_B T_c$ (where k_B is the Boltzmann constant), are the most involved in the process, and their kinetic momentum is approximately

$$\Delta p \approx \frac{k_B T_c}{v_F},$$

where v_F is the Fermi velocity. The Heisenberg principle can be written, thus, as follows

$$\Delta x \gtrsim \frac{h}{\Delta p} \approx \frac{h v_F}{k_B T_c},$$

and so

$$\xi_0 = a \frac{h v_F}{k_B T_c,}$$

where ξ_0 is the coherence length and a is a constant close to the unity. This quantity is the analogous of the mean free-path of charge carriers in the non-local electrodynamics of metals. Another fundamental quantity is the so-called "superconductive gap" $\Delta(T)$: it is the minimum energy the single bounded electron needs to break its pair.

Its value is equal to zero when $T = T_c$ and increases rapidly below the threshold until it reaches the value

$$E_g = 2\Delta(0) = 3.528\, k_B T_c$$

when $T \to 0$. E_g is, thus, the pair-breaking energy.

Appendix D

PL best-fit program.

D.1 Main program: Ganasto.

```
clear all
    close all
    clc
    cd savedirectory
    delete *.*
    cd ..
    nomedire='\Intensity';
    cd(nomedire);
    nomefiler='\F1STObs+50Crisposta00000.dat';
    cd('E:\FotoLuminescenza\tempi\Ganasto_old');
    afile=dir(nomedire);
    nfiles=length(afile);
    EAR=1; % EAR=0;
    decisione=0 % 0= measured energies, 1=integral
    temp=[];
    fileind=[];
    for j=1:nfiles
    nomefile=afile(j).name;
    posmis=findstr(nomefile,'mis');
    l=isempty(posmis);
    if l==0
    possegno=findstr(nomefile,'+');
    ll=isempty(possegno);
    if ll==0
    temp1=afile(j).name(possegno:posmis-2);
    temp=[temp str2num(temp1)];
    fileind=[fileind j];
    tit1=strtok(afile(j).name,'+');
    tit=tit1(3:length(tit1));
    elseif ll==1
```

```
possegno=findstr(nomefile,'-');
temp1=afile(j).name(possegno:posmis-2);
temp=[temp str2num(temp1)];
fileind=[fileind j];
tit1=strtok(afile(j).name,'-');
tit=tit1(3:length(tit1))
end
end
end
npunti=length(temp);
[temp_mis,riord]=sort(temp);
fileind=fileind(riord);
energia=temp_mis'*1e-3;
if decisione==1
for kk=1:npunti;
nomefiled=[nomedire,'\',afile(fileind(kk)).name];
dt=dlmread(nomefiled,' ');
d=dt(:,2);
t=dt(:,1)*1e9;
[maxf nmax]=max(d);
nb=fix(2/3*nmax);
bkg=mean(d(1:nb));
d=d-bkg;
dint(kk,1)=trapz(t,d);
end
[energia2,riord2]=sort(dint);
conversione=(sum(dint.*energia))/(sum(dint.^2));
energia=energia2*conversione;
elseif decisione==0
[energia2,riord2]=sort(energia);
energia=energia2;
end
% Initializations
% starting values
tau0start=10;
alpha0=4;
if EAR==1
bamma0=0.2;
end
t0=0.1;
if EAR==0
par1=[tau0start alpha0];
elseif EAR==1
par1=[tau0start alpha0];
end
for kk=1:npunti;
```

```
nomefiled=[nomedire,'\',afile(fileind(kk)).name];
titl(:,kk)=cellstr(strcat(tit,' E = ',num2str(energia(kk)),' mJ'));
titfig(:,kk)=...
cellstr(strcat(tit,'E',num2str(energia(kk)),'mJ','.fig'));
% DATA
dt=dlmread(nomefiled,' ');
sizedt=size(dt);
d=dt(:,2);
n=length(d);
t=dt(:,1)*1e9;
[maxf nmax]=max(d);
nb=fix(2/3*nmax);
bkg=mean(d(1:nb));
d=d-bkg;
dint(kk)=trapz(t,d);
dmax(kk,1)=max(d);
np=2^nextpow2(d);
d=[zeros(1,np-n) d']';
deltat=t(2)-t(1);
t=[t(1)-deltat*(np-n+1)+deltat*(1:np-n) t']';
l1=nb+np-n;
l2=np;
d=d/max(d);
half1=find(d>max(d)/2);
half=half1(1);
tshd=t(half-1)+(t(half)-t(half-1))/...
(d(half)-d(half-1))*(max(d)/2-d(half-1));
if abs(t(half)-tshd)<abs(t(half-1)-tshd);
tshift(kk)=t(half);
else
tshift(kk)=t(half-1);
end
dati(:,kk)=d;
end
rt=dlmread(nomefiler,' ');
tr=rt(:,1)*1e9;
r=rt(:,2);
[maxr nrmax]=max(r);
nb=fix(2/3*nrmax);
bkg=mean(r(1:nb));
r=r-bkg;
if abs(tr(2)-tr(1)-(t(2)-t(1)))>1e-10
msgbox('Attenzione: la base dei...
tempi della funzione risposta e dei dati...
sono diversi','ERRORE');
return
```

```
end
if n>length(r)
r=[r' zeros(1,n-length(r))]';
elseif n<length(r)
msgbox('Attenzione: gli intervalli...
temporali della funzione risposta e...
dei dati sono diversi','ERRORE');
return
end
r=[zeros(1,np-n) r']';
[maxr nrmax]=max(r);
r=r/maxr;
half1=find(r>max(r)/2);
half=half1(1);
tshr=t(half-1)+(t(half)-t(half-1))/...
(r(half)-r(half-1))*(max(r)/2-r(half-1));
r=[r(nrmax:np)' r(1:nrmax-1)']';
tshiftr=0;
dati=dati(:,riord2);
tshift=tshift(riord2);
titl=titl(riord2);
titfig=titfig(riord2);
dint=dint(riord2);
dmax=dmax(riord2);
% CALLING OF THE FIT PROGRAM Gfitflsto
[par,depar,c_mat,dec,chi2,teom,teo1m,teo2m,tshiftnew]=...
Gfitflsto(energia,dati,r,t,tshift,...
tshiftr,l1,l2,titl,titfig,par1,t0,EAR);
chi2s=num2str(chi2);
tau0=par(1);
tau0s=num2str(tau0);
alpha=par(2);
alphas=[num2str(alpha)];
if EAR==1
bamma=0
end
c1=c_mat(1,:)';
c2=c_mat(2,:)';
pcent=.2;
figure(npunti+1)
plot(energia, c1.*dmax,'o:')
xlabel('energy (mJ)')
ylabel('c1 * dmax - coeff ricerca')
title(strcat(' \chi^2 = ',chi2s,' \tau_0 =...
',tau0s,' ns \alpha =',alphas))
axis([0 max(energia)+max(energia)*pcent 0...
```

```
max(c1.*dmax)+max(c1.*dmax)*pcent]);
figure(npunti+2)
plot(energia, c2.*dmax,'o:')
xlabel('energy (mJ)')
ylabel('c2 * dmax - coeff exp')
title(strcat(' \chi^2 = ',chi2s,' \tau_0 =...
',tau0s,' ns \alpha =',alphas))
axis([0 max(energia)+max(energia)*pcent 0...
max(c2.*dmax)+max(c2.*dmax)*pcent]);
figure(npunti+3)
plot(energia, dint,'o:')
xlabel('energy (mJ)')
ylabel('Integral')
title(strcat(' \chi^2 = ',chi2s,' \tau_0 =...
',tau0s,' ns \alpha =',alphas))
axis([0 max(energia)+max(energia)*pcent 0...
max(dint)+max(dint)*pcent]);
figure(npunti+4)
plot(energia, dmax,'o:')
xlabel('energy (mJ)')
ylabel('Maximum')
title(strcat(' \chi^2 = ',chi2s,' \tau_0 =...
',tau0s,' ns \alpha =',alphas))
axis([0 max(energia)+max(energia)*pcent 0...
max(dmax)+max(dmax)*pcent]);
figure(1000)
title(strcat(tit,' \chi^2 = ',chi2s,' \tau_0...
= ',tau0s,' ns \alpha =',alphas))
figure(1001)
title(strcat(tit,' \chi^2 = ',chi2s,' \tau_0...
= ',tau0s,' ns \alpha =',alphas))
cd savedirectory
save results
saveas(npunti+1, 'c1.fig')
saveas(npunti+2, 'c2.fig')
saveas(npunti+3, 'integral.fig')
saveas(npunti+4,'maximum.fig')
saveas(1000, 'global.fig')
saveas(1001, 'semiloglobal.fig')
cd ..
```

D.2 First function: Gfitflsto.

```
function [par,depar,c_mat,dec,chi2...
    ,teom,teo1m,teo2m,tshiftnew]=...
```

```
fitflsto(energia,dati,r,t,tshift,...
tshiftr,l1,l2,titl,titfig,par1,t0,EAR);
% Initialization
i=sqrt(-1);
colors='bgrcmykbgrcmykbgrcmyk';
sized=size(dati);
n=sized(1);
npunti=sized(2);
dt = t(2)-t(1);
deomega=2*pi/(n*dt);
om=((1:n/2+1)'-1)*deomega;
rf=fft(r);
aggiustamenti=10;
while aggiustamenti>0
% FIT PROGRAM CALL
options=optimset('Display','Final',...
'TolX',1e-6,'TolFun',1e-11,...
'MaxFunEvals',10000,'MaxIter',10000);
par=fminsearch('Gchi2sto',par1,...
options,n,l1,l2,t...
,tshift,energia,dati,rf,tshiftr,t0,EAR);
last=length(par);
tau0=par(1);
alpha0=par(2);
if EAR==1
bamma=0;
end
for kk=1:npunti
theta=(1+sign(t-t0-tshift(kk)+tshiftr+dt*1e-9))/2;
if EAR==0
flnorm=theta./(1+energia(kk)*alpha0*...
(t-t0-tshift(kk)+tshiftr)).^2;
flnorm=(theta.*exp(-2*(t-t0-tshift(kk)+tshiftr)/...
tau0))./(1+energia(kk)*alpha0*tau0*...
(1-exp(-(t-t0-tshift(kk)+tshiftr)/tau0))).^2;
elseif EAR==1
flnorm=(theta.*exp((-t+t0+tshift(kk)-tshiftr)/...
tau0)).*(1./(1+energia(kk)*alpha0*...
(t-t0-tshift(kk)+tshiftr)).^(bamma+1));
end
flnormf=fft(flnorm);
flnormfr=rf.*flnormf;
flnormr=real(ifft(flnormfr));
if EAR==0
flexp1=theta.*...
exp((-t+t0+tshift(kk)-tshiftr)/tau0);
```

```
elseif EAR==1
flexp1=(theta.*...
exp((-t+t0+tshift(kk)-tshiftr)/tau0)).*...
(1./(1+energia(kk)*alpha0*...
(t-t0-tshift(kk)+tshiftr)).^(bamma));
end
flexpf1=fft(flexp1);
flexpf=rf.*flexpf1;
flexp=real(ifft(flexpf));
A(:,1)=flnormr;
A(:,2)=flexp;
c=A(l1:l2,:)\dati(l1:l2,kk);
teo=A*c;
teom(:,kk)=teo;
chiquadro_mat(kk)=((norm(teo(l1:l2)...
-dati(l1:l2,kk)))^2);
c_mat(:,kk)=c;
teo1=c(1)*flnormr;
teo1m(:,kk)=teo1;
teo2=c(2)*flexp;
teo2m(:,kk)=teo2;
end
chiquadro=sum(chiquadro_mat)/...
(npunti*(l2-l1+1-length(c))-last);
depar=zeros(last,1);
dec=0;
chi2=chiquadro;
tshiftold=tshift;
for kk=1:npunti
d=dati(:,kk);
half1=find(d>max(d)/2);
half=half1(1);
tshd=t(half-1)+(t(half)-t(half-1))/...
(d(half)-d(half-1))*...
(max(d)/2-d(half-1));
teo=teom(:,kk);
half1=find(teo>max(d)/2);
halfteo=half1(1);
tshdteo=t(half-1)+(t(half)-t(half-1))/...
(teo(half)-teo(half-1))*...
(max(teo)/2-teo(half-1));
Dt=tshd-tshdteo;
tshift(kk)=tshift(kk)+dt*round(Dt/dt);
end
aggiustamenti=length(find([tshiftold-tshift]))
end
```

```
for kk=1:npunti
teo1=teo1m(:,kk);
teo2=teo2m(:,kk);
teo=teom(:,kk);
figure(kk);
plot(t,dati(:,kk),'.r',t,teo1,'...
-b',t,teo2,'-m',t,teo,'-k');
legend('data', 'bimoulecular', ...
'unimoulecular', 'best fit')
xlabel('Time (ns)');
ylabel('Normalized Signal');
tit=titl(kk);
titolfig=char(titfig(kk));
title(tit);
t1=t-tshift(kk);
figure(1000)
plot(t1,dati(:,kk)+(npunti-kk)*.3,'.r',t1,...
teo+(npunti-kk)*.3,'-k');
hold on
xlabel('t (ns)');
ylabel('signal');
warning off
figure(1001)
semilogy(t1,dati(:,kk),strcat('.',colors(kk))...
,t1,teo,strcat('-',colors(kk)));
hold on
xlabel('t (ns)');
ylabel('signal');
warning off
cd savedirectory
saveas(kk, titolfig)
cd ..
close(kk)
end
tshiftnew=tshift;
return
```

D.3 Second function: Gchi2sto.

```
function chiquadro=...
chi2sto(par,n,l1,l2,t,tshift,energia,...
dati,rf,tshiftr,t0,EAR)
sized=size(dati);
npunti=sized(2);
last=length(par);
```

```
tau0=par(1);
alpha0=par(2);
if EAR==1
bamma=0;
end
dt=t(2)-t(1);
for kk=1:npunti
theta=(1+sign(t-t0-tshift(kk)+tshiftr+dt*1e-9))/2;
if EAR==0
flnorm=theta./(1+energia(kk)*alpha0*...
(t-t0-tshift(kk)+tshiftr)).^2;
flnorm=(theta.*exp(-2*(t-t0-tshift(kk)+tshiftr)/tau0)...
)./(1+energia(kk)*alpha0*tau0*...
(1-exp(-(t-t0-tshift(kk)+tshiftr)/tau0))).^2;
elseif EAR==1 flnorm=(theta.*...
exp((-t+t0+tshift(kk)-tshiftr)/tau0)...
).*(1./(1+energia(kk)*alpha0*...
(t-t0-tshift(kk)+tshiftr)).^(bamma+1));
end
flnormf=fft(flnorm);
flnormfr=rf.*flnormf;
flnormr=real(ifft(flnormfr));
if EAR==0
flexp1=theta.*exp((-t+t0+tshift(kk)-tshiftr)/tau0);
elseif EAR==1
flexp1=(theta.*exp((-t+t0+tshift(kk)-tshiftr)...
/tau0)).*(1./(1+energia(kk)*alpha0*...
(t-t0-tshift(kk)+tshiftr)).^(bamma));
end
flexpf1=fft(flexp1);
flexpf=rf.*flexpf1;
flexp=real(ifft(flexpf));
A(:,1)=flnormr;
A(:,2)=flexp;
c=A(l1:l2,:)\dati(l1:l2,kk);
teo=A*c;
chiquadro_mat(kk)=((norm...
(teo(l1:l2)-dati(l1:l2,kk)))^2);
end
chiquadro=sum(chiquadro_mat)/...
(npunti*(l2-l1+1-length(c))-last);
```

Conclusions.

As always happens, the final point of a scientific investigation can be regarded as the starting point of the subsequent one. This is true in our case too. Some results have been achieved by the present work, and many prospects arise from them. In this final section, we would like to stress both of them. Let us, here, summarize our principal experimental results and the possible future developments of the two experimental tecniques we performed.

For what concerns the Coherent Raman Spectroscopy experiment, we would like to emphasize that the presence of a significant "reflected" CRS signal, without damaging the sample, should not be given for granted. We demonstrated that this route can be followed. The use of the "reflection" geometry can avoid many experimental problems, which are mostly related to the substrate contribution and the phase-matching condition. These were the main difficulties in the past attempts to use this technique on HTCS. Besides this, the investigation of the Cuprate superconductors by means of the CRS has revealed to be a very powerful tool in order to study the coherent spectrum of phonons and their relative phases. Although we were able to interpret our data within a simple semiclassical model, a deeper theoretical investigation about the measured values of the phonon phases should be done, in order to achieve a better understanding of the underlying physics. The possibilities of this spectroscopic technique should be further investigated, in particular in the superconductive phase, since the role of phonons in the phenomenon of the high temperature superconductivity is far from being understood. The CRS technique could be also useful in order to study many other materials in the wide class of the high-correlated electron systems. However, this is not the unique advantage of the CRS. Our work opens the route to the measurement of a selected quasiparticle lifetime, which is quite difficult to manage with other optical techniques. This time-resolved study may help clarifying the coupling mechanism at the root of the Cooper's pair formation and it still remains the main goal of our work.

If the results presented here can be regarded, without doubt, as a preliminary work, we are nonetheless confident that the main difficulties have been overcome and that the CRS apparatus we developed will be able to give an invaluable information about the fundamental physics of cuprate superconductors.

For what concerns the time-resolved photoluminescence experiment on strontium titanate, we obtained many quite strict experimental results.

First of all, we would like to stress that the photoinduced high charge-density regime we have studied can be generated and probed without any sample damage, thus opening the way to several other possible investigations of this interesting

regime. Our results set the upper bandwidth limit of STO-based emitting devices above 1 GHz, opening some interesting prospects on the fabrication of integrated optoelectronic devices based on titanates, where the growth of epitaxial heterostructures allows integrating emitting elements with tunable filters, optical switches, and ultrawide bandwidth modulators.

Moreover, we found a non-common recombination kinetics: the time-resolved luminescence decay is well explained by assuming the presence of two separate decay channels, one associated with a direct recombination of unbound mobile electron-hole charge carriers and the other with the recombination of bound electron-hole pairs. Very strong overall similarities were found in the emission spectrum, the yield and the decay dynamics of the photoluminescent response of pure, oxygen deficient and Nb-doped STO. This results point to a very minor role of donors and doping induced electrons both on the states involved in the transition, and at least on the most relevant decay mechanism, i.e., the bimolecular one.

Finally, an interesting behaviour of the photoluminescence spectrum at different temperatures was found, and its correct interpretation will help choosing between several possible recombination models.

The microscopic recombination mechanisms taking place in this system remain uncertain, although the polaron character of the charge carriers and the presence of intrinsic crystal defects are both likely to be involved in these processes.

The renewed attention on an old and possibly not-so-well-known compound, such as STO, can be, thus, justified since many electronic features of this "evergreen" material still have to be fully explained. We hope to have contributed to their understanding as much as we could.

Bibliography

[1] V.N. Bagratashvili et al. - Phys. Lett. A **164** (1992).

[2] A. Frova - Fisica nella musica, Zanichelli, Italy (1999).

[3] R.W. Boyd - Nonlinear Optics, Academic Press, USA (1992).

[4] Y.R. Shen - The principles of Nonlinear Optics, John Wiley & Sons, USA (1984).

[5] H.J. Eichler, P. Gunter, D.W. Pohl - Laser induced dynamic gratings, Springer-Verlag, Germany (1986).

[6] M.K. Wu et al. - Phys. Rev. Lett. **58**, 908 (1987).

[7] J.R. Waldram - Superconductivity of Metals and Cuprates, IOP-Publ. Ltd (1996).

[8] P.W. Anderson - Theory of superconductivity in the High Tc Cuprates, Princeton U.P. (1997).

[9] Z.X. Shen et D.S. Dessau - Phys. Rep. **253**, 1-162 (1995).

[10] J.R. Cooper, A. Carrington - Adv. in Supercond. p95 (1992).

[11] J.F. Annett et al. - Physical Properties of HTSC vol2, p571 (1990).

[12] Q.P. Li et al. - Phys. Rev. B **48**, 437 (1993).

[13] D.J. Van Harlingen - Rev. Mod. Phys. **67**, 515 (1995).

[14] A.B. Migdal - Zh. Eksp. Teor. Fiz. **34**, 1438 (1958) / Sov. Phys. JETP **7**, 996 (1958).

[15] J. J. Friedel - Phys. Cond. Matter **1**, 7757 (1989).

[16] J. Orenstein et J. Millis - Science **288**, 468 (2000).

[17] P.W. Anderson - Phys. Rev. **115**, 2 (1959).

[18] J. Zaanen - Science **286**, 251 (1999).

[19] J. Tranquada et al. - Nature **375**, 561 (1995).

[20] P.J. Hirschfeld et al. - Phys. Rev. Lett. **71**, 3705 (1993).

[21] S. Sachdev - Science **288**, 475 (2000).

[22] A.G. Loser et al. - Phys. Rev. B **56** 14185 (1997).

[23] P.W. Anderson - Science **288** 480 (2000).

[24] P.A. Lee - Physica C **317-318** 194-204 (1999).

[25] M. Cardona - Physica C **317-318** 30-54 (1999).

[26] M. Opel et al. - Phys. Rev. B **61** n14 9752 (2000).

[27] N. Gedik et al. - Science **300** 1410 (2003).

[28] N. Gedik et al. - Phys. Rev. B **70**, 014504 (2004).

[29] N. Gedik et al. - J. of Supercond. **17** 1 117 (2004).

[30] G. Turrell - Infrared and Raman Spectra of Crystals, Academic Press, London (1972).

[31] Liu et al. - Phys. Rev. B **37** n13, 7971 (1988).

[32] F. Bassani,U.M. Grassano - Fisica dello Stato Solido, Bollati Boringhieri, Torino (2000).

[33] P.Y. Yu, M. Cardona - Fundamentals of Semiconductors, Springer, Berlin (1996).

[34] A.S. Davydov - Teoria del Solido, Edizioni MIR, Moscow (1984).

[35] Various Authors - Semiconductors and Semimetals, Academic Press, New York (1972).

[36] Various Authors - Light Scattering in Solids, Springer-Verlag, Berlin (1975).

[37] F. Bassani, G. Pastori Parravicini - Optical Transitions in Solids, Pergamon Press (1975).

[38] V.E. Henrich, P.A. Cox - The Surface Science of Metal Oxides, Cambridge U.P. (1994).

[39] J.J. Hopfield - Proc. 7th Int. Conf. on the Phys. of Semicond. Dunod, Paris, pp. 725-735 (1964).

[40] W.P. Dumke - Phys. Rev. **132**, 1998-2002 (1963).

[41] Y. Toyozawa Prog. Theor. Phys. Suppl. **12**, 111-140 (1959).

[42] M. Tinkham - Introduction to superconductivity, McGraw-Hill, USA (1975).

[43] Bednorz J.G., Muller K.A. - Z. Phys. **64** 189 (1986).

[44] H. Barrett - Phys. Rev. **86** 118 (1952).

[45] O. Bidault et al. - Phys. Rev. B **52** n6, 4191 (1995).

[46] H.P.R. Frederiske et al. - Phys. Rev. **134** A442 (1964).

[47] H. Yasunaga - J. Phys. Soc. Jap. **24** n5, 1035 (1967).

[48] A.H. Kahn et al. - Phys. Rev. **135** A1321 (1964).

[49] H.P.R. Frederiske et al. - Phys. Rev. **143** 648 (1966).

[50] R.O. Bell, G. Rupprecht - Phys. Rev. **129** 90 (1963).

[51] L. Rimai, G.A. de Mars - Phys. Rev. **127** 702 (1962).

[52] F.W. Lytle - J. App. Phys. **35** 2212 (1964).

[53] H. Katsu et al. - J. App. Phys. **90** 4578 (2001).

[54] K.A. Muller, H. Burkard - Phys. Rev. B **19** 3593 (1979).

[55] W. Cochran - Adv. Phys. **9** 387 (1960).

[56] H. Vogt - Phys. Rev. B **51** 8046 (1995).

[57] Y. Qiu et al. - Phys. Rev. B **72** 224105 (2005).

[58] V.S. Vikhnin et al. - Phys. Rev. B **65** 104304 (2002).

[59] V.S. Vikhnin et al. - EuroPhys. Lett. **56** 702-708 (2001).

[60] A. Stashans - Mat. Chem. Phys. **68** 214 (2001).

[61] T. Higuchi et al. - Phys. Rev. B **65** 033201 (2001).

[62] J.F. Schooley et al. - Phys. Rev. Lett. **12** 474 (1964).

[63] K. van Benthem et al. - J. App. Phys. **90** n12, 6156 (2001).

[64] C. Itoh et al. - J. of Lum. **112** 263-266 (2005).

[65] A. Lagendijk et al. - Chem. Phys. Lett. **20** 92 (1973).

[66] T. Hasegawa, K. Tanaka - J. of Lum. **94-95** 15-18 (2001).

[67] A. Othomo, H.Y. Hwang - Nature **427** 423 (2004).

[68] S. Thiel et al. - Science **313** 1942 (2006).

[69] M. Capizzi, A. Frova - Phys. Rev. Lett. **25** n18, 1298 (1970).

[70] M. Cardona - Phys. Rev. **140** 2A, A651 (1965).

[71] D.M. Eagles et al. - Phys. Rev. B **54** n1, 54-22 (1996).

[72] H.G. Reik - Z. Phys. **203** 346 (1967).

[73] L. Grabner - Phys. Rev. **177** n3, 1315 (1969).

[74] M. Aguilar, F. Lopez - J. App. Phys. **53** 12 (1982).

[75] R. Leonelli, J.L. Brebner - Phys. Rev. B **33** n12, 8649 (1986).

[76] W.F. Zhang et al. - App. Phys. A **70** 93-96 (2000).

[77] L. Grigorjeva et al. - Ferroelectrics **304** 117-123 (2004).

[78] S. Mochizuki et al. - J. Lum. **112** 267-270 (2005).

[79] S. Mochizuki et al. - J. Phys. Cond. Matt. **17** 923-948 (2005).

[80] S. Mochizuki et al. - Physica B **376-377** 816-819 (2006).

[81] H.Y. Hwang - Nature Mat. **4** 803 (2005).

[82] D. Kan et al. - Nature Mat. **4** 816 (2005).

[83] D. Kan et al. - App. Phys. Lett. **88** 191916 (2006).

[84] T. Rappen et al. - Phys. Rev. B **48** 7, 4879 (1993).

[85] B. Fainberg - Opt. Comm. **89** 5-6, 403-409 (1991).

[86] A.N. Zherikhin et al. - Physica C **221** 311-318 (1994).

[87] D. Reznik et al. - Physica C **185-189** (1991).

[88] M.V. Klein et al. - Physica C **185-189** (1991).

[89] B. Fainberg and D. Huppert - Physica C **209**, 95-98 (1993).

[90] H.J. Zarrabi et al. - App. Phys. Lett. **46** 513 (1985).

[91] J. Linnros - J. of App. Phys. **84** 275 (1998).

[92] N.F. Massè et al. - App. Phys. Lett. **90** 161113 (2007).

[93] S. Jursenas et al. - Phys. Rev. B **54** 16706 (1996).

[94] C. Thomsen and G. Kaczmarczyk - Handbook of Vibrational Spectroscopy, J. Wiley & Sons Ltd, Chichester, (2002).